SATELLITE TO SATELLITE DOPPLER TRACKING (SSDT)
FOR MAPPING OF THE EARTH'S GRAVITY FIELD

Final Report

For the period 1 April 1980 through 31 March 1981

Grant No. NAG5-36

(NASA-CR-164722) SATELLITE TO SATELLITE DOPPLER TRACKING (SSDT) FOR MAPPING OF THE EARTH'S GRAVITY FIELD Final Report, 1 Apr. 1980 - 31 Mar. 1981 (Smithsonian Astrophysical Observatory) 107 p HC A06/MF A01
N81-31601
Unclas
G3/43 27314

Principal Investigators

Dr. G. Colombo
Dr. E. M. Gaposchkin
Dr. M. Grossi

Prepared for
National Aeronautics and Space Administration
Goddard Space Flight Center
Greenbelt, Maryland 20771

September 1981

Smithsonian Institution
Astrophysical Observatory
Cambridge, Massachusetts 02138

The Smithsonian Astrophysical Observatory
and the Harvard College Observatory
are members of the
Center for Astrophysics

SATELLITE TO SATELLITE DOPPLER TRACKING (SSDT)
FOR MAPPING OF THE EARTH'S GRAVITY FIELD

Final Report

For the period 1 April 1980 through 31 March 1981

Grant No. NAG5-36

(NASA-CR-164722) SATELLITE TO SATELLITE DOPPLER TRACKING (SSDT) FOR MAPPING OF THE EARTH'S GRAVITY FIELD Final Report, 1 Apr. 1980 - 31 Mar. 1981 (Smithsonian Astrophysical Observatory) 107 p

HC A06 / MF A01

N81-31601

Unclas

G3/43 27314

Principal Investigators

Dr. G. Colombo
Dr. E. M. Gaposchkin
Dr. M. Grossi

Prepared for
National Aeronautics and Space Administration
Goddard Space Flight Center
Greenbelt, Maryland 20771

September 1981

Smithsonian Institution
Astrophysical Observatory
Cambridge, Massachusetts 02138

SATELLITE TO SATELLITE DOPPLER TRACKING (SSDT)
FOR MAPPING OF THE EARTH'S GRAVITY FIELD

Final Report

For the period 1 April 1980 through 31 March 1981

Grant No. NAG5-36

Principal Investigators
Dr. G. Colombo
Dr. E. M. Gaposchkin
Dr. M. Grossi

Prepared for
National Aeronautics and Space Administration
Goddard Space Flight Center
Greenbelt, Maryland 20771

September 1981

Smithsonian Institution
Astrophysical Observatory
Cambridge, Massachusetts 02138

ACKNOWLEDGEMENTS

This report has been prepared by Dr. Robert D. Estes, of the Radio and Geoastronomy Division of the Harvard-Smithsonian Center for Astrophysics, Cambridge, Massachusetts 02138.

ABSTRACT

A new analytical tool has been formulated (and the related software developed) for carrying out performance evaluation of satellite-to-satellite doppler tracking (SSDT) schemes devoted to the recovery of gravity anomalies in the earth crust. Two schemes have been evaluated: a) a "standard," low-low, SSDT configuration, in which both satellites are in basically the same low altitude nearly-circular orbit and the pair is characterized by small angular separation; b) a more general configuration (the Colombo scheme) in which the two satellites are in arbitrary orbits, so that different configurations (such as the "high-low" mode) can be comparatively analyzed. By using the analytical tool above, it has been found that the "standard" low-low SSDT configuration is capable of recovering 1° x 1° surface anomalies with a stregth as low as 1 milligal, located on the projected satellite path, when observing from a height as large as 300 km (angular separation of the two satellites: 6° to 8°). This configuration has also been shown to be capable of resolving, for instance, two 20 milligal anomalies of the same sign, each 1° x 1°, located 2° apart on the projected satellite path, when observing from an altitude of 200 km (satellites' angular separation 5°). The Colombo scheme, in the "high-low" mode, provides an important complement of "low-low" SSDT observations, inasmuch as it is sensitive to radial velocity components, while keeping at the same performance level both measuring sensitivity and measurement resolution. It also offers substantial advantages with respect to the "standard" low-low case, from the standpoint of drag compensation requirements.

Table of Contents

LIST OF ILLUSTRATIONS

1. INTRODUCTION

Satellite-to-satellite Doppler tracking (SSDT) is a promising method of obtaining information about the fine-structure of the earth's gravitational field, which as yet has not been extensively utilized (1-4). The method offers the advantages of wide coverage and sensitivity sufficient to detect and measure anomalies on the order of 1 mgal over wavelengths in the 100 km range. Given the cost of actual SSDT experiments, it is desirable to have computer models available in which various relevant parameters such as satellite height, satellite orbital configuration, satellite separation, anomalous mass distribution, integration time, and noise level can be varied for use in studies designed to compare the relative merits of different configurations and the ability of the method to obtain the anomalous mass distribution from Doppler relative velocity data under different assumptions.

The primary goal of this study is to obtain an economical method for carrying out such sensitivity and feasibility studies. We have developed a method that applies not only to the "standard" low-low SSDT configuration in which both satellites are in basically the same, near-circular, low earth orbit with small angular separation, but to the general case in which the two satellites are in arbitrary orbits, so that the method can be used to compare different configurations. We have applied this technique to the problem of recovering gravitational anomalies in several practical cases. We were particularly interested in a comparison of the efficiency of the standard low-low configuration with an alternative configuration, proposed by Dr. Giuseppe Colombo of the Smithsonian Astrophysical Observatory (SAO). The latter, which would obtain information about both the radial and angular variations in the gravitational potential in the region of space through which the satellites move, is discussed in more detail here below.

An additional problem that we have addressed is the choice of altitude and spacing of the satellites in the low-low configuration. There is an obvious tradeoff involved between signal strength and detectable wavelength in the choice of satellite altitude. That is, the lower the altitude is, the greater the signal strength, but for a given integration time the dimensions of detectable longtitudinal variations that can be resolved decrease with decreasing altitude. The necessity of minimizing atmospheric drag places a practical lower limit on the altitude as well. Wider spacing between satellites also improves both signal strength and resolution up to a point. We have conducted a number of simulations to determine the relative velocity signatures for various choices of satellite height and separation for gravitational anomalies directly beneath the satellite path and at various distances from the path. This study is reported in detail below in both graphical and tabular form.

Since the use of a drag-free system would eliminate a possibly troublesome source of uncertainty in the anomalous relative velocity measurements, we have also studied the savings that might be expected for such a system through the use of the

Colombo scheme referred to above and examined in detail in the body of this report.

The basic problem involved in SSDT studies, using either actual or simulated data is to convert the raw measurements of relative line-of-sight velocity between the two satellites into an anomalous mass distribution on or within the earth. The first problem is to eliminate the portion of the relative velocity variations due to causes other than gravitational anomalies, i.e., those due to the "standard" terrestrial gravitational field (which can be defined in various ways in simulation studies), to atmospheric drag, and to the various other small perturbations that are well-known in satellite dynamics (radiation pressure, etc.). This of course includes the contribution due to the difference in the satellite orbits, which is zero only in the case of perfectly circular orbits with non-central force term neglected. To obtain the actual relative velocity from doppler measurements the contribution due to the variation in the ionospheric electron density, i.e., the index of refraction, must be removed. An additional factor that could be important in an actual experiment is the integration time. In the present study we assume that ionospheric corrections have been made correctly and that measurements are instantaneous though separated by time intervals corresponding to the integration time. There is no inherent reason why this last assumption must be made. It is made only for convenience, and the same software could be used to study the effects of integration time on the recovery of short wavelength anomalies.

Once we have obtained the relative velocity variation and we have separated the part due to the gravity anomaly as defined above, we are faced with the problem of converting this velocity variations data into either a special additional mass distribution (+ or -) or a special variation of potential distribution on, say, the earth's surface. The first step in this conversion process involves obtaining formulae that give the relative velocity components in terms of the anomalous potential at the satellite positions. The differential equations relating satellite position and velocity and the anomalous potential at the satellite position are easily obtained from the general equations of motion. We have dealt with the problem of solving these equations by obtaining linearized equations for the perturbed satellite co-ordinates, which can then be easily integrated by numerical techniques.

Implicit in this integration is of course a particular form for the anomalous potential at the satellite position. A simple formulation, and one that can be applied to the analysis of actual data and to simulation studies, is that of the potential due to a grid of surface patches on which either the difference in the potential between the actual case and the standard model is known or an equivalent variation of surface mass density is known. The potential outside the surface, at the satellite position for example, due to such a distribution is readily obtained from potential theory.

Having obtained the perturbed relative velocity as a linear function of surface anomaly strengths, we are then in a position to utilize least-squares fitting to obtain the best estimate of surface strength values (for the particular model) relative to the data, which can be either actual data or data simulated by an independent method, such as integrating the full equations of motion for the satellites in the presence of and in the absence of gravitational anomalies.

In outline then, this is the program we have followed, and we have been able to demonstrate that our method of obtaining perturbed relative velocity works well in the sense that, not only does the velocity signature for a given anomaly distribution obtained by this method closely correspond to that obtained by the more lengthy simulation procedure, such as integrating the full equations, but the anomaly distribution obtained by the least-squares inversion technique also agrees well with the input simulation distribution for a linear array of surface elements oriented along the satellite path. As expected, the resolving power is found to be weaker for the case of a linear array of elements oriented perpendicular to the satellite path or at various distances below the earth's surface. This ability to recover the simulation mass anomaly distribution is the crucial test, and we have documented the success of the method in a number of different cases. In addition, we propose further studies that could easily be undertaken utilizing the software we have developed. Both the method used and the results obtained are explained in detail in the following sections.

2. SATELLITE ALTITUDE AND SEPARATION STUDY

Before proceeding to demonstrate the recoverability of an anomolous mass distribution (or gravitational potential distribution) by least-squares fitting, we addressed the question of optimal altitude and satellite separation from the standpoint of signal strength and observed wavelength of the perturbed relative velocity waveform caused by a single one degree by one degree surface mass anomaly. We have simulated a number of cases, varying satellite height and separation as well as the distance of the anomaly from the path of the satellite projected onto the earth's surface. This was done only for the standard low-low configuration with an eccentricity of 0.001 and with altitudes ranging from 175 km to 300 km, angular separations ranging from two to eight degrees, and distances of the anomaly from the projected satellite path of zero to 40 degrees (one degree corresponds to approximately 110 km). To be more specific, the satellite heights considered were 175, 200, 250, and 300 km, while the separation choices were two, four, five, six, and eight degrees. The angular separation of the anomalies from the projected satellite path was taken in ten degree increments.

Figures 1-13 display the perturbed relative velocity signatures for a number of these simulations. The relative velocity is plotted in mm/sec versus the time in seconds. Both the initial satellite positions and the longtitude of the anomaly are held constant throughout. The orbit is equatorial for simplicity of interpretation. The surface gravitational anomalies are all of the same dimensions (1° x 1°) and strength as well: 200π mgals. Since the effect is very nearly linear, one can obtain the relative velocity amplitude for any arbitrary anomaly strength (of the same surface area) by changing the velocity and anomaly strengths in the same ratio.

The pattern that emerges from studying these relative velocity signatures is quite clear and has an obvious physical explanation. First let us consider the sequence of Figures 1, 2(a), 3(a), and 4, corresponding to an altitude of 175 km and separations of two, four, six, and eight degrees, respectively. The anomaly is fixed directly on the projected satellite path for this sequence. As the separation between the satellites increases, we note an increase in the amplitude of the relative velocity waveform. The waveform takes its particular shape due to the fact that first one, then the other satellite undergoes an acceleration due to the anomaly, which exerts a significantly different effect on the satellite behavior only when the difference in satellite-to-anomaly distance becomes significant. When the satellite separation is small, the second satellite to "see" the anomaly begins to do so before the first one through has reached its maximum perturbed velocity. This diminishes the maximum relative perturbed velocity observed. Thus we see a steady increase in signal strength in going from to two to six degrees, which begins to level off thereafter as the perturbed relative velocity begins to approach the perturbed velocity of the individual satellite most affected by the gravitational anomaly. In Figure 4, with a separation of eight degrees, we see that we are approaching the point where each satellite sees the anomaly separately. This is evidenced by the shoulder in the curve between the two extremes in perturbed relative velocity.

The same general behavior is observed in the corresponding 200km altitude sequence of Figures 5, 6(a), 7(a), and 8 and in the similar sequences for 250 km and 300 km altitudes. These results indicate that for detecting gravitational anomalies with dimensions of around 100 km by 100 km a satellite separation of some five to six degrees should be optimum for the low-low configuration. Since the Wolf (4) approximations used to relate perturbed relative line-of-sight velocity to anomalous gravitational potential become less accurate as the separation increases, this points to the necessity of obtaining a more general, fast, and economical way of obtaining this relationship, which is the main subject this report.

Another obvious and expected phenomenon one can note in these figures is a decrease in signal strength as the satellite height is increased (for a given satellite separation). Since all of the peak-to-peak signals are tabulated below we shall not discuss this effect further.

When we study the changing behavior of the perturbed relative velocity signature for fixed height and separation and variable anomaly position we notice that the shape of the waveform changes and that there is an overall downward shift in the data , so that for anomaly-to-path distances of twenty degrees or more the perturbed relative velocity is negative from the beginning. We ascribe this to the geometry of the configuration. While the "leading" satellite is still given a greater perturbed velocity than the "trailing" one in the first half of the path, the component of perturbed velocity along the line-of-sight, i.e., the original direction of motion, is greater for the trailing satellite. This is just a consequence of our taking the initial "unperturbed" position so close (in terms of differential satellite distances) to the off-line anomaly.

The peak-to-peak signal strength is seen to fall drastically as the distance from the projected satellite path is increased. All of the results are tabulated below (see Table 1) in terms of peak-to-peak perturbed relative velocity signal strength per mgal of anomaly strength. It is hoped that in future satellite-to-satellite Doppler tracking experiments noise levels in the perturbed relative velocity measurements can be kept below 10^{-6} m/sec or 10^{-7} m/sec. Since the last column in the table gives the peak-to-peak signal strength in units of 10^{-6} m/sec due to a one degree by one degree surface anomaly of 1 mgal strength, it can be used as a measure of whether such an anomaly would cause a signal of sufficient magnitude to be detectable for the various altitudes and separations in the low-low configuration. Clearly a 1 mgal directly on the projected satellite path will give a signal well above the 10^{-6} m/sec noise level in all cases. The peak-to-peak signal falls off by 50 percent in going from 175 km height to 300 km height for satellite separation of 8 degrees. Since the 300 km signal should still be more than adequate for anomaly recovery and since the atmospheric drag would be much smaller at this altitude, this factor would seem to make the higher altitude attractive for an actual experiment.

As the anomaly is moved away from the projected satellite path it begins to make a decided difference whether or not the more stringent condition on the noise (noise $< 10^{-7}$ m/sec) can be met. The numbers in the table speak for themselves. As we show in another section dealing with recoverability of anomalies aligned perpendicular to the projected orbital path, there is another problem associated with detecting off-line anomalies. But this is basically a resolution problem due to the similarity of perturbed velocity signatures between two anomalies that are close to each other and both at some distance from the projected orbital path.

One other feature of the simulated signal strength data is worth pointing out. As the distance of the anomaly from the projected satellite path increases, the effect of varying the satellite height becomes less important. This is simply because the distance from the anomaly to the projected satellite path becomes much larger than the altitude and becomes the dominant contribution to the satellite-to-anomaly distance which determines the velocity response.

Table 1

Velocity Signal Strengths for Simulated Cases

altitude (km)	separation (degrees)	anom. location (degrees)	peak-to-peak signal ($\mu m\ sec^{-1}$/mgal)
175	2	0	11.3
175	4	0	15.9
175	4	10	0.6
175	4	20	0.1
175	6	0	17.5
175	6	10	0.9
175	6	20	0.2
175	8	0	17.8
200	2	0	9.0
200	4	0	13.2
200	4	10	0.6
200	4	20	0.1
200	6	0	14.8
200	6	10	0.9
200	6	20	0.2
200	8	0	15.2
250	2	0	5.9
250	5	0	10.3
250	6	0	11.1
250	6	10	0.8
250	6	20	0.2
300	2	0	4.1
300	5	0	7.6
300	5	10	0.7
300	5	20	0.2
300	6	0	8.1
300	6	10	0.8
300	6	20	0.2
300	8	0	8.9

3. THE RECOVERY OF GRAVITATIONAL ANOMALIES FROM RELATIVE VELOCITY DATA

Although the perturbed velocity due a given surface distribution of gravitational anomalies can be obtained by numerically integrating the equations of motion for a satellite in the resultant gravitational field, as it is done in the Apollo Soyuz Test Project (ASTP) integration program, which was developed for this purpose at SAO, it is desirable to obtain a more economical method since in feasibility/sensitivity studies one may wish to study numerous different cases, varying parameters such as orbital height, satellite separation, and orbital configuration, as well as the anomaly distributions. In the original low-low scheme proposal by Wolf (4), energy conservation is utilized to obtain a linear relation between the perturbed along-the-track velocity and the anomalous potential at the satellite position. This is done as follows.

Since gravity is a conservative force (and this includes the force due to any surface anomalies) we have

$$\tfrac{1}{2}V^2(r,\theta)+U(r)+T(r,\theta)=\tfrac{1}{2}V^2(r',\theta')+U(r')+T(r',\theta') \qquad (1)$$

where V is the satellite velocity, U the central potential due to the spherically symmetric part of the earth's mass distribution, and $T(r, \theta)$ is the anomalous gravitational potential, which in general includes all higher order harmonics of the earth's potential, but which for the purposes of the present discussion we limit to the potential due to some surface distribution of gravitational anomalies. The primed and unprimed variables refer to any two different points along the satellite orbit. The angle θ determines the position of the satellite along the orbital path. For a nearly circular orbit $r' \doteq r$, so that the the central potential terms are nearly equal at the two points.

Since T is assumed to be much smaller than U, the components of the perturbation in velocity (relative to the case when T = 0) are much smaller than the unperturbed velocity V . Thus

$$\begin{aligned} V^2 &= (\vec{V}+\vec{v}_\perp+\vec{v}_\parallel)^2 = V_0^2 + 2V_0 v_\parallel^2 + v_\parallel^2 + v_\perp^2 \\ &\doteq V_0^2 + 2V_0 v_\parallel \end{aligned} \tag{2}$$

where $v_\parallel$ and $v_\perp$ are the components of the perturbed velocity along the unperturbed path and perpendicular to the unperturbed path, respectively. The quadratic terms are negligible in comparison with the linear term in $v_\parallel$. Combining equations (1) and (2) gives the simple linear relation

$$v_\parallel(\theta_1) - v_\parallel(\theta_2) = (T(\theta_2) - T(\theta_1))/2V_0 \tag{3}$$

where θ_1 and θ_2 are any two positions along the orbit.

In the case where there are two satellites moving in the same unperturbed orbit but with angular separation $\Delta\theta$ the expression

$$v_{\parallel}(\theta+\Delta\theta)-v_{\parallel}(\theta)=(T(\theta)-T(\theta+\Delta\theta))/2V_0 \qquad (4)$$

obviously applies from the previous analysis. If the angular separation is small, then the relative line-of-sight velocity, i.e. the velocity determined by a Doppler measurement between the two satellites, is approximately equal to this difference in the along-the-track velocity. This is the beauty of the low-low scheme: by the use of energy conservation it turns the problem of obtaining satellite height anomalous potential values from Doppler velocity data into a geometrical problem. It is important to note the limitations of this scheme, however. It is strictly applicable only to circular unperturbed orbits with small angular separation. Since there are other considerations that recommend an angular spacing of some 5 degrees, as we demonstrate later on, it is important to investigate what kind of errors are introduced by equivalencing the relative velocity and the difference in along-the-track velocity.

In the general case of two arbitrary satellite orbits another approach is necessary. We are interested in solving this problem because a scheme that can deal with arbitrary satellite separation is needed for the low-low case and because one of the aims of this study is to investigate an alternative orbital configuration which samples both vertical and horizontal components of the gradient of the anomalous potential, utilizing orbits with non-negligible eccentricity.

The ASTP integrator (or any program that integrates the complete equations of motions) must solve six differential equations (3 position co-ordinates, 3 velocity co-ordinates), and the velocity equations involve non-linear functions of the spatial co-ordinates through the gradients of U and T as defined above. Under the assumption that the unperturbed orbits of the two satellites are co-planar, so that perturbations that are perpendicular to the orbital plane are irrelevant to the relative line-of-sight velocity to first order, we can reduce the problem to the solution of four differential equations in perturbed variables, all of which are linear in these variables. This is done in the following way.

First we write down the Lagrangian for a unit mass satellite moving in a potential that consists of the two already familiar parts U and T:

$$L=\frac{1}{2}(\dot{r}^2+r^2\dot{\theta}^2)-U(r)-T(r,\theta) \qquad (5)$$

Here r and θ are obvious polar co-ordinates of the satellite ($\theta = f + \omega$, where f is the true anomaly and ω the argument of perigee). As mentioned above, the other angular co-ordinate is irrelevant to the discussion. The equations of motion are then

$$\ddot{r} = r\dot{\theta}^2 - \frac{\partial U}{\partial r} - \frac{\partial T}{\partial r} \qquad (6)$$

$$\dot{M} = -\frac{\partial T}{\partial \theta}$$

where $M = r^2\dot{\theta}$ is the angular momentum. The zeroth order unperturbed equations are

$$\ddot{r}_0 = r_0\dot{\theta}_0^2 - \frac{\partial U}{\partial r}\Big|_{r=r_0} \qquad (7)$$

$$\dot{M}_0 = 0$$

If we eliminate the unperturbed part of the equations of motion and linearize the resulting equations we obtain

$$\delta\ddot{r} = -\frac{\partial T}{\partial r} + \frac{2M_0}{r_0^3}\delta M + \left(\frac{2GM_e}{r_0^3} - 3\dot{\theta}_0^2\right)\delta r$$

$$(8)$$

$$\delta\dot{M} = -\frac{\partial T}{\partial \theta}$$

where δr and $\delta M = 2\, r_0\dot{\theta}_0\delta r + r_0^2\,\delta\dot{\theta}$ are perturbations in the radial co-ordinate and angular momentum, respectively.

We thus have the system of four linear differential equations to solve:

$$\frac{d}{dt}(\delta\dot{r}) = \frac{-\partial T}{\partial r} + \frac{2M_0}{r_0^3}\delta M - \frac{GM_e}{r_0^3}(1 + 3e\cos f)$$

$$\frac{d}{dt}(\delta\dot{r}) = \delta\dot{r}$$

$$(9)$$

$$\frac{d}{dt}(\delta M) = \frac{-\partial T}{\partial \theta}$$

$$\frac{d}{dt}(\delta\theta) = (\delta M - 2r_0\,\dot{\theta}_0\delta r)/r_0^2$$

where G is the gravitational constant, M_e the mass of the earth, e is the orbital eccentricity and f the true anomaly.

We utilize a Runge-Kutta integration package RKF45 to solve these equations. To integrate these equations we must assume a particular form for the anomalous potential at the satellite positions. First let us consider the potential due to a distribution of anomalous surface mass density. Since we must have a potential that is linear in some variable parameters in order to carry out our least-squares fitting program, we use the approximation in which the surface mass density is constant over a given surface area, or in which we approximate a continuous distribution by a discrete one, breaking up the earth's surface into small surface areas and assigning the average value of the surface mass density over each small surface to that entire subsurface. The gravitational potential due to such a surface mass density is given by direct integration, using the Newtonian formula for the potential due to an arbitrary mass distribution.

$$T(\vec{r}) = GR^2 \int \frac{\sigma(\lambda',\phi')\,d\Omega'}{\rho} \qquad (10)$$

where $\delta(r - R)\sigma$ is the mass density, with R the radius of the earth and σ the surface mass density. The integration is over the solid angle that defines the subsurface. The vector $\vec{\rho}$ locates the space point (satellite position in our application) at which the potential is evaluated relative to a point on the subsurface of integration. Figure 14 shows the geometrical relationship between various position vectors and co-ordinates.

In equation (10) we have:

$$\rho = \sqrt{r^2 + R^2 - 2rR\cos\Psi} \quad . \tag{11}$$

The derivatives are then

$$\frac{\partial T}{\partial r} = -GR^2 \int \frac{(r - R\cos\Psi)\sigma(\lambda', \phi')d\Omega'}{\rho^3} \tag{12}$$

$$\frac{\partial T}{\partial \theta} = GR^2 \int \frac{rR}{\rho^3} \frac{\partial \cos\Psi}{\partial \theta} \sigma(\lambda', \phi')d\Omega' \tag{13}$$

Since we wish to work in an inertial co-ordinate system, we need to express all quantities in terms of inertial co-ordinates. In particular we must express the cosine of the angle between $\vec{R}$ and $\vec{r}$ in terms of these co-ordinates. The desired expression is obtained directly by use of rotation matrices to be

$$\begin{aligned}\cos\psi = {} & \sin\phi' \sin i \sin\theta + \cos\phi' \cos(\lambda' - \Omega)\cos\theta \\ & + \cos\phi' \sin(\lambda' - \Omega)\cos i \sin\theta\end{aligned} \tag{14}$$

where the relevant orbital parameters are defined as in Figure 15, and the inertial longitudinal angle locating the subsurface varies linearly in time as the earth rotates.

When we take the space point defined by $\vec{r}$ to be the satellite position, then the only quantities in the expression for the potential that vary are r, θ, and λ'. Since, by assumption, the perturbing potential makes only small variations in the satellite orbit we can take the time variation in r and θ to be given directly by the unperturbed solution to Kepler's equation. The variation in λ' depends only on the rotational velocity of the earth. The remaining problem is then to carry out the surface integration. For obtaining the design matrix we have just taken the value of the integrand at the center of the surface times the surface area. This amounts to a point mass approximation which should be adequate for initial studies of the sort we are undertaking. To generate the simulated data we broke the surface into a 3X3 grid of smaller surfaces and took the force contribution to the complete equations of motion from each surface to be the sum of the gradients of the potentials due to these subsurfaces.

The relationship between the surface mass density and the corresponding gravitational anomaly (anomalous gravitational acceleration) is easily obtained from Laplace's equation for the gravitational field and the use of the divergence theorem. This relationship is

$$\Delta g = -2\pi G\sigma \tag{15}$$

where σ is the equivalent surface density (gram/m^2) and G is the gravitational constant. This expression allows us to use gravitational anomalies in mgals as input into the simulation runs and to obtain these quantities in our least-squares fitting.

An alternative procedure would be to obtain the gravitational potential at the satellite position due to a surface distribution of potential. To do this the Laplace integral is utilized, which gives

$$T(\vec{r}) = \frac{R(r^2 - R^2)}{4\pi} \int \frac{T(\lambda', \phi')\,d\Omega'}{\rho^3} \tag{16}$$

$$\frac{\partial T}{\partial r} = \frac{2rR}{4\pi} \int \frac{T d\Omega'}{\rho^3} - \frac{3R(r^2 - R^2)}{4\pi} \int \frac{(r - R\cos\psi)}{\rho^5} T d\Omega' \tag{17}$$

$$\frac{\partial T}{\partial \theta} = \frac{3R(r - R)}{4\pi} \int \frac{rR}{\rho^5} \frac{\partial \cos\psi}{\partial \theta} T d\Omega' \tag{18}$$

The variables defined in these expressions are the same as those used in the previous expression for the potential due to a surface mass distribution.

We should mention that an additional level of complexity can be added by letting the anomalous masses be distributed beneath the earth's surface as well as on the surface. We have studied only a few such cases, and this is another area that would seem to deserve further study.

To obtain the complete design matrix that we require for our least-squares fitting procedure we must obtain the perturbed relative velocity due to the perturbed quantities obtained by the Runge-Kutta integration routine. The relative line-of-sight velocity is defined by

$$v^{12}=\frac{(\vec{r}_1-\vec{r}_2)\cdot(\vec{v}_1-\vec{v}_2)}{|\vec{r}_1-\vec{r}_2|} \tag{19}$$

where the subscripts refer to the two different satellites. Figure 16 defines the quantities graphically.

Then the perturbed relative velocity $\delta_v{}^{12}$ is given by

$$\begin{aligned}
\delta v^{12} \times r_{12} = [\,&\delta r_1(\dot{r}_1-\dot{r}_2\cos\theta_{12}+r_2(\dot{\theta}_1-\dot{\theta}_2)\sin\theta_{12}) \\
&+\delta\dot{r}_1(r_1-r_2\cos\theta_{12}) \\
&+(\delta\dot{\theta}_1-\delta\dot{\theta}_2)r_1r_2\sin\theta_{12} \\
&+\delta r_2(\dot{r}_2-\dot{r}_1\cos\theta_{12}+r_1(\dot{\theta}_1-\dot{\theta}_2)\sin\theta_{12}) \\
&+\delta r_2(r_2-r_1\cos\theta_{12}) \\
&+(\delta\theta_1-\delta\theta_2)\{\sin\theta_{12}(\dot{r}_1r_2+\dot{r}_2r_1)+\cos\theta_{12}r_1r_2(\dot{\theta}_1-\dot{\theta}_2)\}] \\
&+v_c^{12}[\delta r_1(r_2\cos\theta_{12}-r_1)+\delta r_2(r_1\cos\theta_{12}-r_2) \\
&\quad -r_1r_2\sin\theta_{12}(\delta\theta_1-\delta\theta_2)]
\end{aligned} \tag{20}$$

where

$$r_{12} = (r_1^2 + r_2^2 - 2r_1r_2\cos\theta_{12})^{1/2} = |\vec{r}_1 - \vec{r}_2|$$

4. DESCRIPTION OF THE SOFTWARE

We have developed a software package suitable for use in sensitivity/feasibility studies and for determining (in the least-squares sense) surface anomaly distributions from actual satellite-to-satellite Doppler tracking data.

In summary, the components of this software system are:

I) The ASTP integrator. This package of routines integrates the equations of motion for a satellite (or two satellites simultaneously) with given initial position and velocity vectors or, equivalently, initial Kepler orbital elements. The force acting on the satellite consists of numerous terms in addition to the central force of the spherically symmetric part of the earth's gravitational field. These terms, which include higher order harmonics of the terrestrial field, can be activated or not as desired. Most importantly for the present applications, the force due to a surface gravitational anomaly distribution can be included.

II) The "standard" low-low configuration model anomaly package. This model uses conservation of energy to obtain the dominant term in the perturbation of the relative line-of-sight velocity between two satellites in a given orbit due to a given surface anomaly in the gravitational field.

III) The general model anomaly package. This model obtains the perturbation in relative velocity by integrating the linearized differential equations for perturbations to the velocity of each satellite due to a given surface anomaly. A Runge-Kutta routine (RKF45) is used to carry out this integration (5).

IV) The Singular Value Decomposition (SVD) package. Taking as input the relative velocity matrix generated by I or II for a given sample of data points and set of surface anomalies, this set of routines obtains the singular value decompositon of the design matrix as well as the two matrices U and V (defined below) which transform the design matrix into the diagonal form. These three output matrices are then used to obtain least-squares fits corresponding to the particular model and orbit of the original design matrix for actual or simulated Doppler data.

Schematically these components interface in the way shown in Figure 17. The upper part of the diagram shows the method used to obtain simulated Doppler data. (A) The ASTP integration package is first used to obtain the relative velocity of the two satellites along a given path at selected times, or sample points, for given initial conditions and with no gravitational anomalies. For example, in the standard low-low configuration the two satellites might be chosen to have the same low-altitude (say 200 km) nearly circular orbit except for a small (say 5 degree) separation due to a difference in perigee. The relative velocities $\{\delta v^{o}_{j}\}$ for the zero-anomaly case, which are due strictly to orbital effects and vanish in the limit of zero eccentricity, are stored on a disk file for later use. (B) Now the ASTP integrator is run again with the same initial satellite positions and velocities but with a given surface anomaly distribution on the earth { Δg_i}. The relative velocity values { δv_j } are obtained for the same times as in step A. The values obtained in step A are then retrieved from the disk file on which they were stored and are then subtracted from the new relative velocity values. The resulting set of values is then the perturbed relative velocity set { $\delta v'_j$ }, corresponding to the anomaly distribution { Δg_i }. This is taken to be the simulated data. The step B can be repeated for as many different anomaly distributions as desired for a given orbital path without repeating step A. In fact, since the effect of the surface anomalies is linear, simulated data from any linear combination of anomaly distributions can be obtained directly from the corresponding linear combination of { $\delta v'_j$ } without re-running the ASTP integrator, a fact which can be utilized to reduce computer time.

The lower part of the diagram schematically illustrates the method used to obtain the design matrix and its singular value decomposition Σ, which is then utilized in the least-squares fitting. The following section describes this part of the process in more detail.

5. THE LEAST-SQUARES FITTING

The general method of least-squares fitting of data to a particular model assumes that one can approximate the actual measured values of the quantity of interest by a linear combination of basis functions (this is what we mean by the model), which may be nonlinear functions of the independent variable. For our purposes we may take the independent variable to be the time of observation or, equivalently, an angular variable such as the true anomaly. In the present instance the appropriate basis functions cannot be written down in closed form since they are obtained only through the integration of the differential equations (9). However, since our equations are linear, we know that these basis functions exist. Note that the equations must be linear in all the perturbed variables and in the anomalous potential (or its derivatives) for the method to be applicable. Each basis function corresponds to a different surface element, and the value of each basis function at a given time is determined strictly by the geometry of the particular orbit in question.

It is useful to introduce the concept of the design matrix in discussing the method. This is the rectangular matrix A in which each column corresponds to a definite basis function evaluated at the different observation times. In our case the design matrix consists of perturbed relative velocity values due to unit strength anomalies on the different surface elements, i.e.

$$A_{ij} = \delta v_i(t_j) = \delta v^*_{ij} \tag{21}$$

where $\delta v_i(t_j)$ is the perturbed relative velocity due to the ith surface element at time t_j. Then the least-squares program is to minimize the sum of the squares of the residuals, where the ith residual is defined by

$$r_j = A_{ij}C_i - \delta v'(t_j) \tag{22}$$

by choosing the best set of coefficients $\{c_i\}$.

To accomplish this we have utilized a singular value decomposition routine SVD (5). The singular value decomposition method allows us to transform the design matrix into a diagonal matrix Σ, the diagonal elements of which are known as the singular values of A. In this form the least-squares solution is trivial, assuming the singular values are not too small. Then this solution, which corresponds to a transformed set of basis functions, can be transformed into the solution corresponding to the initial basis functions. A powerful feature of this method is that it indicates if any of the basis functions are (almost) linearly dependent and allows one to eliminate meaningless solutions by setting the coefficients of the transformed (into the "singular" system) basis functions equal to zero if the corresponding singular value is less than the cutoff value. In practice this cutoff must be chosen in accordance with the accuracy of the data measurements or machine accuracy. Such a cutoff turned out to be necessary when a linear array of surface elements oriented perpendicular to the orbital path was studied, whether it was on the earth's surface or in the vertical direction.

Another powerful feature of this method is that the singular value decomposition Σ and the two orthogonal matrices U and V that transform A into Σ by

$$A = U\Sigma V^T \tag{23}$$

need only be computed once for a given orbital path and surface element array, i.e., for a given design matrix. The Σ , U, and V matrices can then be used over and over to obtain new least-squares fits to any number of simulated or actual data sets corresponding to the same orbital path.

6. THE ECCENTRIC SATELLITE PAIR SCHEME (Colombo Method)

The eccentric scheme, originally proposed by Dr. Giuseppe Colombo of SAO, appears to have a number of virtues that make it an attractive alternative to the standard low-low configuration. One of the primary goals of this study is to examine this scheme in more detail and obtain a better, quantitative evaluation of its characteristics, both in terms of retrieval of gravitational anomalies and economy.

The scheme is based on two satellites with very low area-to-mass ratios (or, alternatively, a drag free system) in near-earth orbits. The slightly eccentric orbits are symmetric with respect to the earth's center; the orbital elements of the two satellites are as follows, and their relative configuration is depicted in Figure 18.

Some numerical examples of the proposed configuration are given below, together with values for the true anomaly $\theta*$ when the two satellites are at the same altitude. In the examples, we have assumed that the Shuttle is the launching platform and have chosen three injection altitudes (220, 300, and 360 km). The perigee height has been kept constant at 160 km; the optimum perigee height will be the height at which the effect of gravity is at a minimum. The optimum apogee height will be based on the length of the system's lifetime.

Example 1. The Shuttle is in a circular orbit at 220-km height; the two satellites have the same semimajor axis, with perigee at 160 km and apogee at 280 km. We will then have

$$a = 6598 \text{ km} \quad , \quad e = 0.009094 \quad , \quad \theta^* = \pm 90\overset{\circ}{.}52 \quad .$$

Example 2. The Shuttle is in a circular orbit at 300-km height; the two satellites have the same semimajor axis, with perigee at 160 km and apogee at 440 km. We have

$$a = 6678 \text{ km} \quad , \quad e = 0.02096 \quad , \quad \theta^* = \pm 91\overset{\circ}{.}20 \quad .$$

Example 3. The Shuttle is in a circular orbit at 360-km height; the two satellites have the same semimajor axis, with perigee at 160 km and apogee at 560 km. We have

$$a = 6738 \text{ km} \quad , \quad e = 0.02968 \quad , \quad \theta^* = \pm 91\overset{\circ}{.}70 \quad .$$

From Figure 18 the fundamental property of the Colombo scheme is evident: The line of sight between the satellites takes on several geometric relationships with respect to specific points on the earth's surface. When, for instance, one satellite is at perigee, the other is at the apogee, and the line of sight between the two is perpendicular to the earth's surface (radial direction). When the true anomaly of one of the satellites is θ^* , the line of sight is horizontal. Therefore, the scheme is capable of measuring the radial and horizontal components of the velocity differential twice per orbit. Since the nodal line and the apsidal line precess, this sampling will cover the entire earth in a latitude span corresponding to twice the inclination. The inclination should not be too close to critical if we want the apsidal line to precess fast enough to give the required coverage.

7. ATMOSPHERIC DRAG AND THE COLOMBO SCHEME

A drag compensation system to eliminate the effects of drag on the relative velocity between the two spacecraft would certainly be the most effective way of eliminating noise due to variations in atmospheric density. However, the inclusion of such a system does increase the total cost of the experiment by a considerable amount. Thus an orbital configuration that maintains the sensitivity of the system to gravitational anomalies but decreases the fuel expenditure of the drag compensation system is highly desirable. In another section of this report we demonstrate that the Colombo scheme is as effective at detecting gravitational anomalies as the standard low-low scheme. We now examine it from the standpoint of fuel economy assuming a drag compensation system to be required.

At lower altitudes, the sensitivity of the system to gravity anomalies is better, but more fuel is consumed in order to compensate for atmospheric drag. A trade- off must be made between sensitivity and lifetime in chosing the orbit for the spacecraft. In the Colombo scheme, the spacecraft would be in eccentric orbits in order to combine the advantages of the low-low and the high-low configurations. A computer program has been written for integrating the drag on the satellite during one orbit in order to evaluate the orbital lifetime for various altitudes and eccentricities.

The equation for an elliptical orbit is

$$r = \frac{a\ (1-e^2)}{1 + e\cos\theta} \qquad (24)$$

where r is the distance from the center of the earth, θ is the angular position measured from perigee, a is the semi-major axis, and e is the orbital eccentricity. For small eccentricity we can write approximately

$$r \doteq a(1-e\cos\theta) \qquad (25)$$

The velocity v is given by

$$v = \sqrt{GM_e\ (2/r - 1/a)} \qquad (26)$$

The atmospheric density ρ can be represented approximately by

$$\rho = \rho_0 e^{-(h-h_0)/c} \qquad (27)$$

where ρ_0 is the density at $h = h_0$ and c is the scale height. The drag force F on the spacecraft is

$$F = A\rho v^2 \qquad (28)$$

where A is the drag cross section. The rate of fuel consumption necessary to counteract the drag force is given by

$$F = \dot{m}V = \frac{dmV}{dt} \qquad (29)$$

where V is the exhaust velocity and $\dot{m}$ is the rate of fuel consumption. The total mass m of the fuel used is

$$m = \int dm = \frac{1}{V} \int F dt \qquad (30)$$

In order to do the integration in the variable θ instead of t, we can make the transformation

$$dx = rd\theta = vdt \qquad (31)$$

or

$$dt = rd\theta \,/\, v \qquad (32)$$

This approximation is valid for low eccentricity orbits where v is nearly perpendicular to r. With this transformation the integral becomes

$$m = \frac{1}{V} \int \frac{Frd\theta}{v}$$

Substituting $F = A\rho v^2$ we have

$$m = \frac{1}{V} \int A\rho vrd\theta \qquad (34)$$

This expressing has been used to integrate the drag around one orbit ($\theta = 0, 2\pi$). The program actually computes

$$m\,V/A = \int \rho v r d\theta \qquad (35)$$

which has the units of dyne-sec/cm^2 in the cgs system.

A set of runs has been done with the following parameters; $GM_e = 3.986013 \times 10^{20}$ (cgs), $h_o = 200$ km., $\rho_o = 2.54 \times 10^{-13}$ g/cm^3 , $c = 30$ km. The table below lists the drag for various orbits.

Table II

Values of Drag For Various Orbits

Perigee (km)	a (km)	Apogee (km)	Drag (dyne-cm/sec^2)
200	200	200	817.20
180	180	180	1589.27
180	200	220	910.55
180	220	260	628.76
180	240	300	492.53
180	260	340	415.78
180	280	380	366.60
180	300	420	331.94

For the same semi-major axis, the drag increases with eccentricity. For example if the altitude decreases by one scale height, the drag increases by a factor of e = 2.718. If the altitude increases by one scale height, the drag decreases by a factor 1/e = .3678.

These results show that the Colombo scheme results in large savings compared to the standard low-low scheme, represented by the first two entries in the table. The question of overall sensitivity is not so easy to answer without more extensive study. It is quite clear from the anomaly recovery analysis we have made that for a given value of the perigee the Colombo scheme compares favorably with the standard low-low configuration as long as it is in the high-low portion of its operation. In comparing the circular 200 km low-low orbit (first entry in the table) with the a = 260 km, apogee=340 km Colombo configuration we find that the fuel expenditure for the circular orbit is almost 100 percent greater. The overall sensitivity of the Colombo case should be at least as good for a major part of the orbit. By referring back to the low-low perturbed relative velocity signatures of a single anomaly for 200 km and 250 km given in Figures 5, 6, 7, 8, 9, and 10 we can get an idea of how sensitivity compares during the low-low portion of the Colombo configuration. While the peak-to-peak signal strength may drop off as much as 50 percent in the Colombo configuration depending on the angular separation between the satellites it should be well above the threshold of detectability for anomalies of the order of a mgal, of dimension one square degree. Thus the Colombo scheme would seem to be quite competitive in terms of sensitivity, while offering substantial savings if a drag compensation system is utilized.

8. LONGITUDINAL LINEAR ARRAYS OF GRAVITATIONAL ANOMALIES

The critical test of the entire software package we have developed is whether the design matrix obtained by the use of the linearized equations for the perturbed velocity and space co-ordinates can, when coupled to the singular value decomposition routines, be used to recover a surface anomaly distribution by least-squares fitting to the corresponding relative velocity data generated in an independent simulation. In other words, can the system take data such as that shown in Figures 1-13 and obtain a good reconstruction of the surface anomaly distribution that caused the particular velocity signature observed? We have examined this problem in detail for a number of linear arrays of one degree by one degree surface anomalies for the standard low-low configuration and for the Colombo configuration in the high-low portion of the orbit. Figures 19-22 show the results of a series of simulation experiments in recovering the input surface anomalies by use of the least-squares fitting procedure outlined above.

Figures 19 and 20 display results of this procedure for a number of linear distributions of surface anomalies lying directly beneath the paths of two satellites in the low-low configuration. The design matrix is obtained for a ten-element array, and the anomaly strengths for each of these surface elements are subsequently obtained through the least-squares fitting procedure for each set of simulated data, the data having been simulated by the ASTP integration routine as outlined in the section devoted to software. The perturbed relative velocity data are displayed in Figures 19(a)-19(e), and a comparison between input distribution and recovered distribution is shown for each case in Figure 20, where the input anomaly strength has been normalized to 10mgal.

The satellites are at an altitude of 200 km with an angular separation of five degrees. The orbital parameters common to both satellites are an eccentricity of 0.001 and an inclination of 0.00001°, so that the orbits are nearly equatorial. These parameters were chosen merely for convenience, since the program can handle arbitrary orbits.

The perturbed relative velocity is shown aa function of time in Figures 19(a) through 19(e) in units of mm/sec, where the strength of a given one-degree by one-degree anomaly is 20π mgal. Figure 19(a) shows the signature of a single such anomaly and is very similar to the one shown in Figure 6(a). Figure 20(a) shows that, except for a slight underestimation of the peak anomaly strength and some side structure, the least-squares determined anomaly strengths agree well with the input values. The underestimation as well as the side structure is probably a consequence of our taking a point mass approximation in obtaining the design matrix while dividing the surface element into 9 subelements in the data simulation process. In any case the method has clearly determined where the central cause of the disturbance lies.

Figure 19(b) shows the signature of two such anomalies separated by one element with zero anomaly strength. An approximate doubling of the amplitude and a broadening of the peaks is observed, but it is far from obvious to the eye that there is a gap between the two anomalies. However, the fitting routine does see this difference, as the results plotted in Figure 20 demonstrate. The dual anomaly is clearly seen in plot 20(b) with excellent resolution. The same can be said for the next case, a dual anomaly separated by two zero-anomaly surface elements. The relative velocity signature for this case is shown in Figure 19(c) and the corresponding fitting results in Figure 20(c).

The rest of the plots in Figure 20 are further evidence that the basic software is working well in terms of discrimination, although there are some errors. Figure 19(e) shows the velocity signature of a gravitational dipole, in which there are two anomalies of opposite sign and equal strength separated by a single zero-anomaly element. Figure 20(e) shows this distribution to have been recovered quite well. The widely separated dual anomaly (eight degrees between non-zero anomaly elements) whose signature in Figure 19(d) clearly shows the two anomalies as separate events showed a little more noise in the fitted anomaly strengths. In restrospect it seems likely that the oscillations about zero seen in the fitted values of Figure 20(d) might have been reduced had we applied a more stringent cutoff on our allowed singular values. But prior to our experience with the more clearly linearly dependent results of the transverse surface and vertical linear arrays we had not been forced to examine this question since the fits for the longtitudinal arrays were good in general.

Figures 21(a)-21(e) show the perturbed velocity signatures for a Colombo configuration during the portion of the orbits for which the radial separation is at a maximum. The surface anomaly arrays are the same as those considered in the low-low configuration, the data for which are displayed in Figure 19, and they follow the same order in both sequences. It is immediately apparent that the velocity signatures are quite different in the two cases. This is largely due to the increased importance of the radial velocity components in the Colombo case.

For our parameters the maximum radial separation is around 140 km. There is essentially no angular separation in this case. The lower satellite is at an altitude of around 175 km. We denote this the high-low case in the figures, but it should not be confused with the standard high-low case. Here we refer only to the high-low portion of the Colombo configuration orbit. The plots of Figure 22 show that, even though the velocity signatures are markedly different from those seen in the low-low case, the ability of the method to obtain least-squares fitted values that agree closely with the input values is nearly the same, with the low-low configuration holding a slight edge. Whether this slight advantage would hold up if one of the basis functions had been eliminated remains to be seen. Time did not permit our running the various cases again with the cutoff criterion found to be optimum in the transverse array cases. The fitted signatures, i.e. the signatures obtained by using the fitted anomaly values, are virtually indistinguishable from the simulated signatures in both low-low and high-low cases.

9. TRANSVERSE AND VERTICAL LINEAR ARRAY RECOVERY

Time did not permit an extensive investigation of anomaly recovery for cases where the surface anomalies are not arrayed along the projected satellite path. We do have some preliminary results to report, however, which illustrate both the added difficulties in unambiguously resolving transversely aligned anomalies and some features of the SVD routines that are useful in such cases.

Figure 23 shows the results for a number of cases of surface anomaly elements aligned perpendicular to the projected satellite path on the earth's surface for the same low-low orbit considered in the analysis of longitudinal linear arrays (Figures 19 and 20). This time the design matrix is determined for ten one degree by one degree surface anomalies at a single longitude. The display of simulated perturbed relative velocity data has been omitted for the standard low-low cases since they are qualitatively similar to the plots previously displayed for off-line anomalies. The comparisons of input anomaly distribution with least-squares fitted anomaly distribution follow the same format that was used in the longitudinal linear array studies, except that in some of the input/output comparisons there is more than one set of fitted anomaly values. These different sets of recovered anomaly distributions correspond to different choices of the singular value cutoff of the design matrix. Since the fits were judged to be sufficiently good to demonstrate the success of the fitting method in the previously analyzed cases of linear arrays aligned parallel to the projected orbital path, and since the ratio of largest to smallest singular value was in those cases less than 10^3 , no cutoff was made in either the standard low-low or Colombo configuration examples previously analyzed. In the present case of a transverse array, however, it was immediately apparent that a cutoff would be necessary to eliminate unreasonably large fitted coefficients for what were essentially null vectors in the space corresponding to the singular value decomposition. This was apparent both from the very poor success in recovering the input anomaly distribution when no cutoff was made and from the large ratio of largest to smallest singular value, which was in this case greater than 10^8 . The choice of singular value cutoff beyond which the singular basis functions are to be considered null depends on the accuracy of the simulated perturbed relative velocity data and on the machine accuracy of the computer. We did not make a systematic study of the accuracy of the ASTP integration, and we held the parameter which determines that accuracy fixed at a value that had been deemed sufficient for earlier work. Thus it is possible that significantly better fits might have been obtained with more accurate simulations. There is hardly reason to doubt, however, that our ASTP simulated data is as accurate as it could be expected for real data.

Figure 23(a) shows the results of the least-squares fitting for a single input anomaly five degrees from the projected satellite path, where two different singular value cutoffs have been used. Neither of these fits can begin to compare with those previously obtained for anomalies directly on the projected satellite path. They both show a broad peak more or less centered on the single input spike. The ratio of maximum singular value to minimum allowed singular value is indicated by the Greek letter tau in these plots. There is not a great deal to choose from among these three different cutoffs. The 10^{-2} cutoff results show flatten out the peak more and shift it somewhat to a lower value. The fit obtained with $\tau = 10^{-3}$ was judged better than either of these having a peak of 3.5 at the central point of the distribution. It should be noted, however, that the fits obtained with a cutoff of 10^{-6} (not shown) were terrible. The 10^{-2} cutoff eliminates six of the ten singular basis functions.

Figures 23(b) and 23(c) show results of further fitting in the standard low-low configuration where $\tau = 10^{-3}$. In the one case a single anomaly nine degrees off-line served as input, and in the other case there were two anomalies, one on-line and the other nine degrees off. These fits, while definitely providing some information about the surface mass distribution, are again inferior to results obtained in the all-on-line cases. However, this is to be expected. Figure 23(d) shows the results of attempts to resolve a dual resonance with a single degree of separation. Again we see that the fit obtains a picture of the average mass distribution over dimensions larger than our surface elements.

In addition to the low-low configuration case of Figure 23(d), we obtained corresponding results for $\tau = 10^{-3}$ using the Colombo configuration analyzed before. Figure 24 shows the perturbed relative velocity signature for this high-low Colombo configuration.

Finally, we considered one case in which the anomaly lay beneath the earth's surface (on another surface at a lower radius). This was done for the Colombo configuration previously studied. The design matrix was obtained for a series of ten surface elements starting on the earth's surface and continuing downward at 100 km radial intervals. The case for which fits were obtained had a single anomaly 200 km beneath the earth's surface. The fitting was done for cutoff values corresponding to $\tau = 10^{-3}$ and 10^{-2}. These results are displayed in Figure 25. As in the transverse surface array case, the procedure fails to recover the sharp peak of the distribution. Although neither fit is a very accurate representation of the actual distribution, the $\tau = 10^{-2}$ has less negative overshoot at the greater depths below the surface.

10. CONCLUSIONS AND SUGGESTIONS FOR FURTHER STUDY

The major goal of this study has been accomplished. We have developed software for use in SSDT sensitivity/feasibility studies that is both simple and economical to use and which combines these features with considerable power of analysis. This was accomplished by obtaining numerical solutions to the linearized differential equations describing the perturbed velocity and position co-ordinates expressed in the most concise way. This reduction of six non-linear differential equations to four linear ones resulted in significant savings in computer time. The numerical solutions provide an advance over the standard Wolf equations which strictly apply only to circular orbits in which the satellite separation is small. Through the use of our software it is possible to consider arbitrary orbital configurations for SSDT ranging from the low-low configurations with optimum satellite separation to the high-low configuration in which only one satellite responds significantly to gravitational anomalies. The Colombo scheme, which is in a sense a hybrid form that combines the low-low and high-low configurations, is readily analyzed with this software as well.

By use of a least-squares fitting routine applied to data simulated by an independent integration of the full equations of motion we have demonstrated that one degree by one degree surface anomalies in the earth's gravitational field can be well resolved by the SSDT method when the anomalies lie directly beneath the path of the satellites in both the standard low-low configuration and in the Colombo variation. This was done for several different anomaly distributions.

Moreover, the singular value decomposition procedure used in the least-squares fitting provides an indication on when surface anomalies cannot be unambiguously resolved. In the case of a linear array of surface anomalies oriented perpendicular to the projected satellite path we found that the degree of resolution possible was considerably less than for an array parallel to the satellite path. In this case it was possible only to recover an anomaly smeared over several adjacent surface elements. A preliminary study of vertically (subsurface) aligned anomalies yielded similar results with respect to resolution and recoverability in the Colombo configuration.

Our study of signal strength as a function of satellite height and separation indicated that a separation of around six degrees appears to be optimum and that higher altitudes up to 300 km should still measure a sufficiently strong signal to detect 1 mgal anomalies. The Colombo scheme was shown to offer significant savings over the standard low-low scheme for a given value of perigee assuming a drag compensation system is utilized.

The Colombo scheme (described in detail in the body of the report) was found to match the standard low-low configuration in resolving power and anomaly recovery for a single pass over the surface of interest. An interesting comparison, that we did not have sufficient time to carry out, would be between two passes over the same surface area with the standard low-low scheme and two passes with the Colombo configuration in its two extreme modes of low-low and high-low. Such a study should be made with a variety of rectangular anomaly distributions. In particular, the resolving power of the two schemes should be tested when there is noise in the data, a factor which we have ignored in our preliminary studies.

We can conclude that our anomaly recovery analysis, although it must be considered only a first step (since we have taken into account only single linear arrays while ignoring complications such as noise, and we have neglected the possible "interference" of localized gravity anomalies with the higher-order harmonics of the Earth gravity field), it has provided nevertheless relevant deductions on the ability of the SSDT method, in its various configurations, to contribute significantly to the improvement of our understanding of the fine-grain features of the earth gravity field.

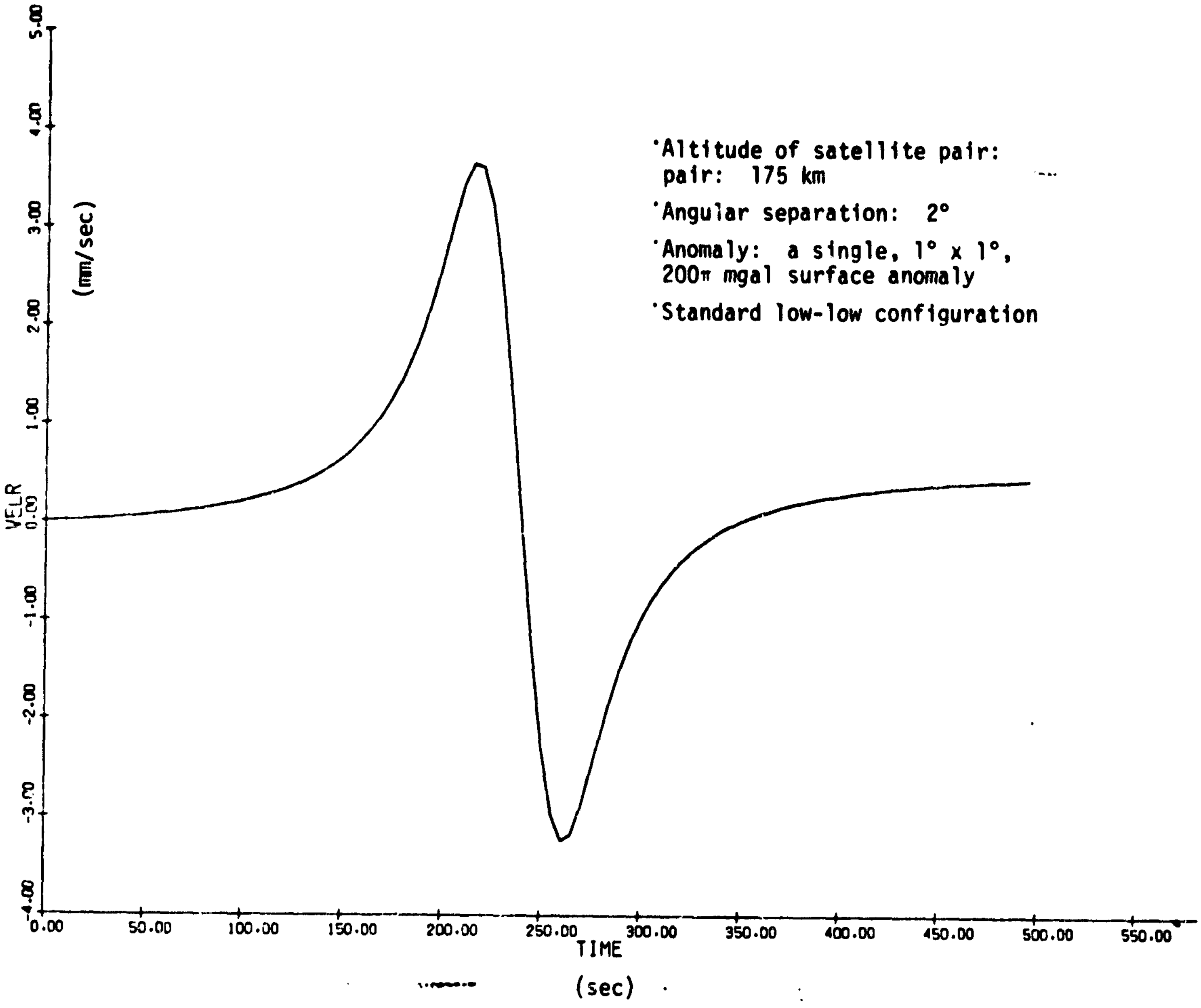

- Altitude of satellite pair: pair: 175 km
- Angular separation: 2°
- Anomaly: a single, 1° x 1°, 200π mgal surface anomaly
- Standard low-low configuration

Figure 1. First example of perturbed relative velocity signature (anomaly location: 0° from projected satellite path).

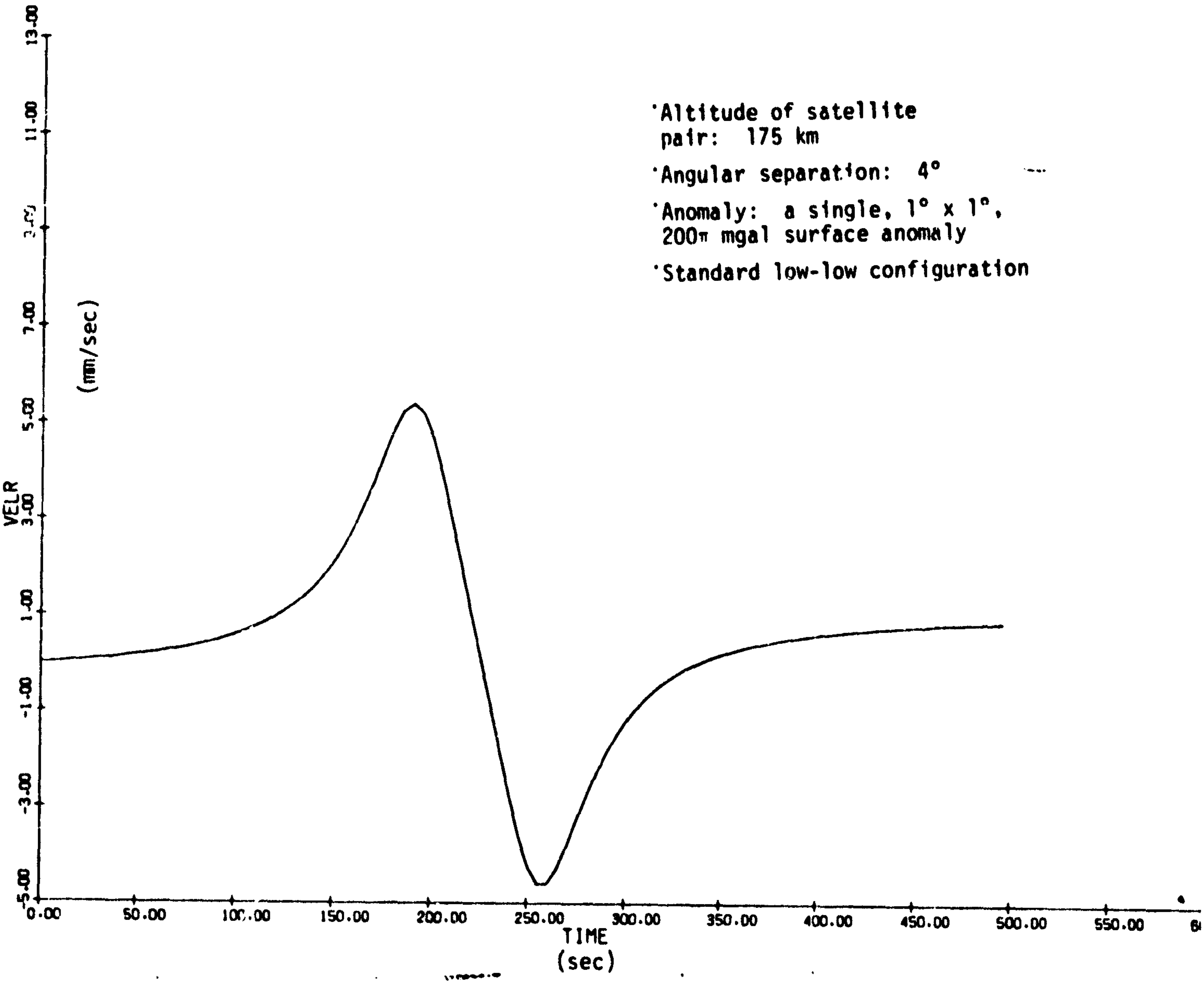

Figure 2(a). Second example of perturbed relative velocity signature (anomaly location: 0° from projected satellite path).

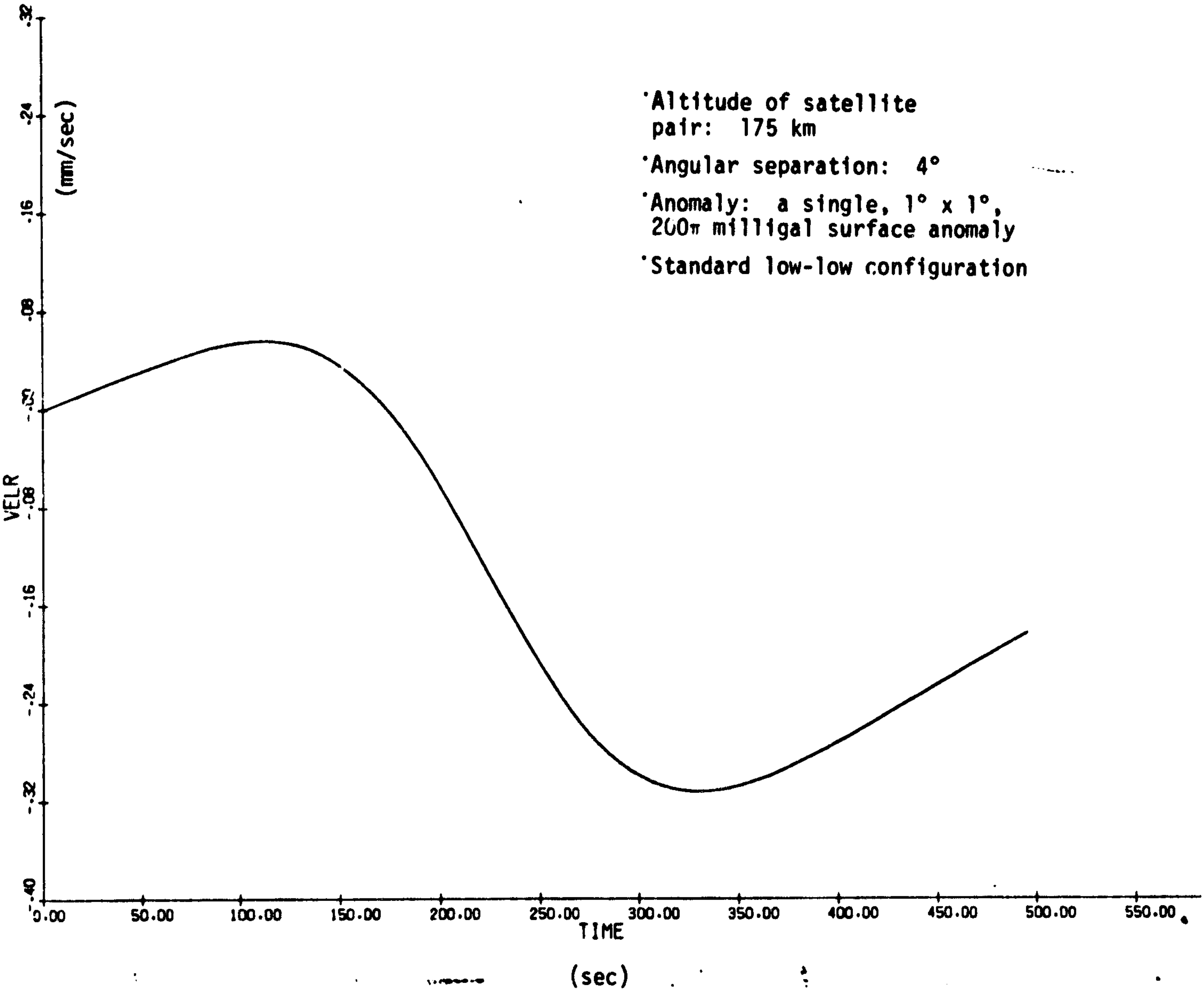

- Altitude of satellite pair: 175 km
- Angular separation: 4°
- Anomaly: a single, 1° x 1°, 200π milligal surface anomaly
- Standard low-low configuration

Figure 2(b). Example as in Figure 2(a), but with anomaly location 10° from projected satellite path.

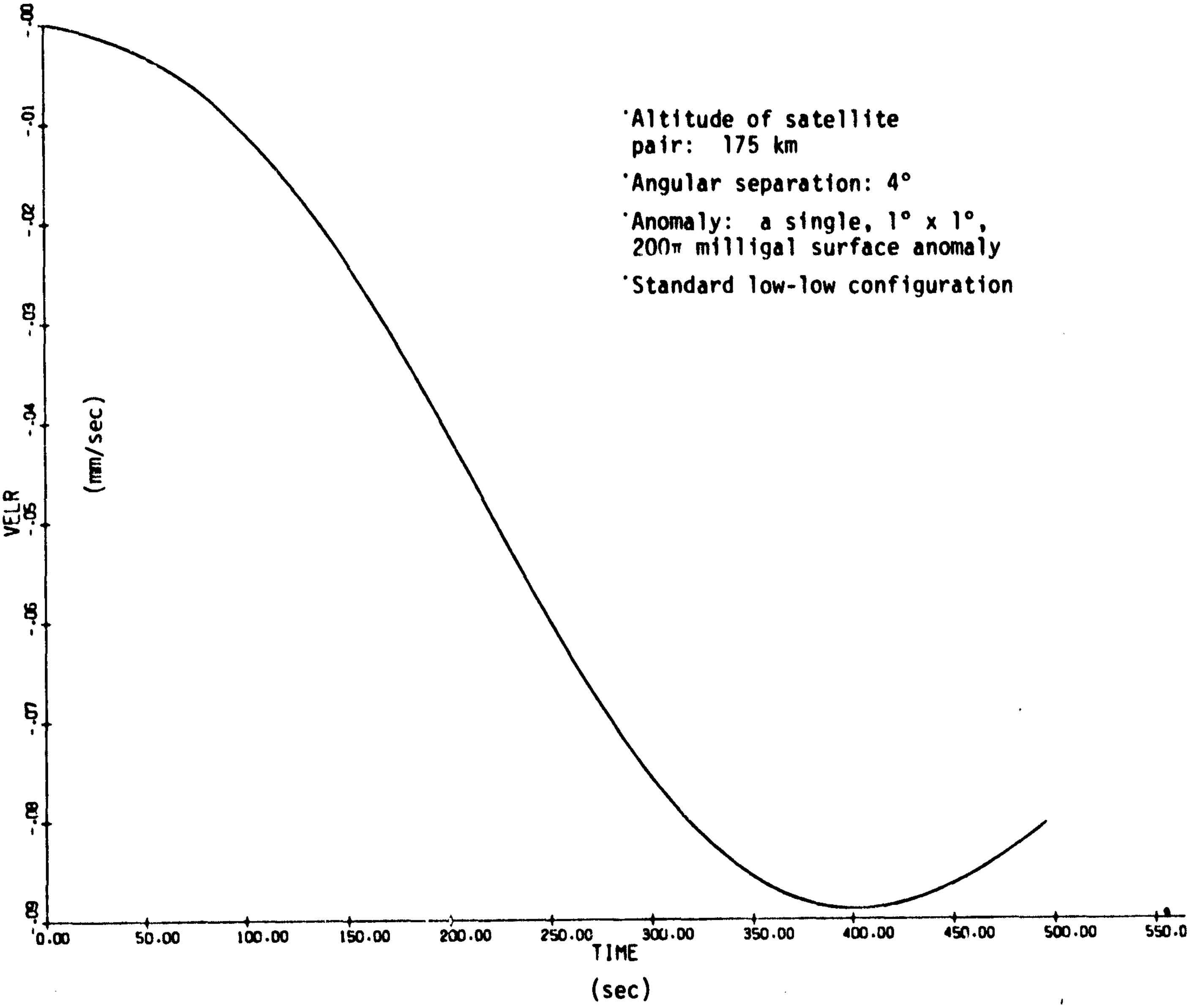

Figure 2(c). Example as in Figure 2(a), but with anomaly location 20° from projected satellite path.

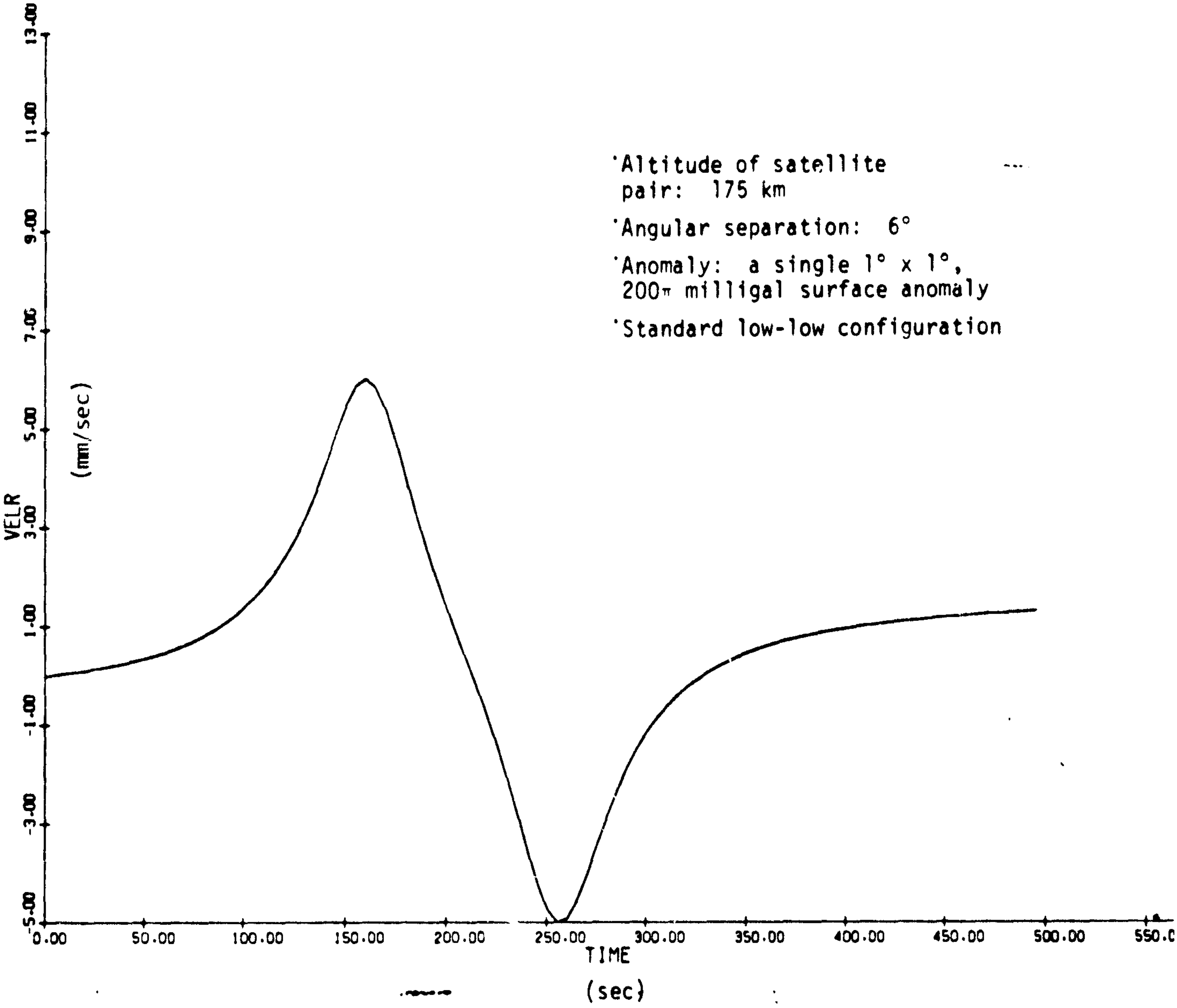

- Altitude of satellite pair: 175 km
- Angular separation: 6°
- Anomaly: a single 1° x 1°, 200 milligal surface anomaly
- Standard low-low configuration

Figure 3(a). Third example of perturbed relative velocity signature (anomaly location: 0° from projected satellite path).

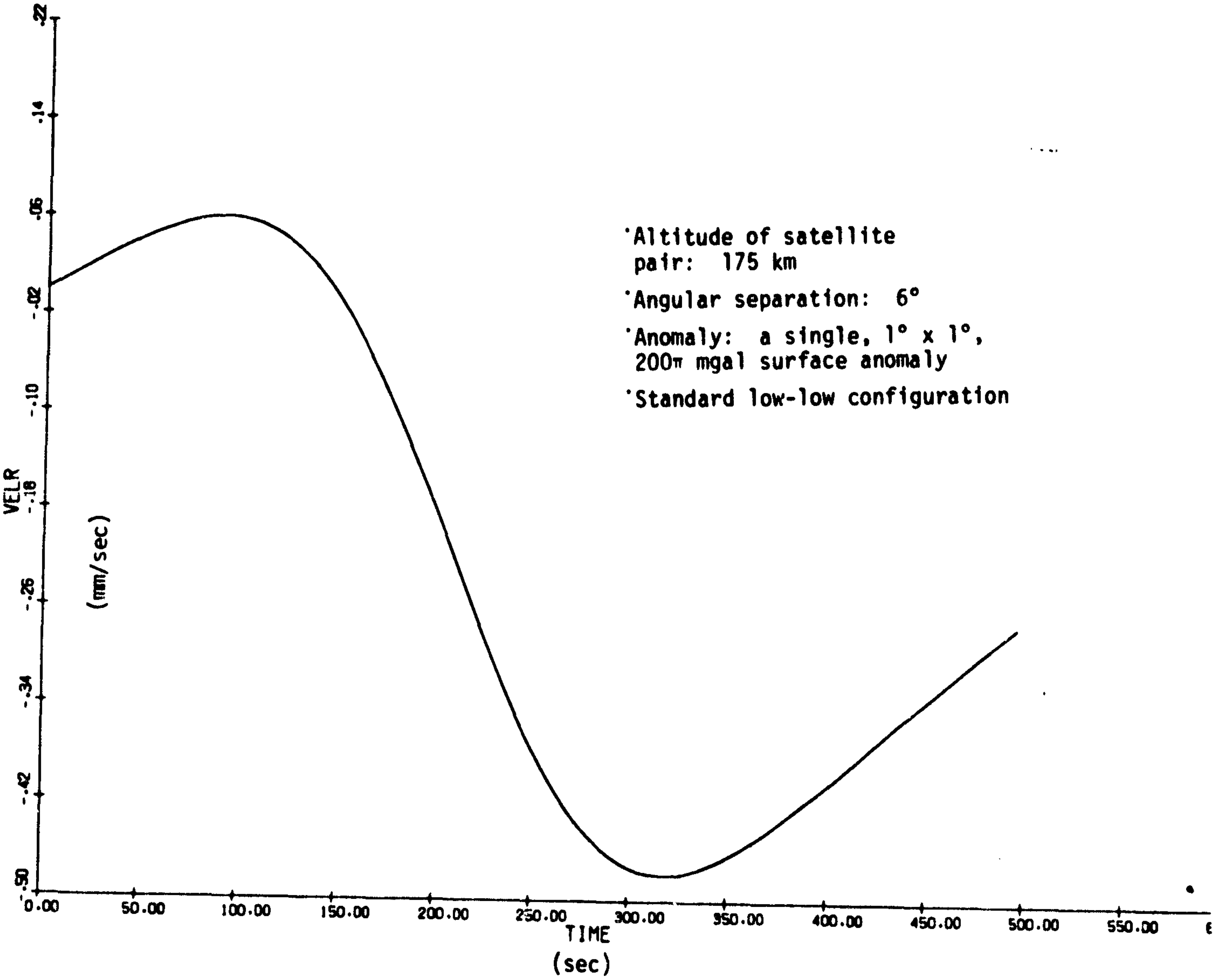

- Altitude of satellite pair: 175 km
- Angular separation: 6°
- Anomaly: a single, 1° x 1°, 200π mgal surface anomaly
- Standard low-low configuration

Figure 3(b). Example as in Figure 3(a), but with anomaly location 10° from projected satellite path.

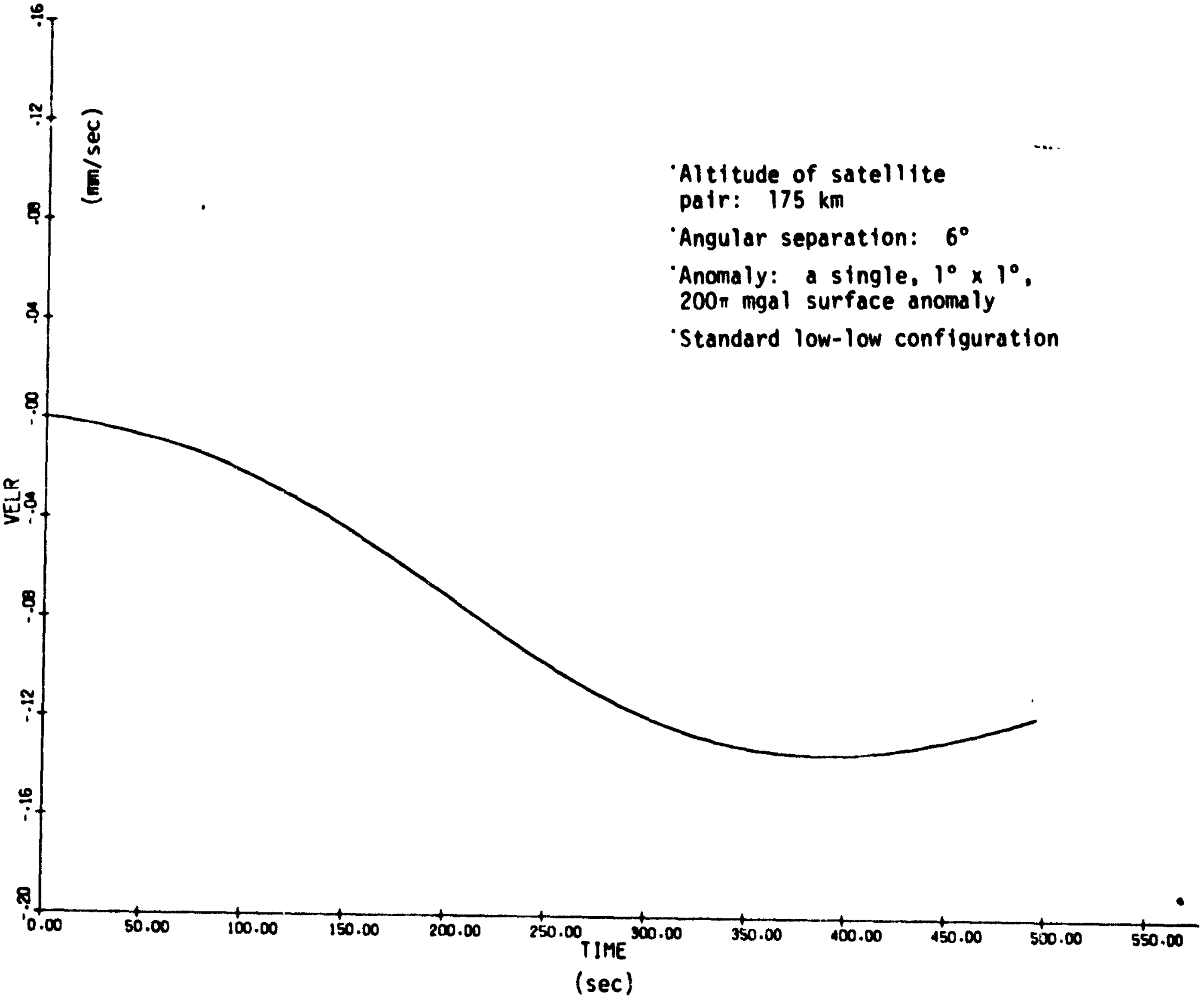

Figure 3(c). Example as in Figure 3(a), but with anomaly location 20° from projected satellite path.

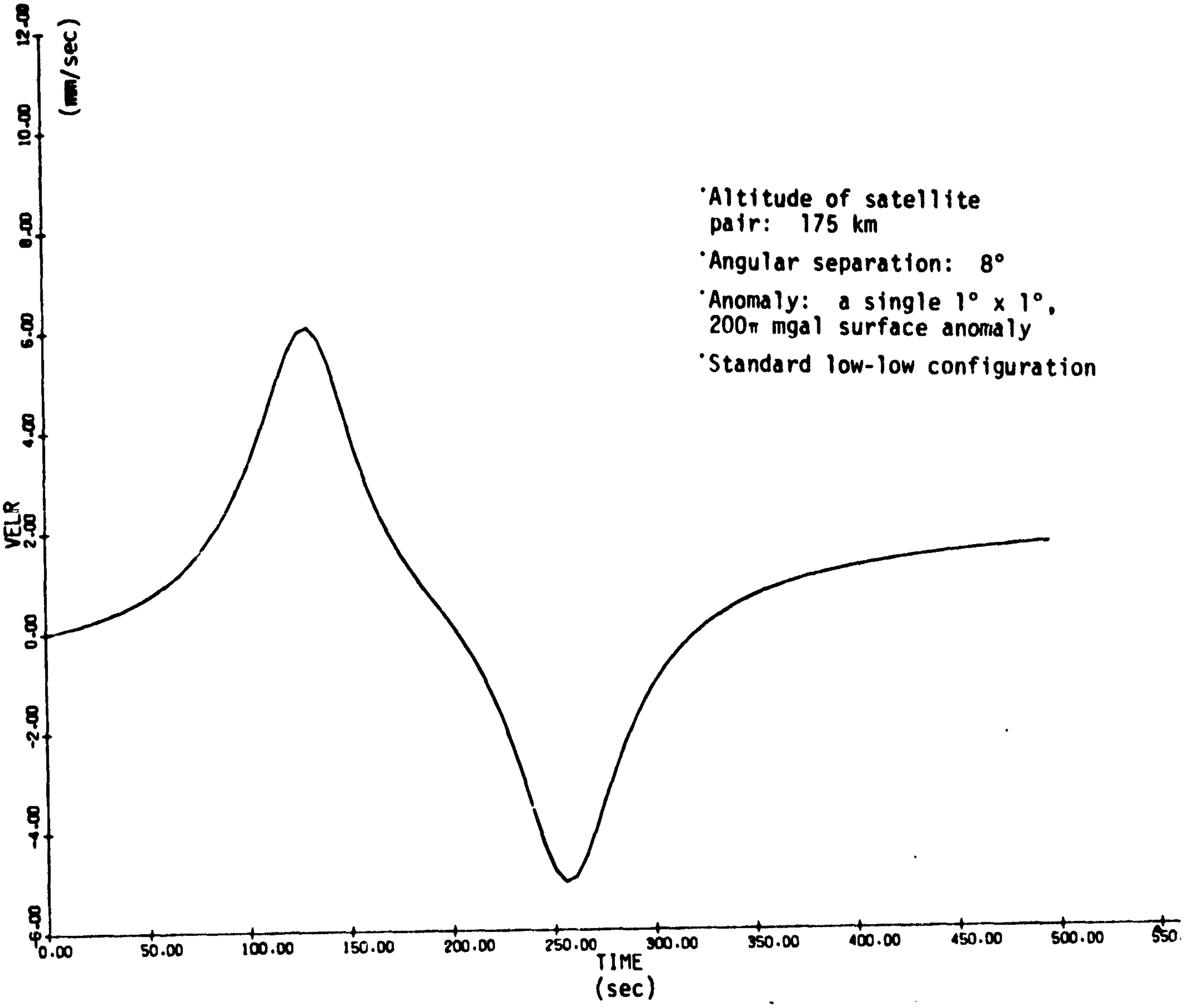

Figure 4. Fourth example of perturbed relative velocity signature (anomaly location: 0° from projected satellite path).

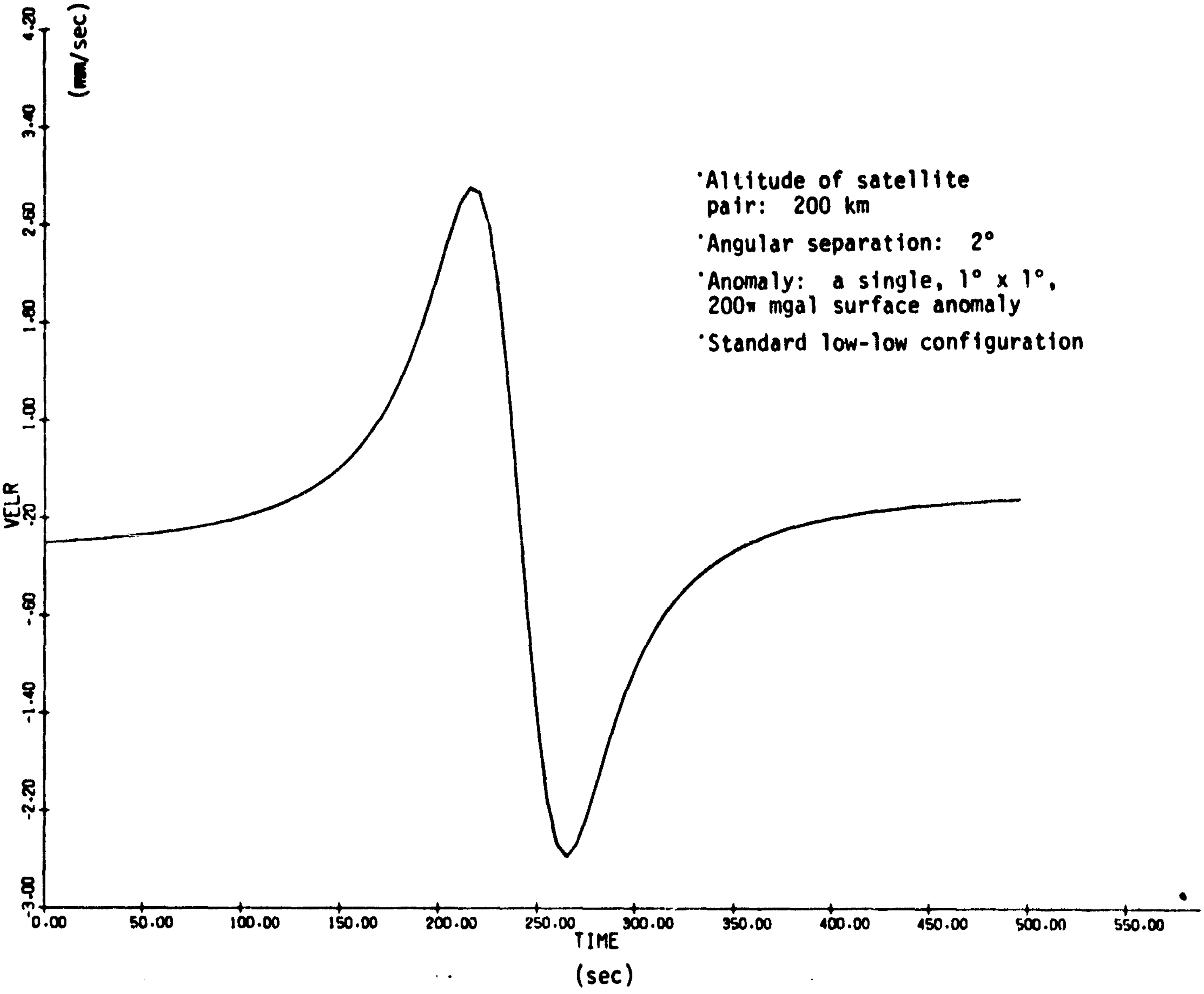

- Altitude of satellite pair: 200 km
- Angular separation: 2°
- Anomaly: a single, 1° x 1°, 200* mgal surface anomaly
- Standard low-low configuration

Figure 5. Fifth example of perturbed relative velocity signature (anomaly location: 0° from projected satellite path).

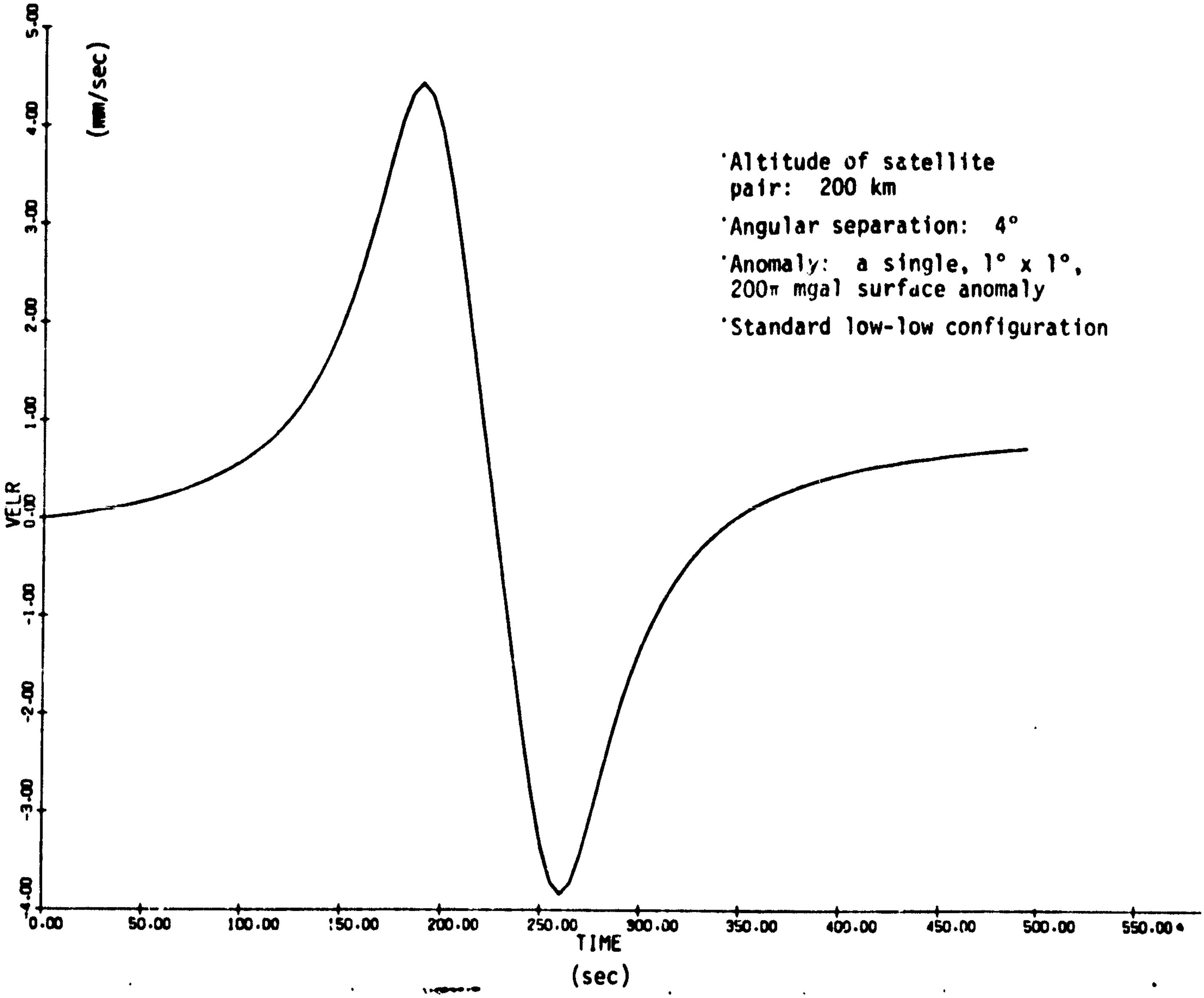

Figure 6(a). Sixth example of perturbed relative velocity signature (anomaly location: 0° from projected satellite path).

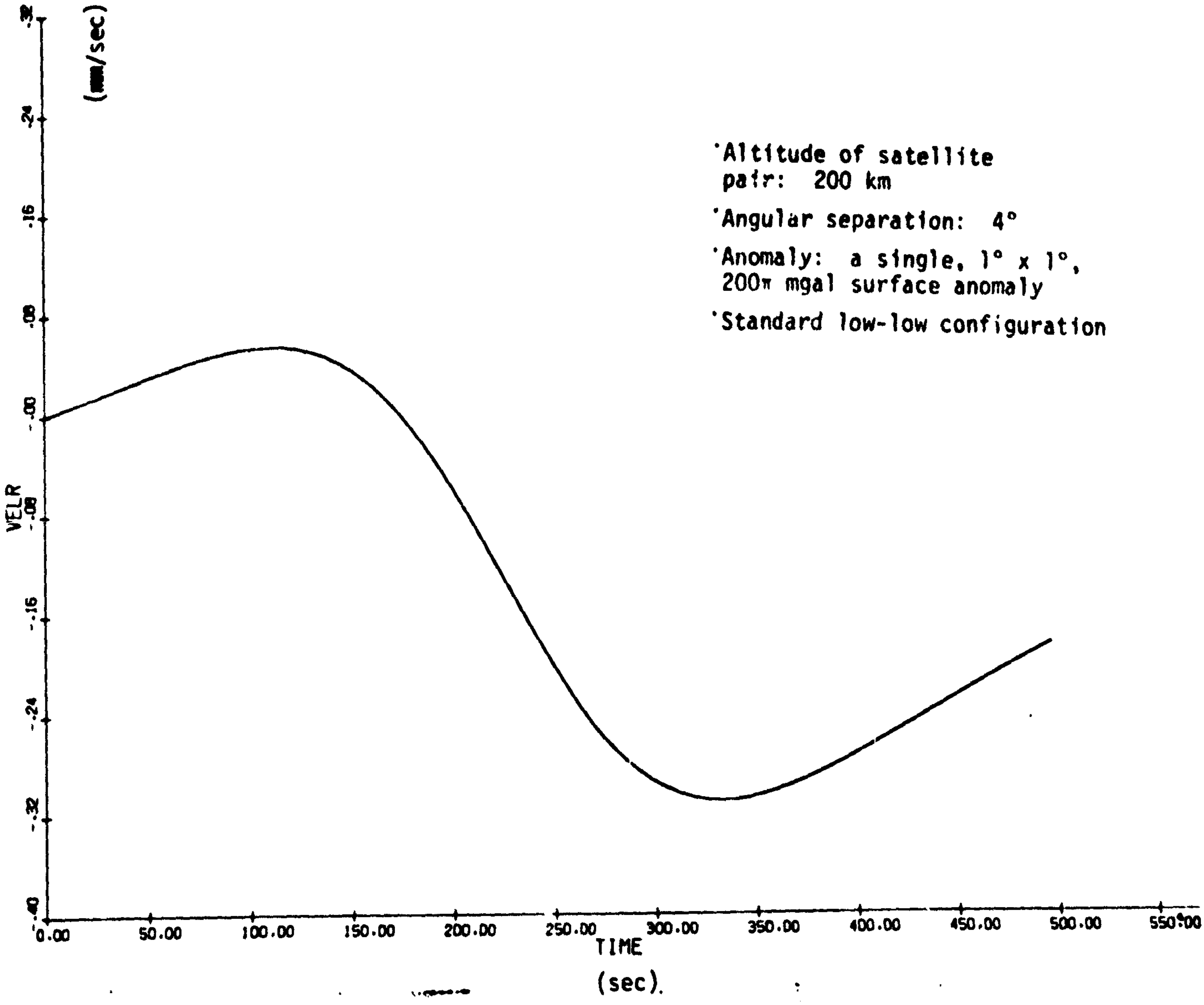

Figure 6(b). Example as in Figure 6(a), but with anomaly location 10° from projected satellite path.

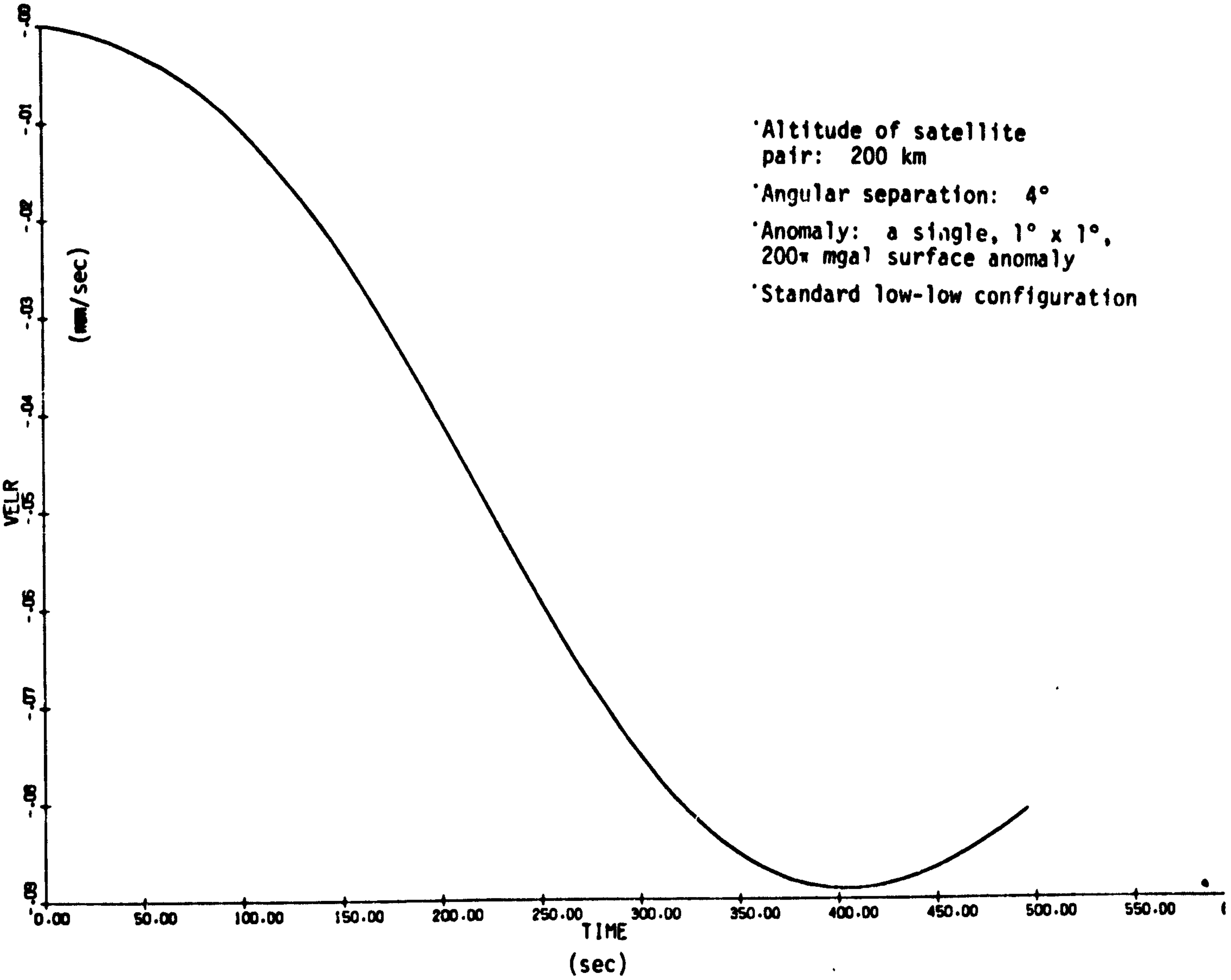

- Altitude of satellite pair: 200 km
- Angular separation: 4°
- Anomaly: a single, 1° x 1°, 200* mgal surface anomaly
- Standard low-low configuration

Figure 6(c). Example as in Figure 6(a), but with anomaly location 20° from projected satellite path.

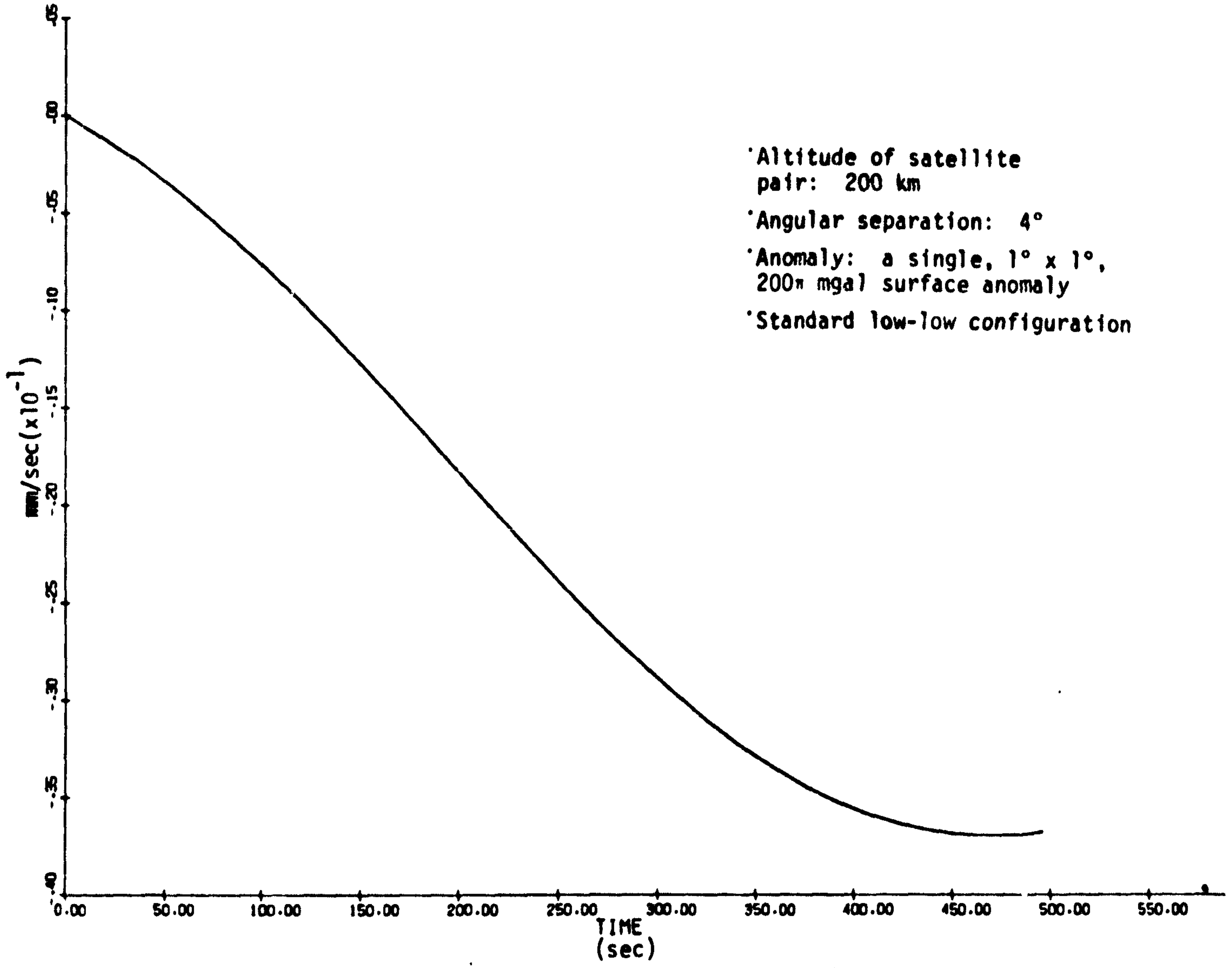

Figure 6(d). Example as in Figure 6(a), but with anomaly location 30° from projected satellite path.

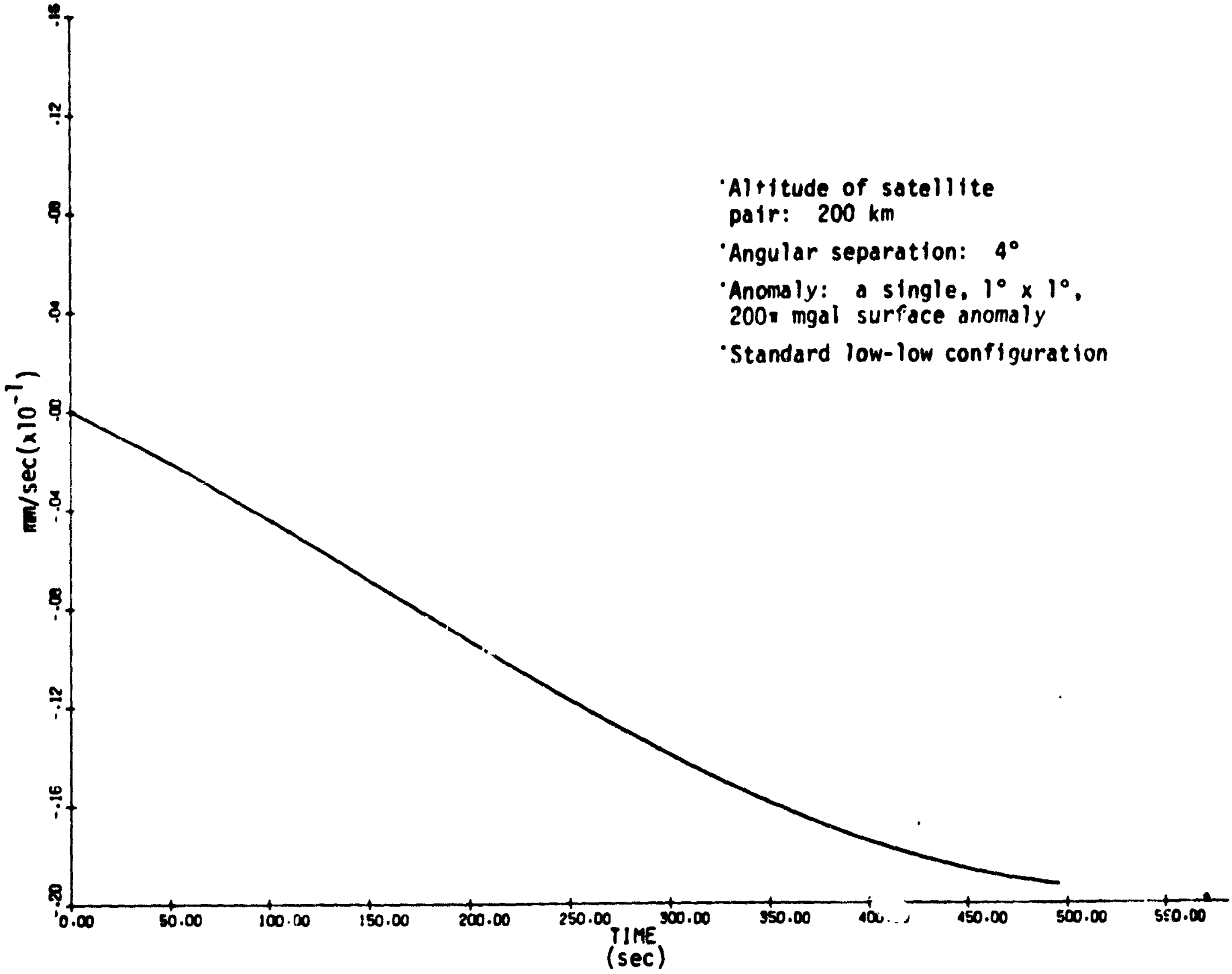

Figure 6(e). Example as in Figure 6(a), but with anomaly location 40° from projected satellite path.

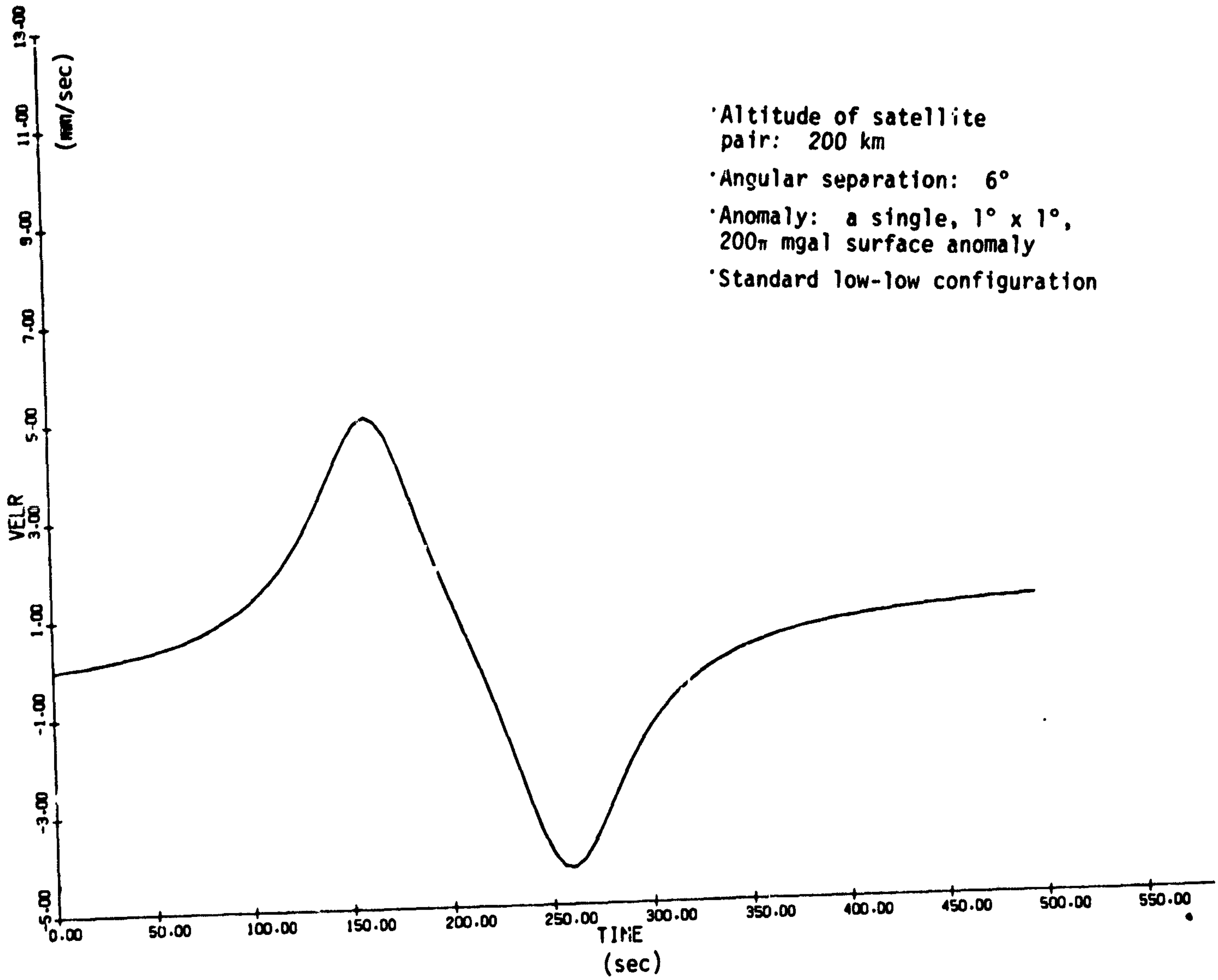

Figure 7(a). Seventh example of perturbed relative velocity signature (anomaly location: 0° from projected satellite path).

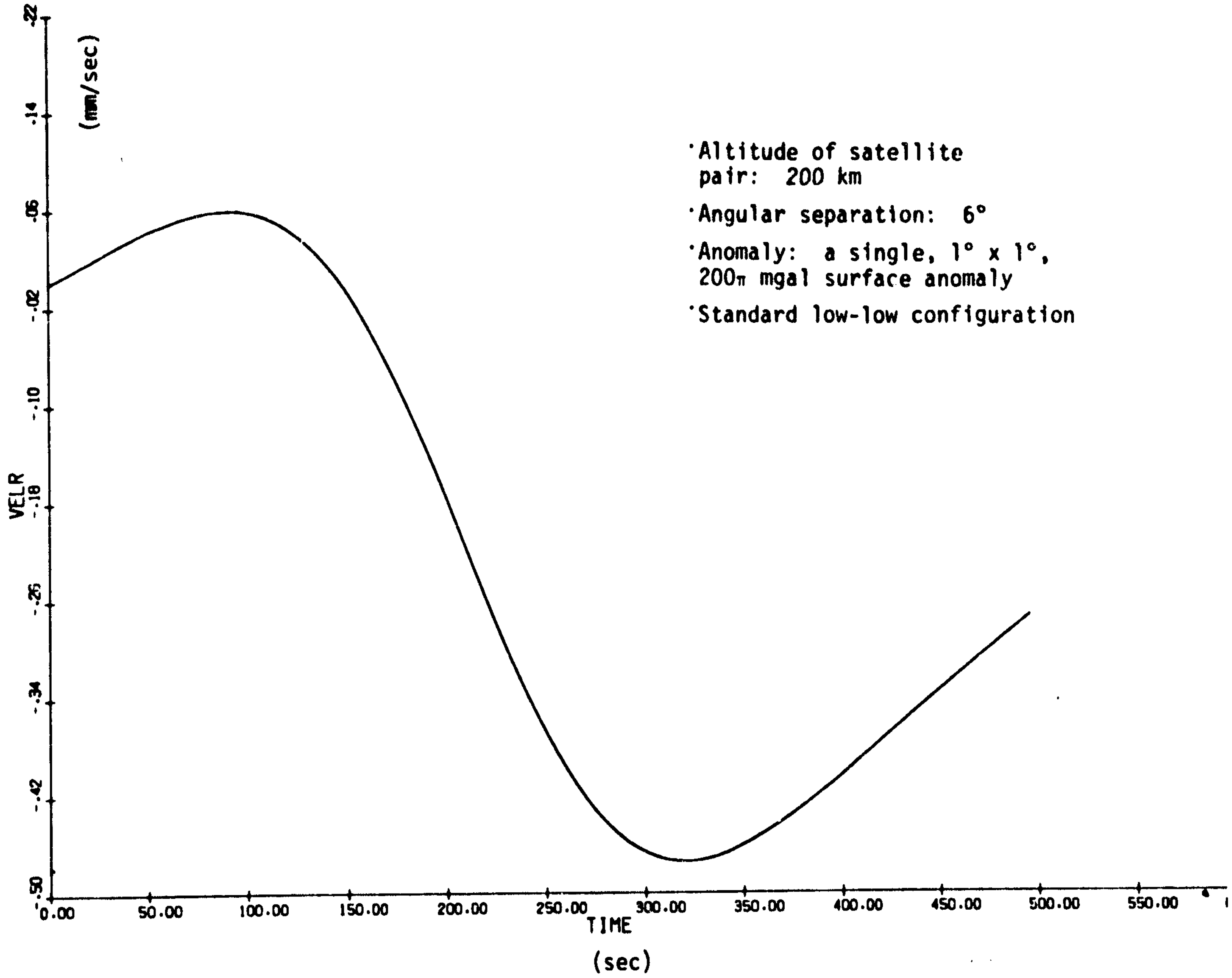

- Altitude of satellite pair: 200 km
- Angular separation: 6°
- Anomaly: a single, 1° x 1°, 200π mgal surface anomaly
- Standard low-low configuration

Figure 7(b). Example as in Figure 7(a), but with anomaly location 10° from projected satellite path.

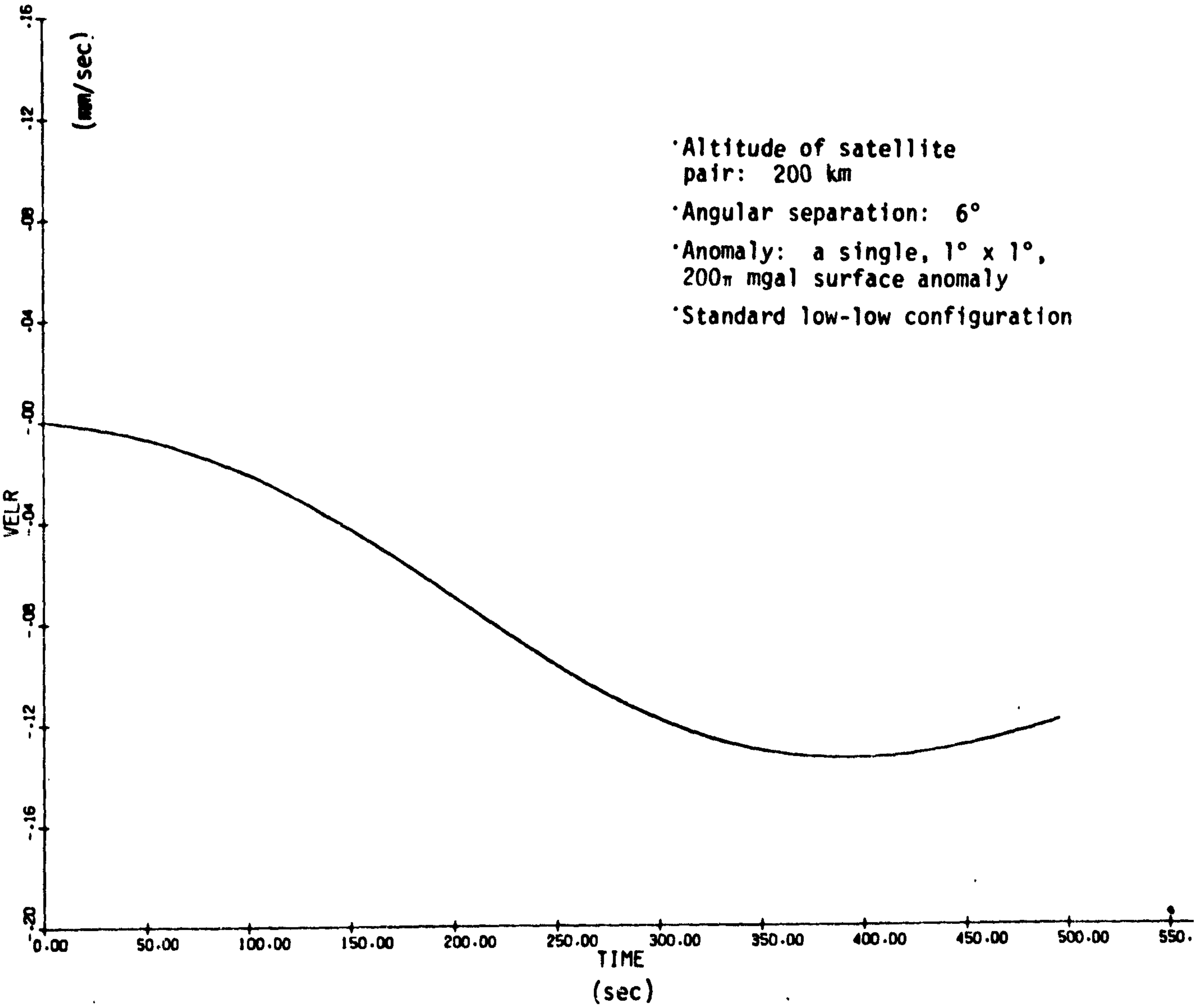

- Altitude of satellite pair: 200 km
- Angular separation: 6°
- Anomaly: a single, 1° x 1°, 200π mgal surface anomaly
- Standard low-low configuration

Figure 7(c). Example as in Figure 7(a), but with anomaly location 20° from projected satellite path.

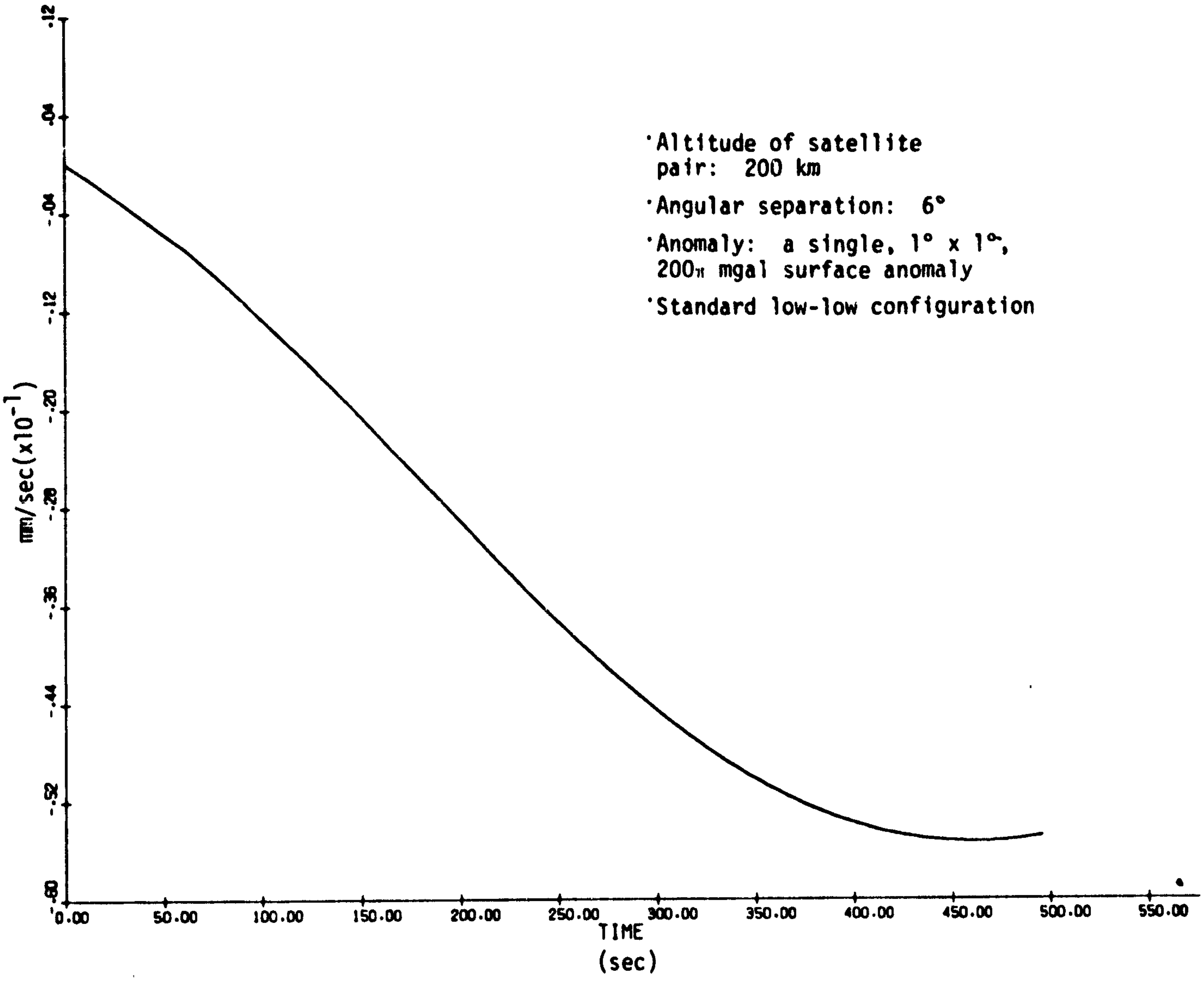

Figure 7(d). Example as in Figure 7(a), but with anomaly location 30° from projected satellite path.

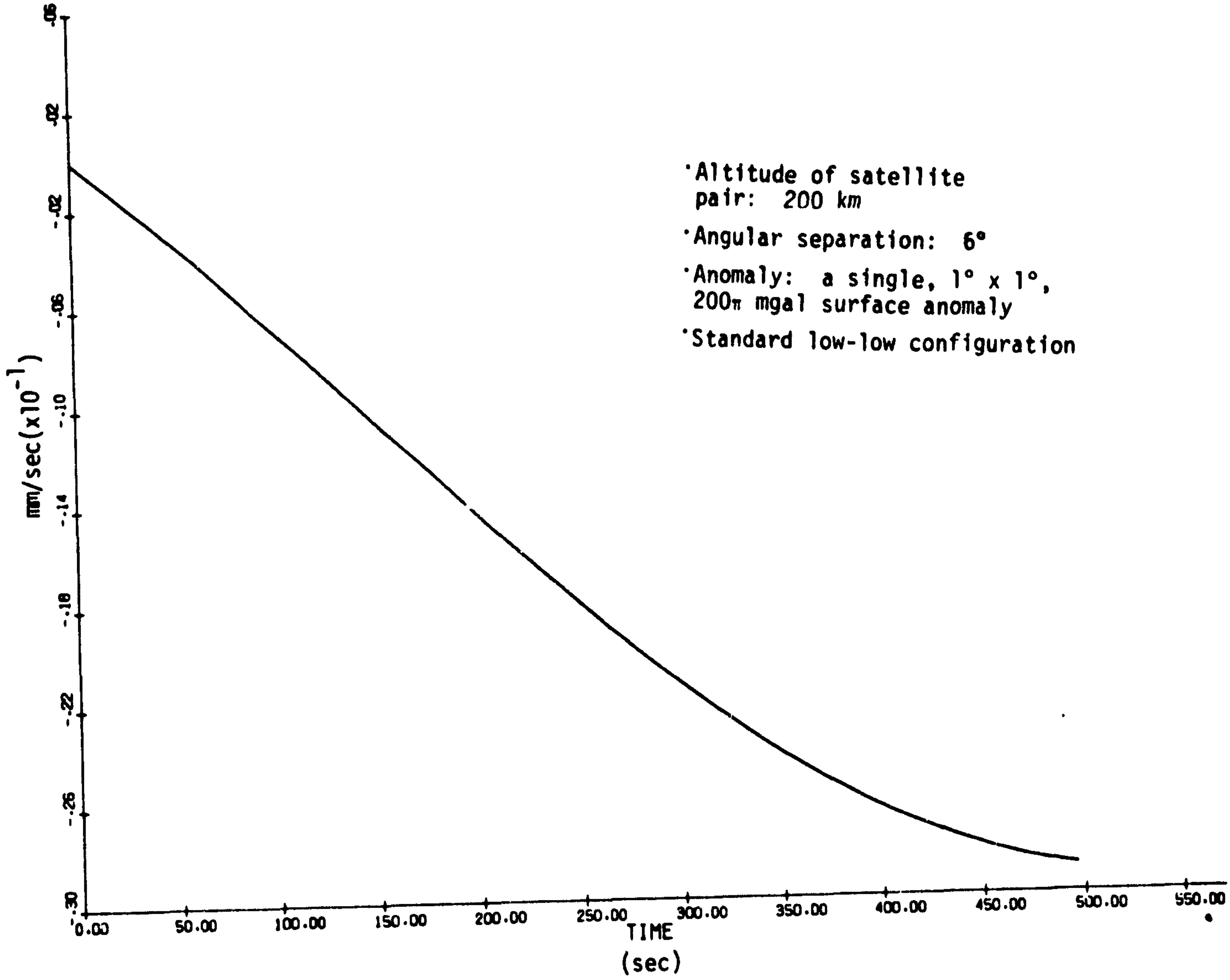

Figure 7(e). Example as in Figure 7(a), but with anomaly location 40° from projected satellite path.

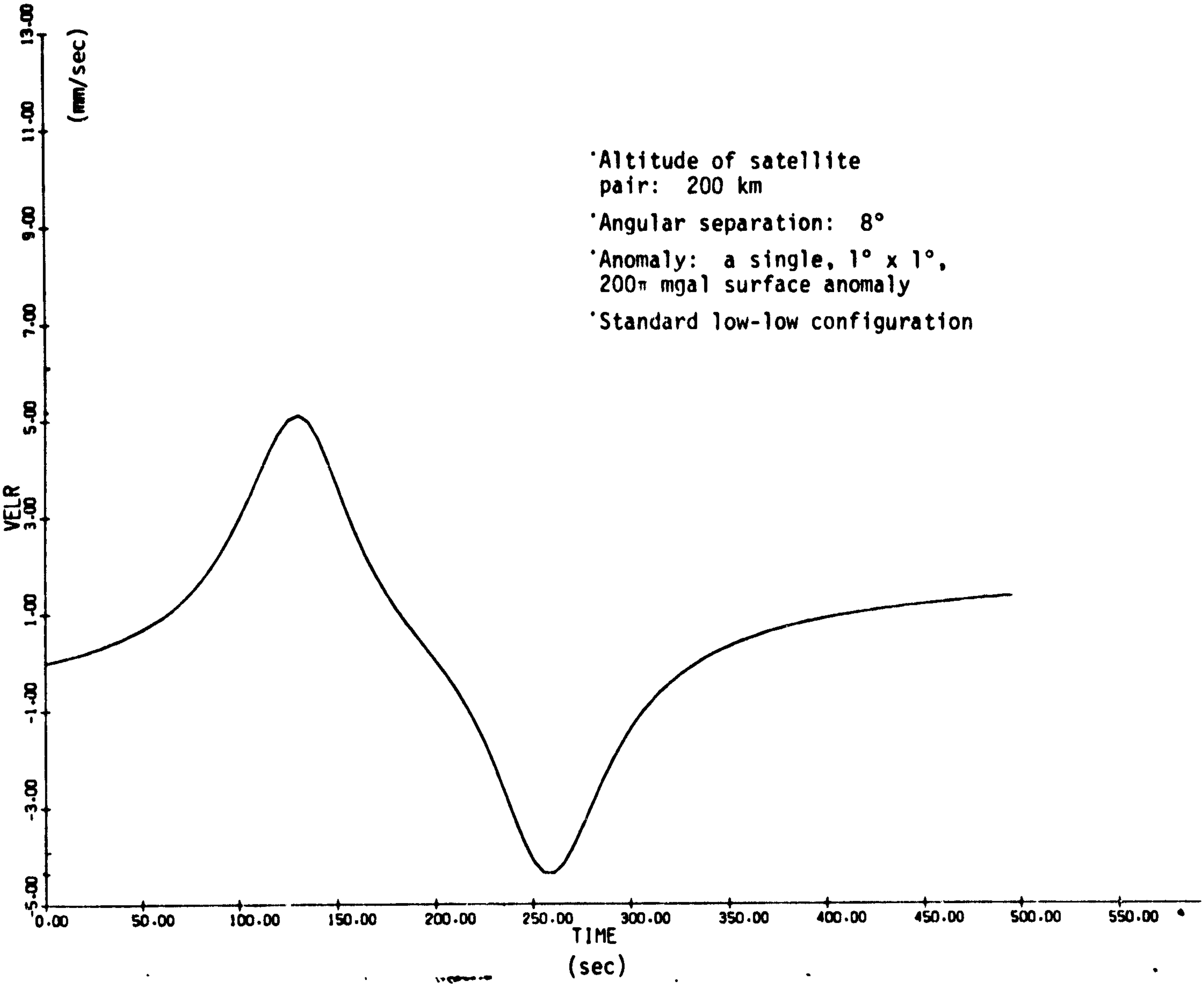

Figure 8. Eighth example of perturbed relative velocity signature (anomaly location: 0° from projected satellite path).

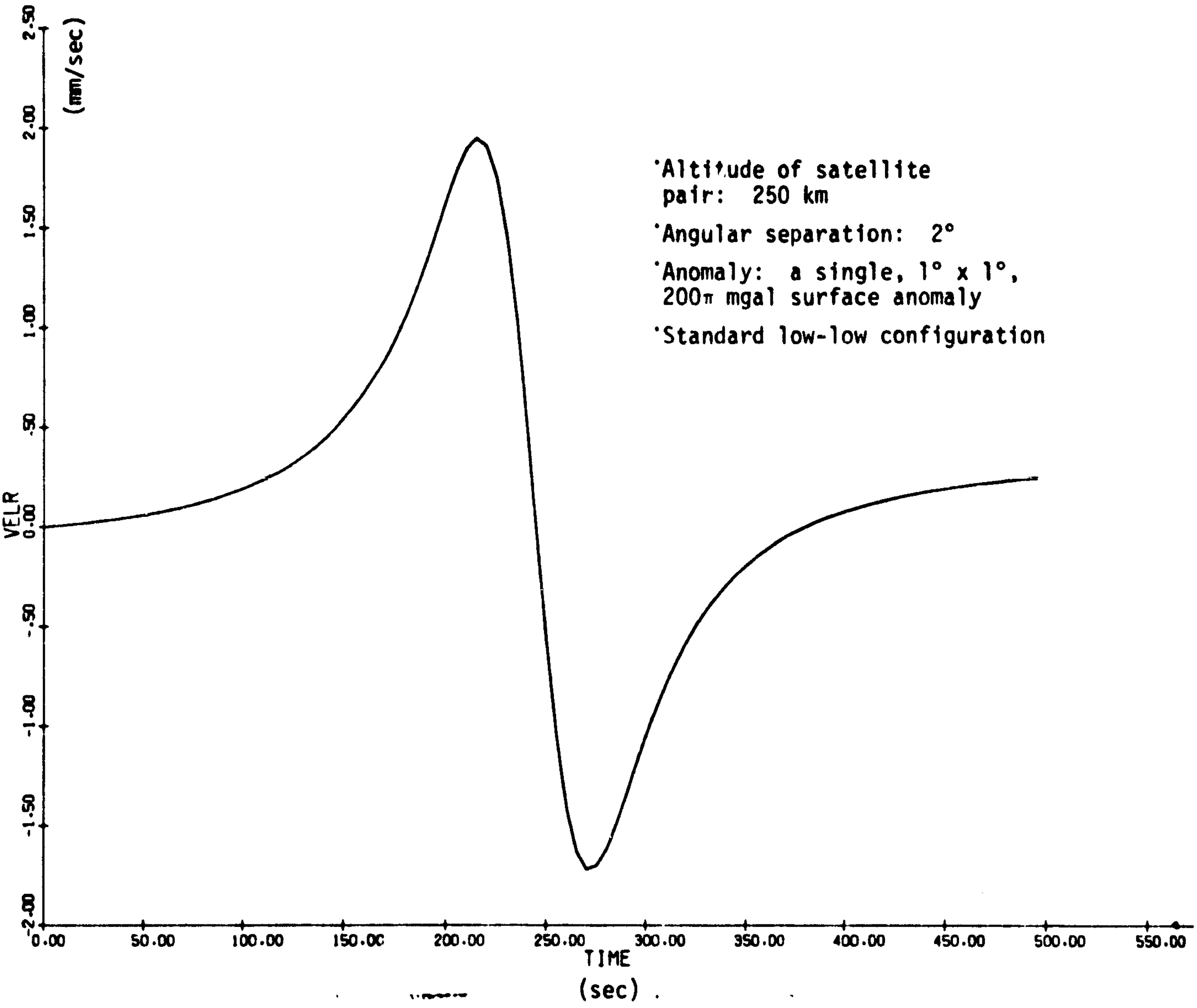

Figure 9. Nineth example of perturbed relative velocity (anomaly location: 0° from projected satellite path).

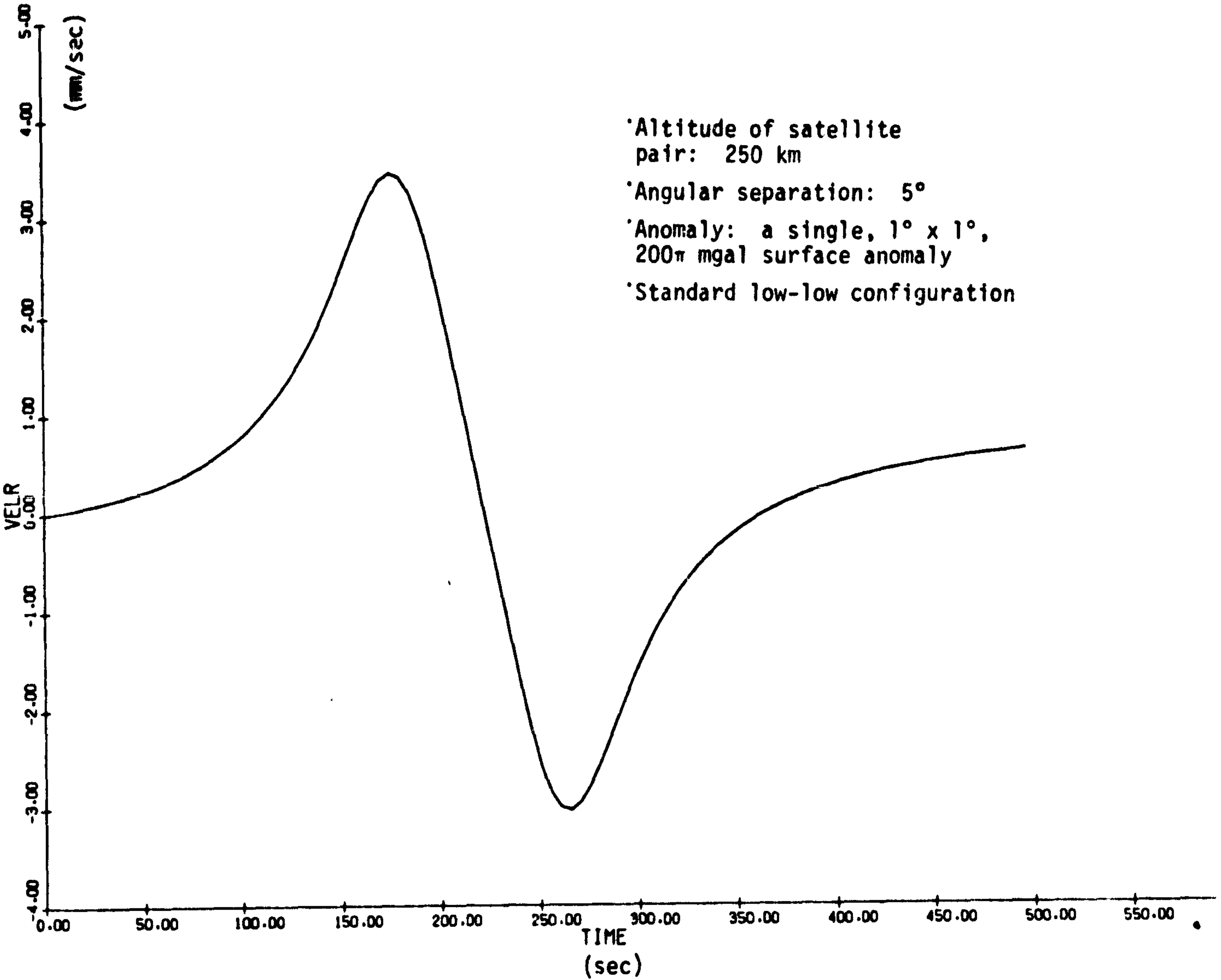

Figure 10(a). Tenth example of perturbed relative velocity (anomaly location: 0° from projected satellite path).

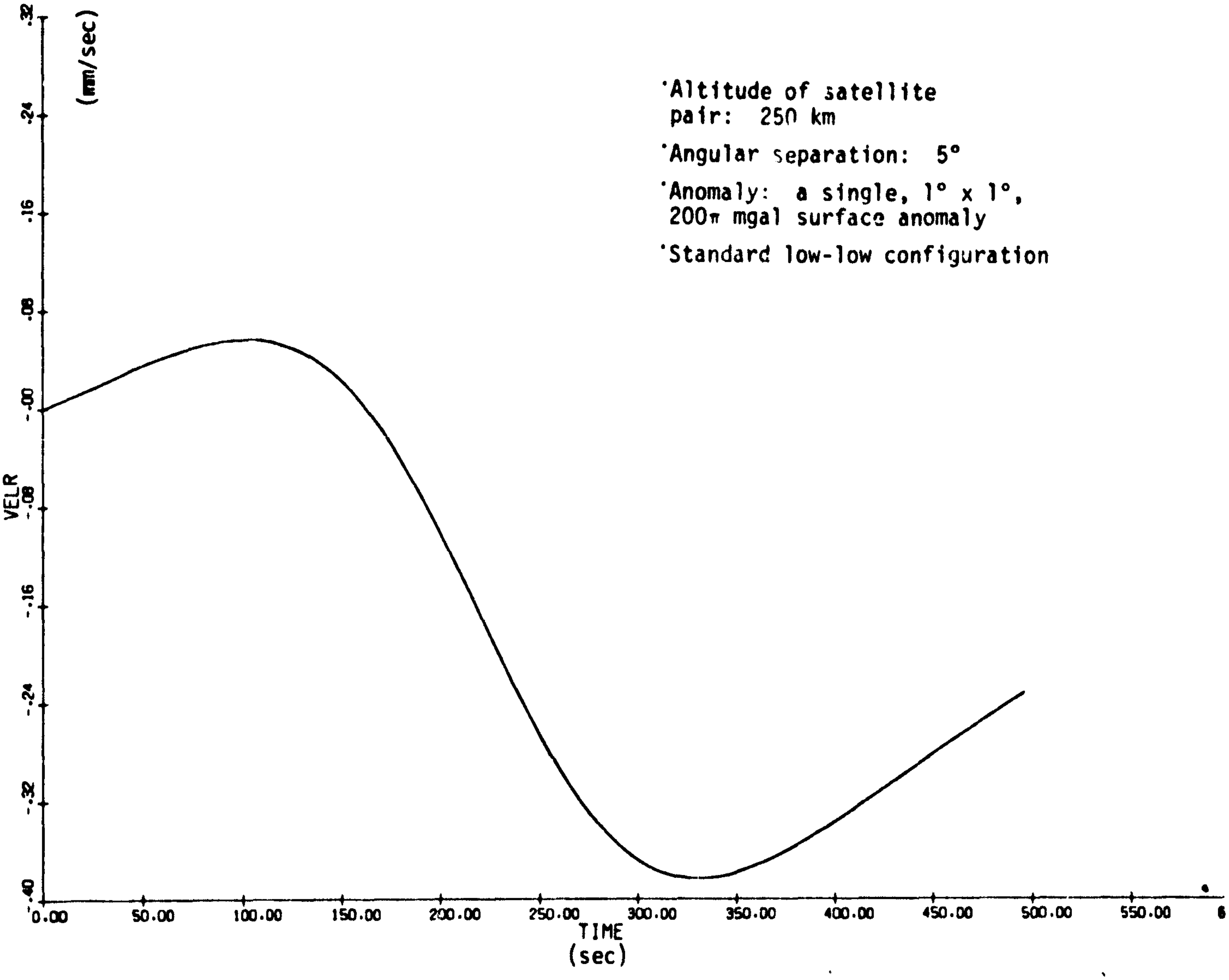

Figure 10(b). Example as in Figure 10(a), but with anomaly location 10° from projected satellite path.

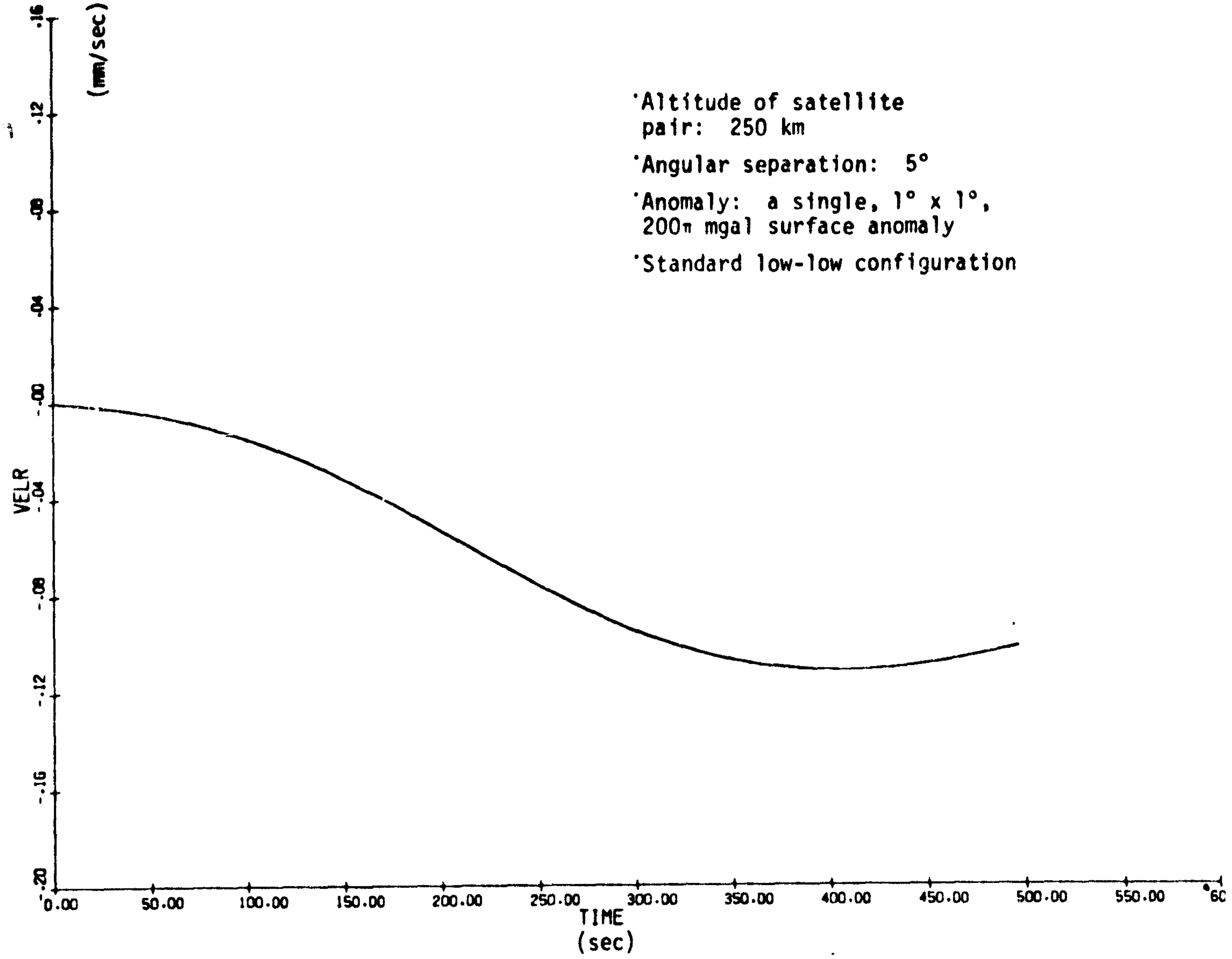

Figure 10(c). Example as in Figure 10(a), but with anomaly location 20° from projected satellite path.

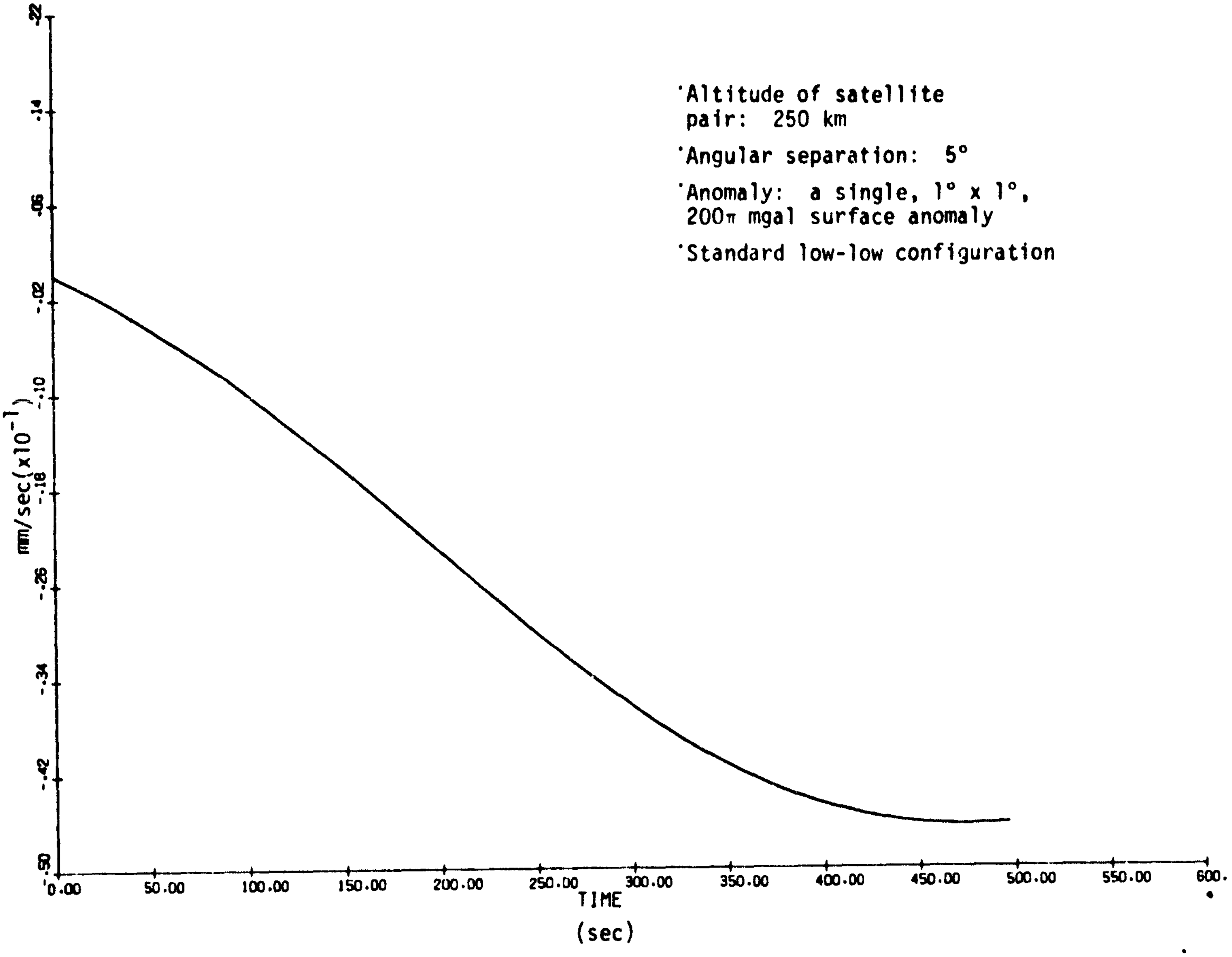

Figure 10(d). Example as in Figure 10(a), but with anomaly location 30° from projected satellite path.

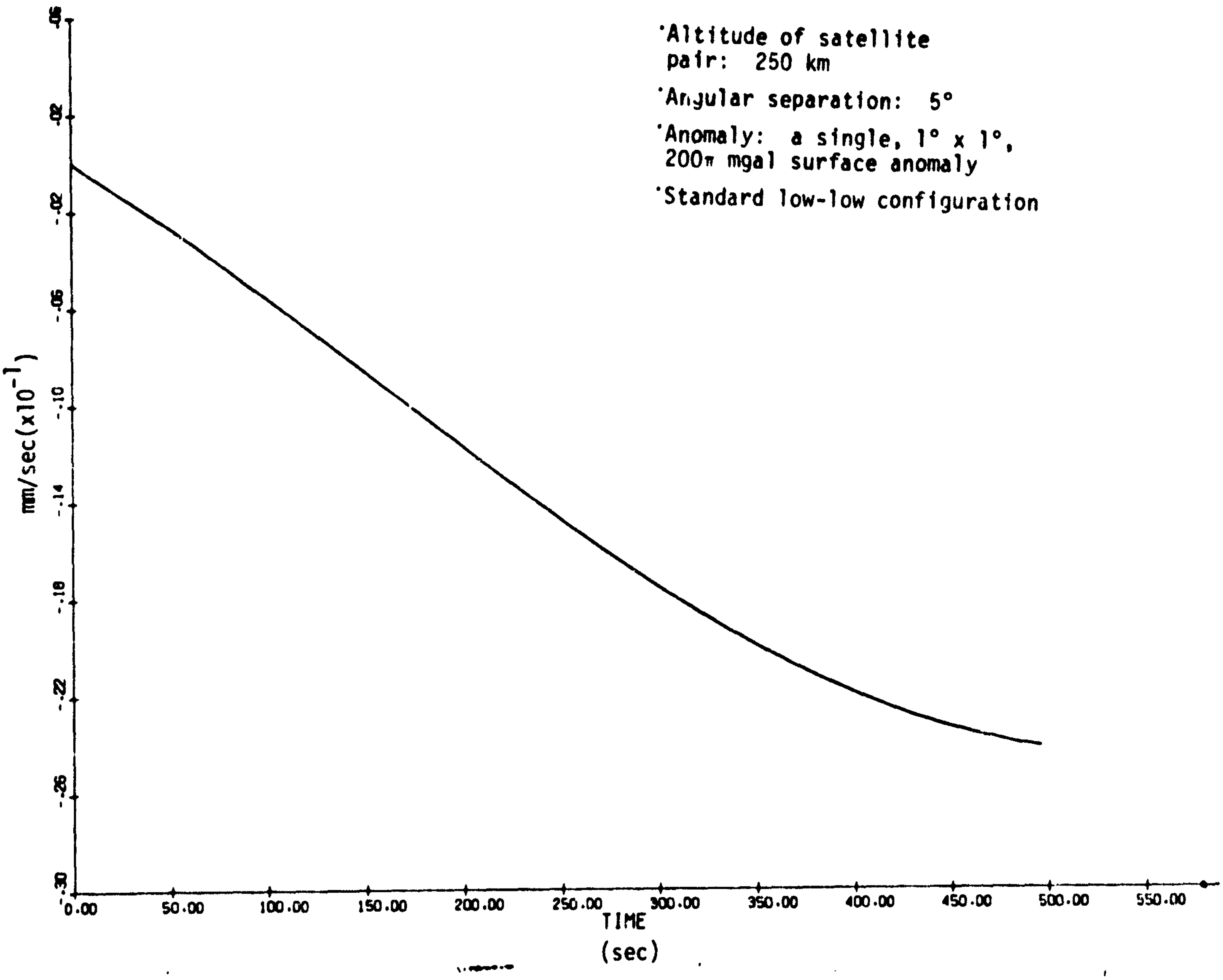

Figure 10(e). Example as in Figure 10(a), but with anomaly location 40° from projected satellite path.

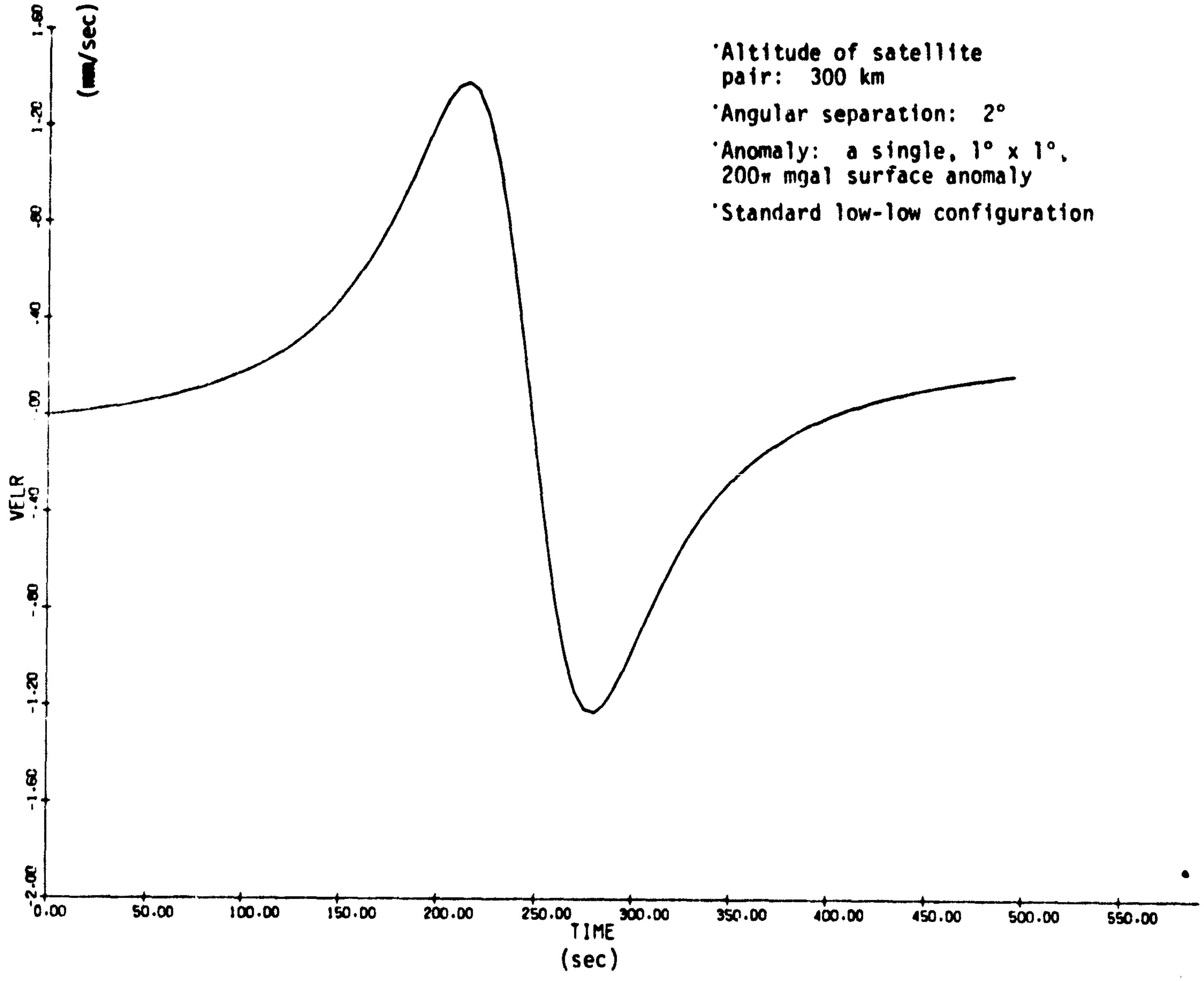

Figure 11. Eleventh example of perturbed relative velocity (anomaly location: 0° from projected satellite path).

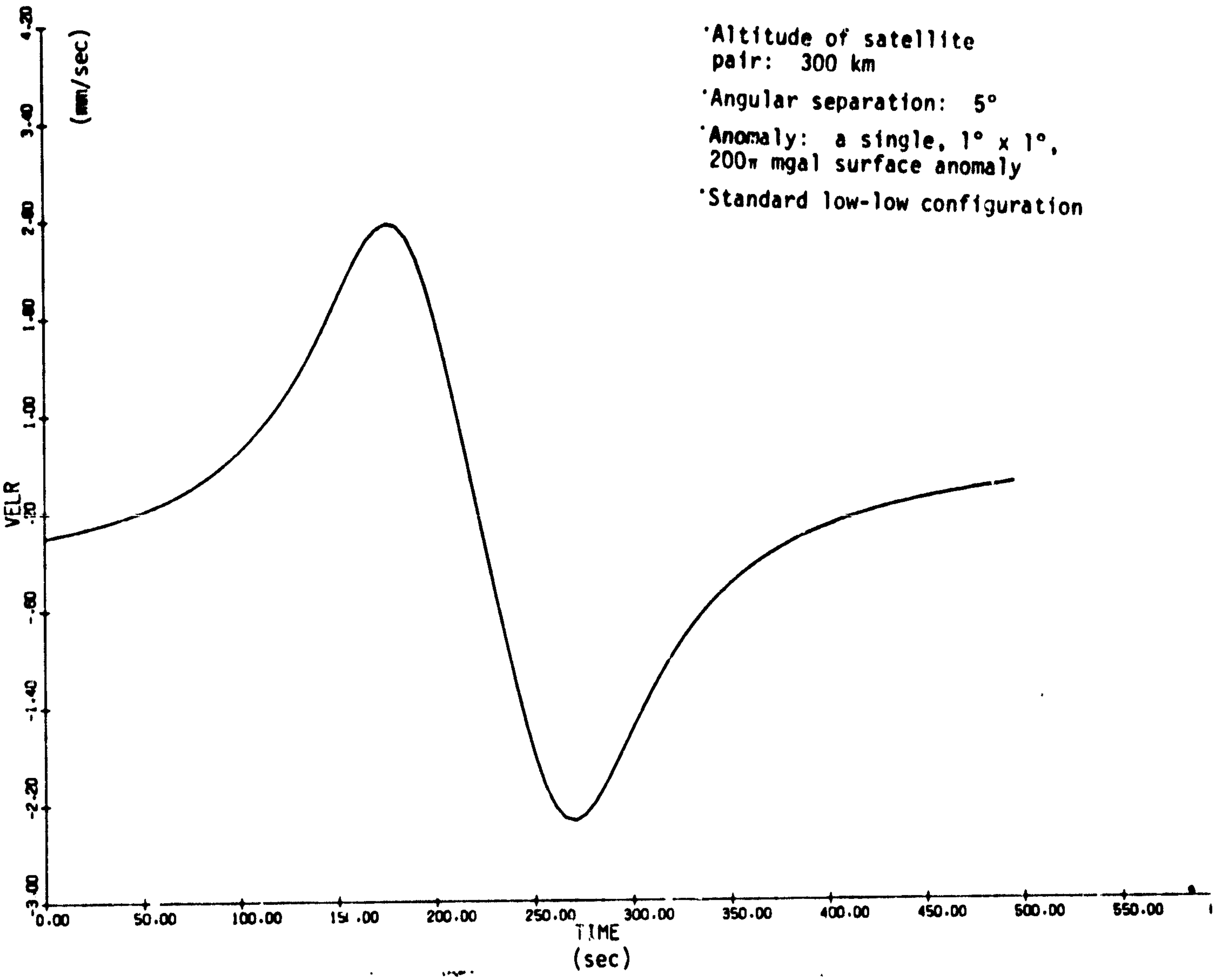

Figure 12(a). Twelfth example of perturbed relative velocity (anomaly location: 0° from projected satellite path).

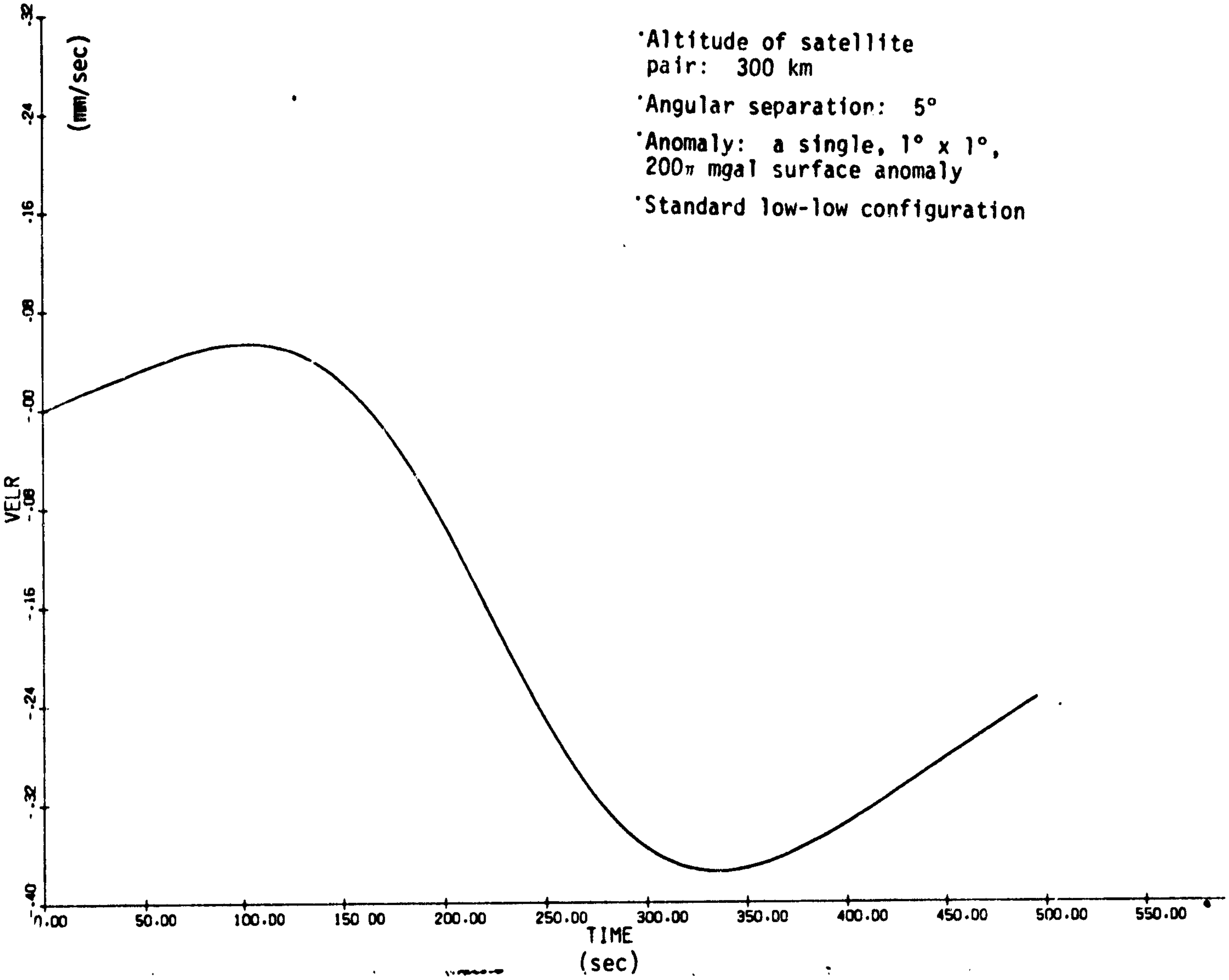

- Altitude of satellite pair: 300 km
- Angular separation: 5°
- Anomaly: a single, 1° x 1°, 200π mgal surface anomaly
- Standard low-low configuration

Figure 12(b). Example as in Figure 12(a), but with anomaly location 10° from projected satellite path.

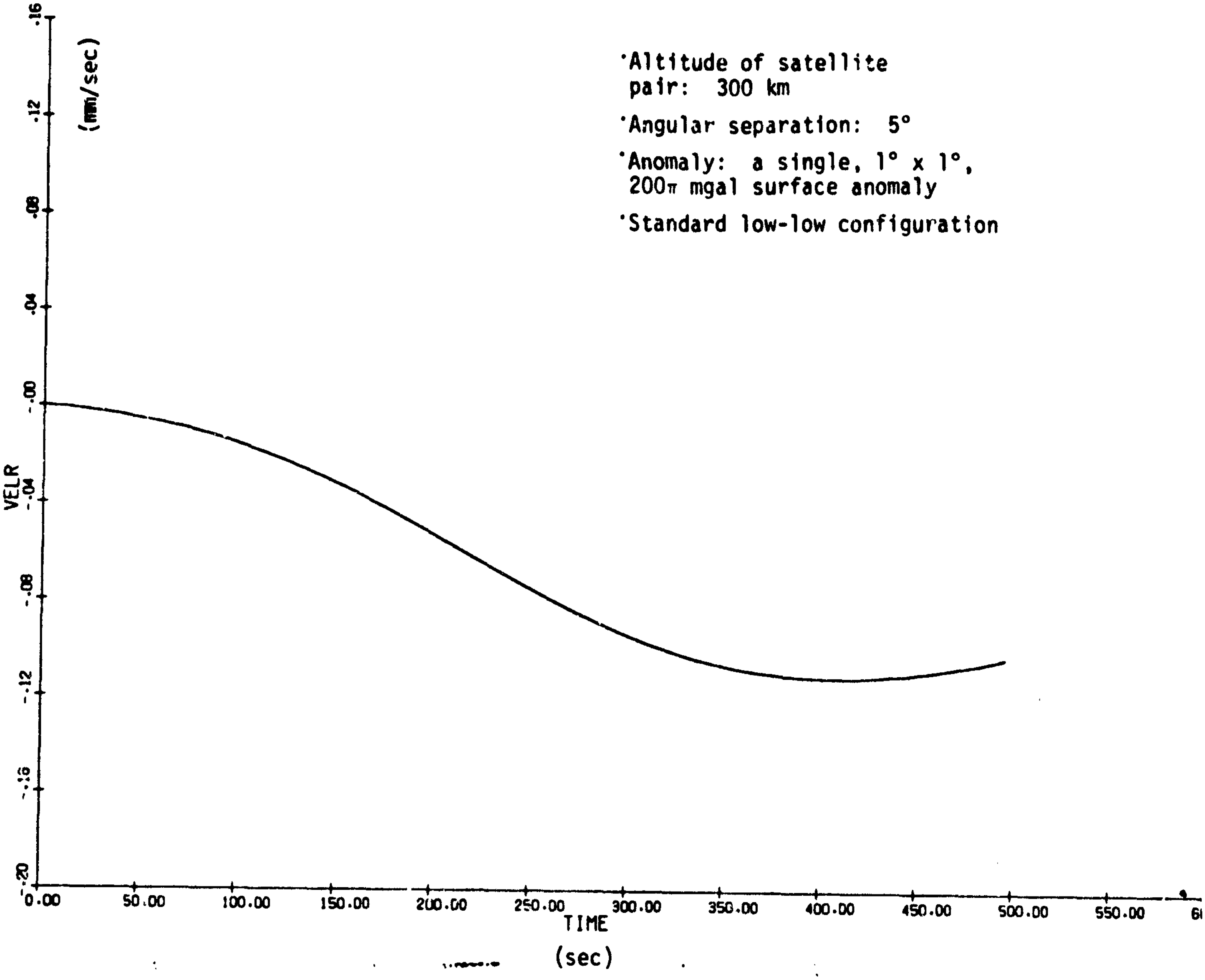

Figure 12(c). Example as in Figure 12(a), but with anomaly location 20° from projected satellite path.

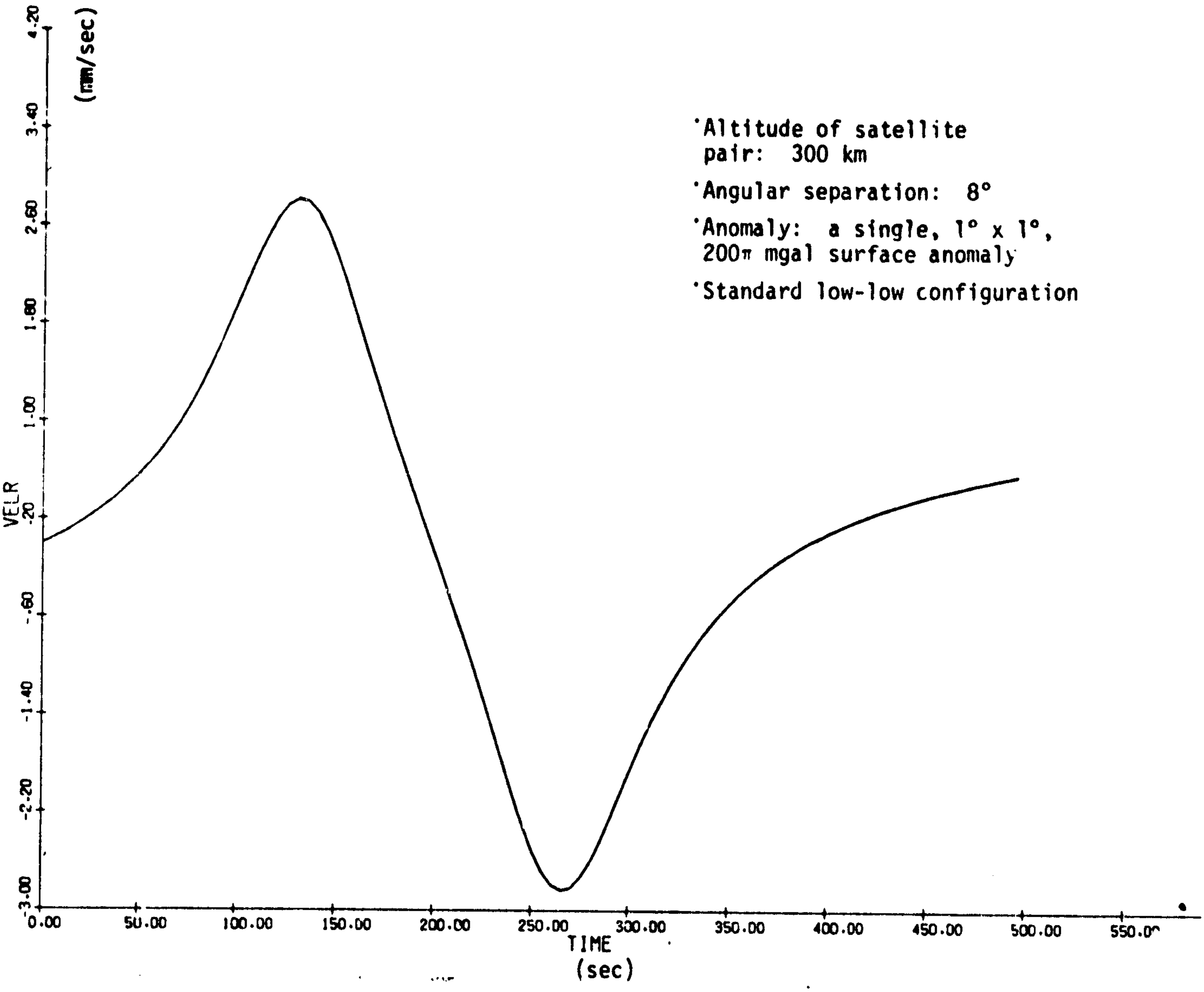

Figure 13. Thirteenth example of perturbed relative velocity (anomaly location: 0° from projected satellite path).

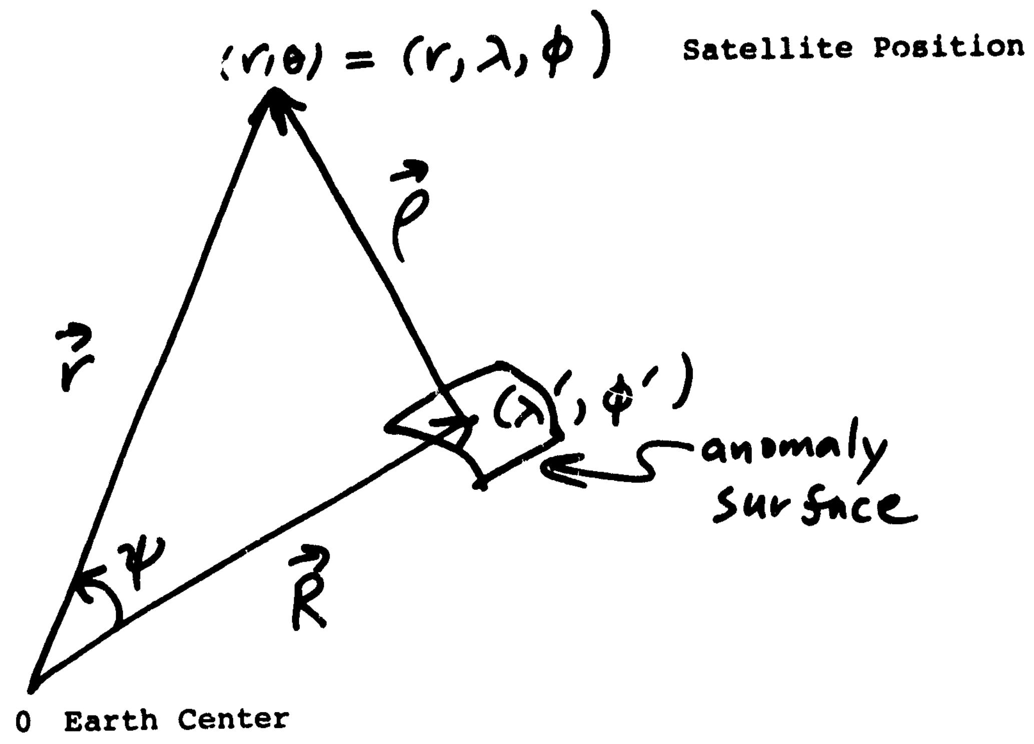

$$\rho = \sqrt{r^2+R^2-2rR\cos\psi}$$

Figure 14. Satellite and surface anomaly coordinates and position vector.

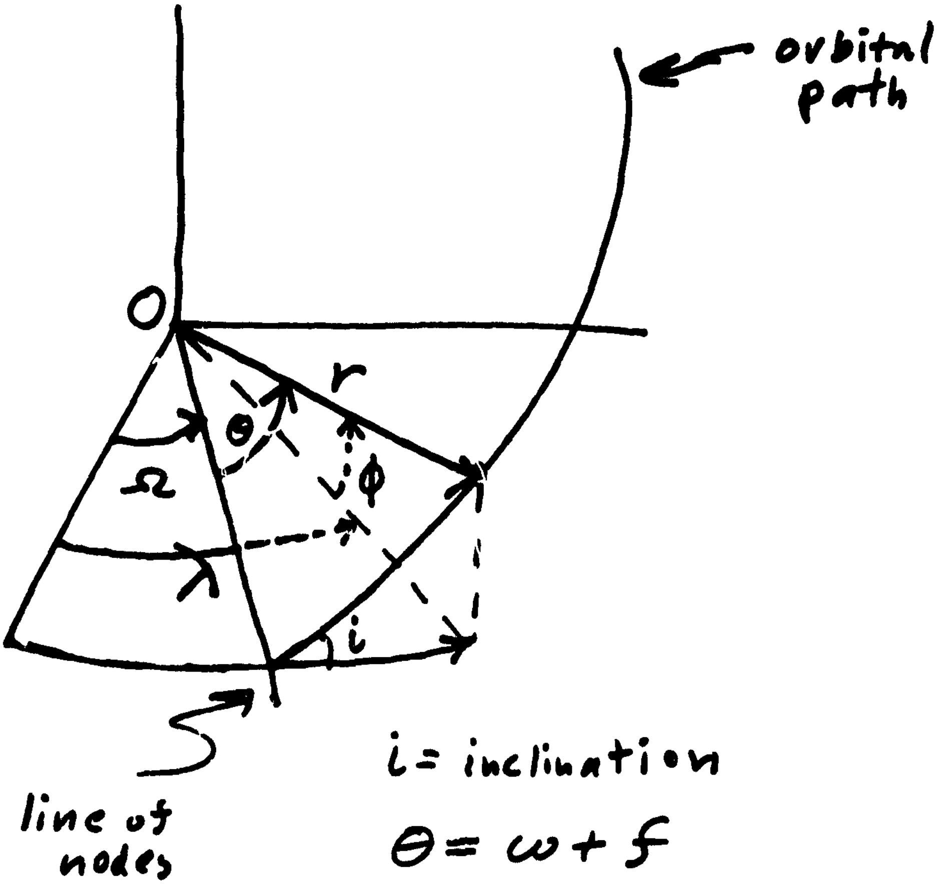

Figure 15. Satellite orbital elements.

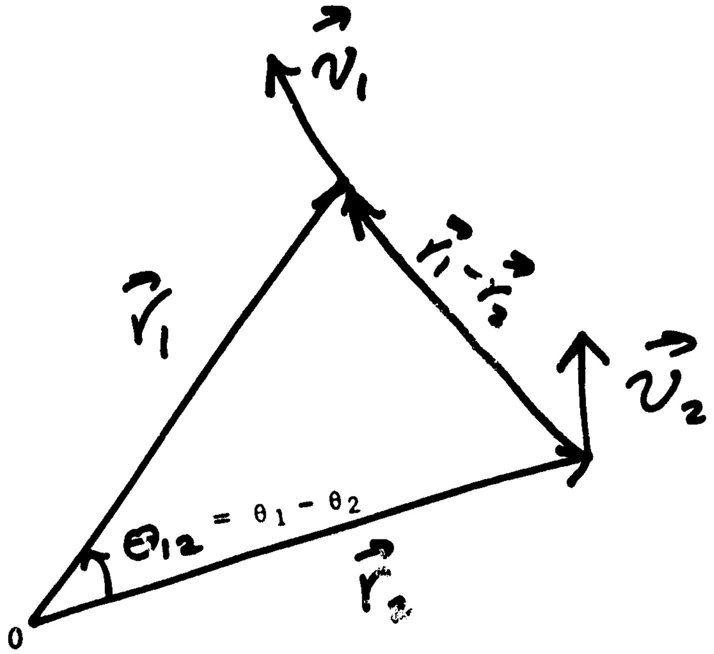

Figure 16. Satellites' coordinates and vectors.

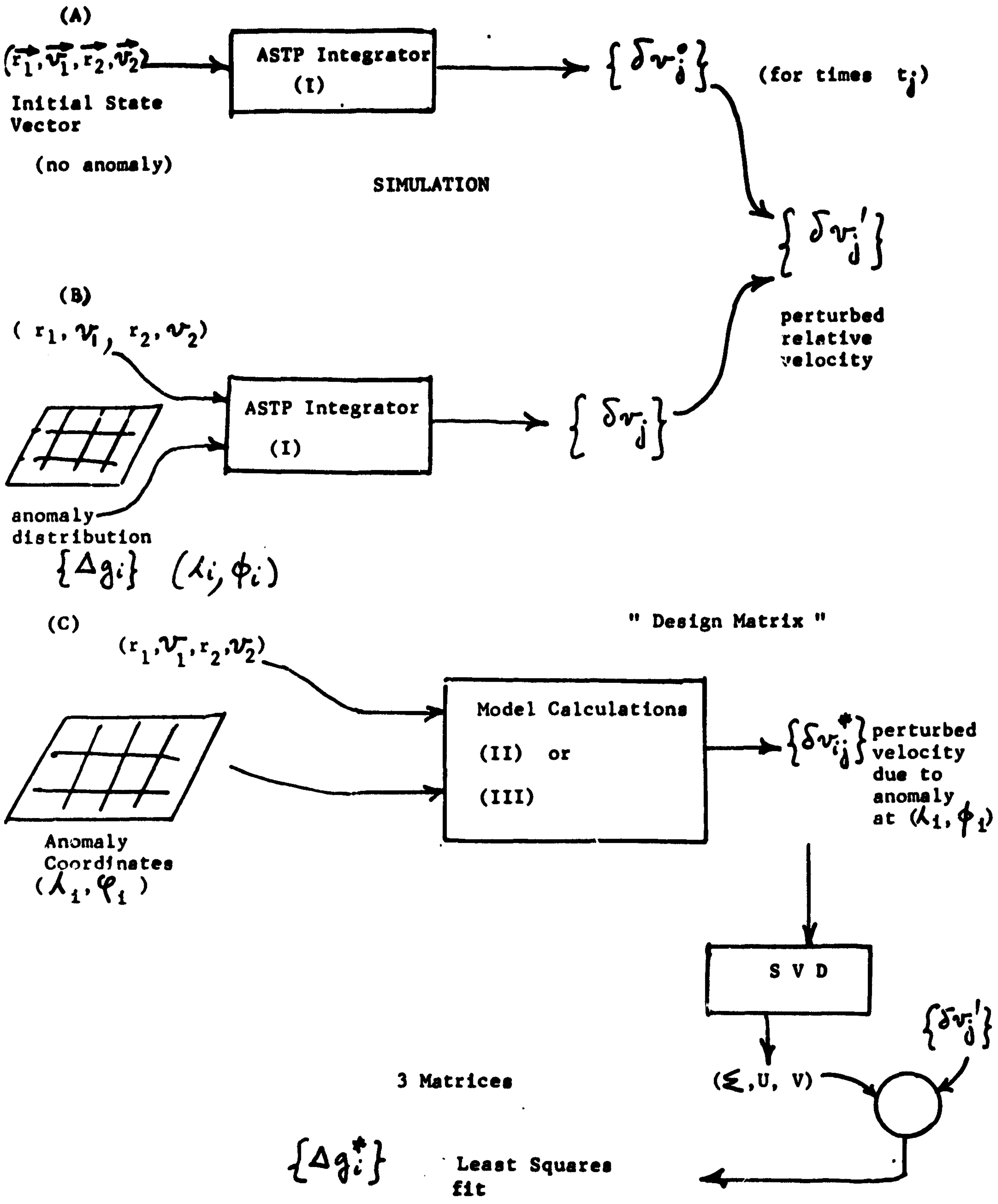

Figure 17. Schematic diagram of software system used to simulate data and to do least-squares fitting.

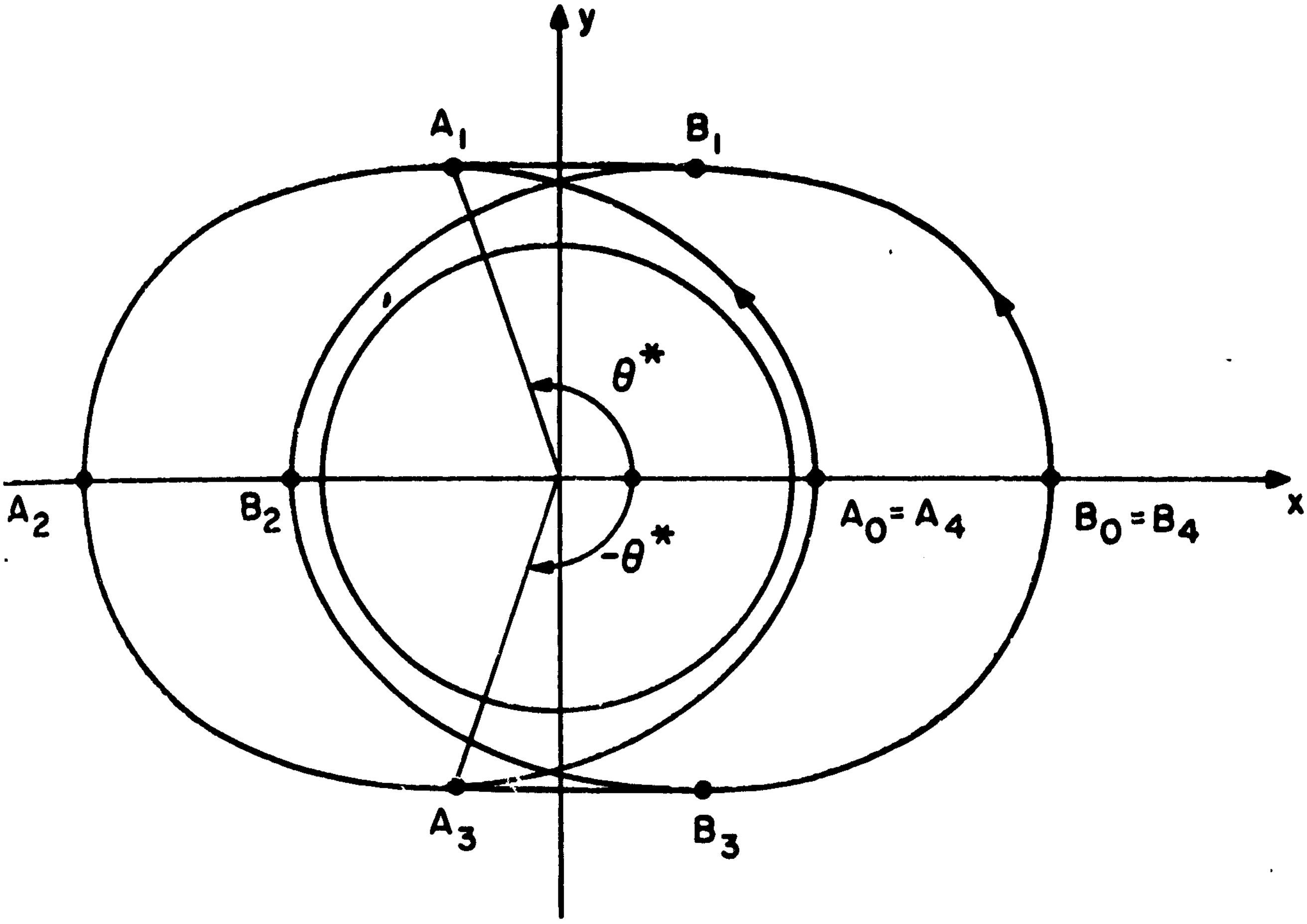

Figure 18. Geometrical configuration of the Colombo scheme.

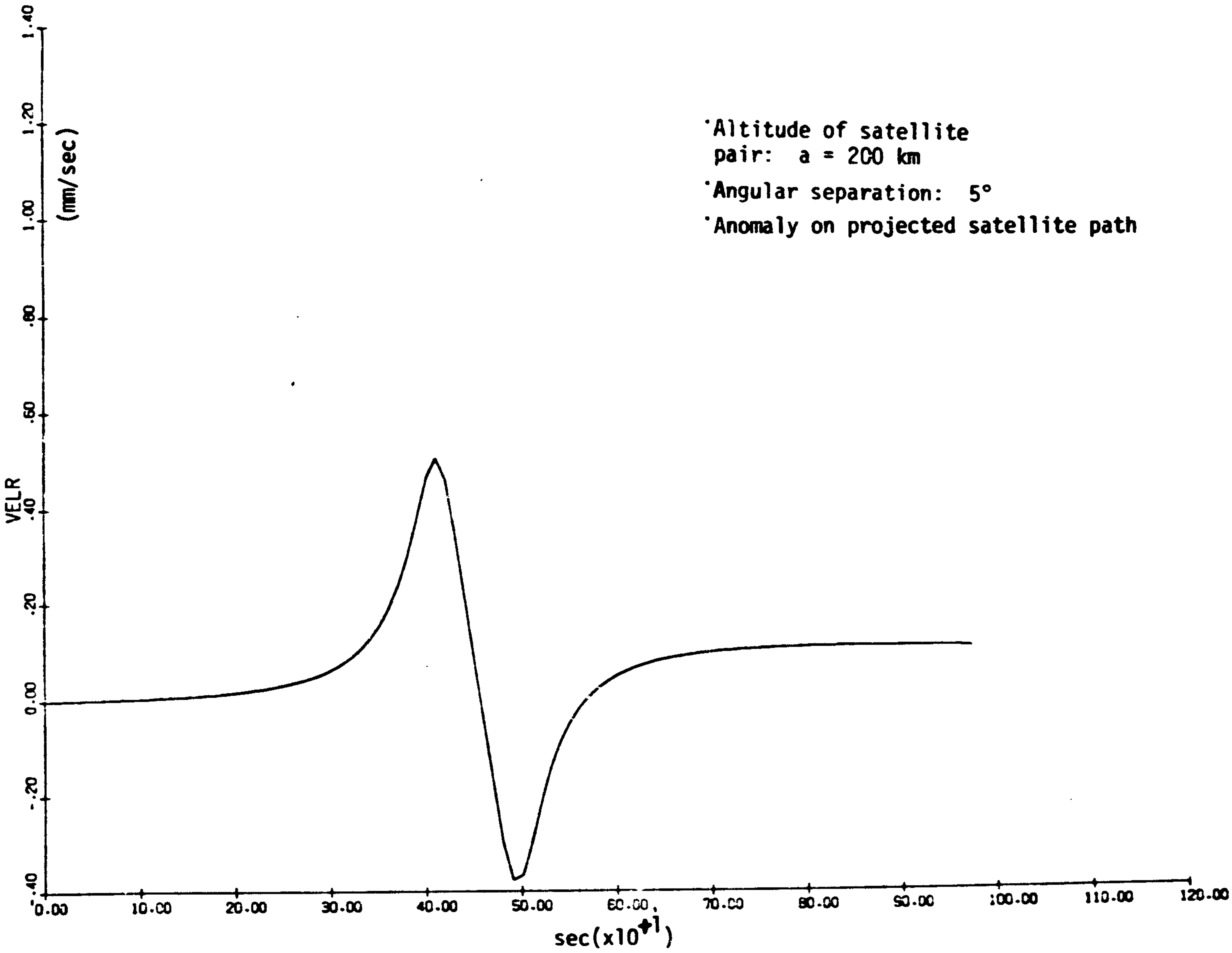

Figure 19(a). Perturbed relative velocity signature of a single, 1° x 1°, 20π mgal surface anomaly for standard low-low configuration.

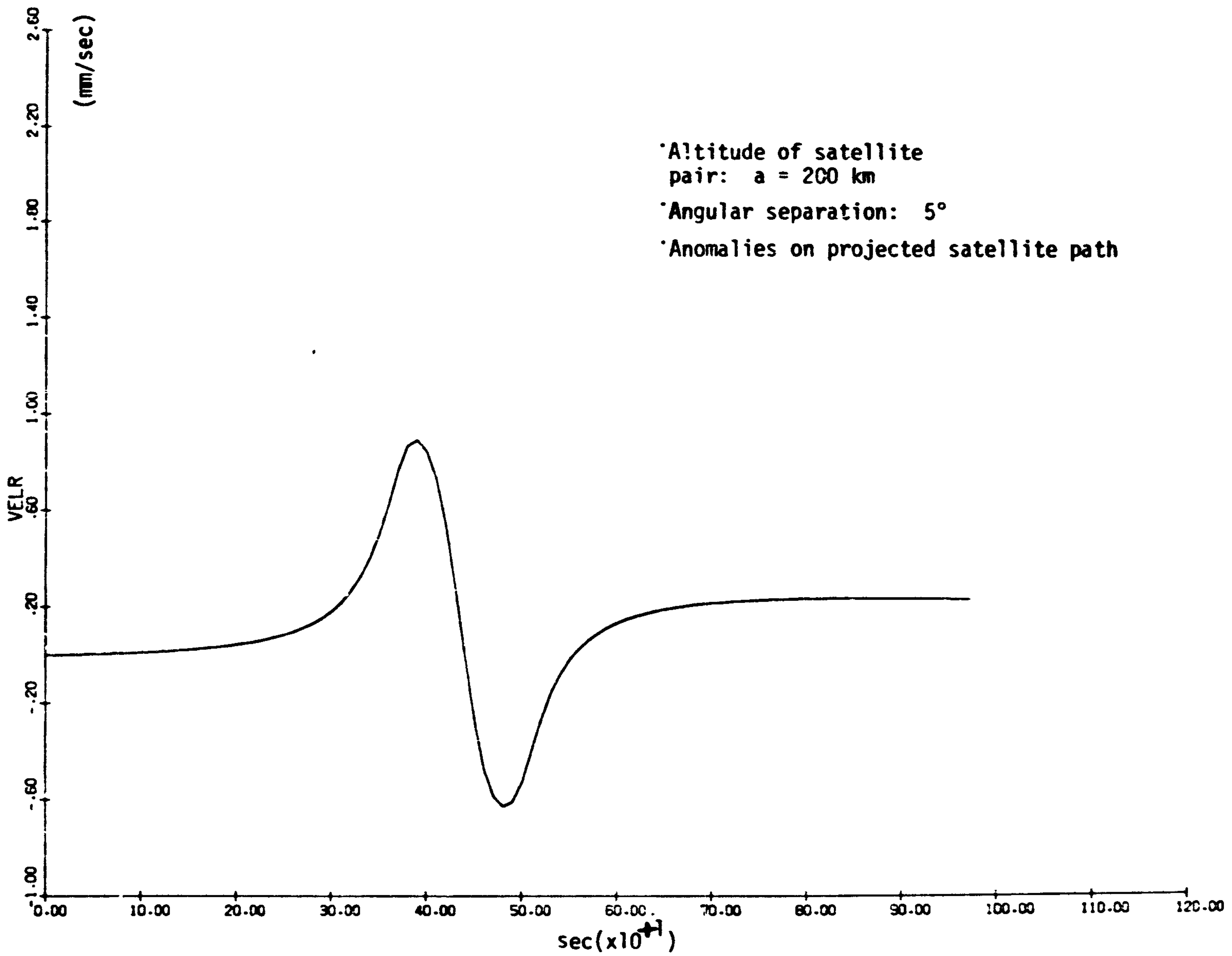

Figure 19(b). Perturbed relative velocity signature of two 20π mgal, 1° x 1°, surface anomalies (2° apart), for standard low-low configuration.

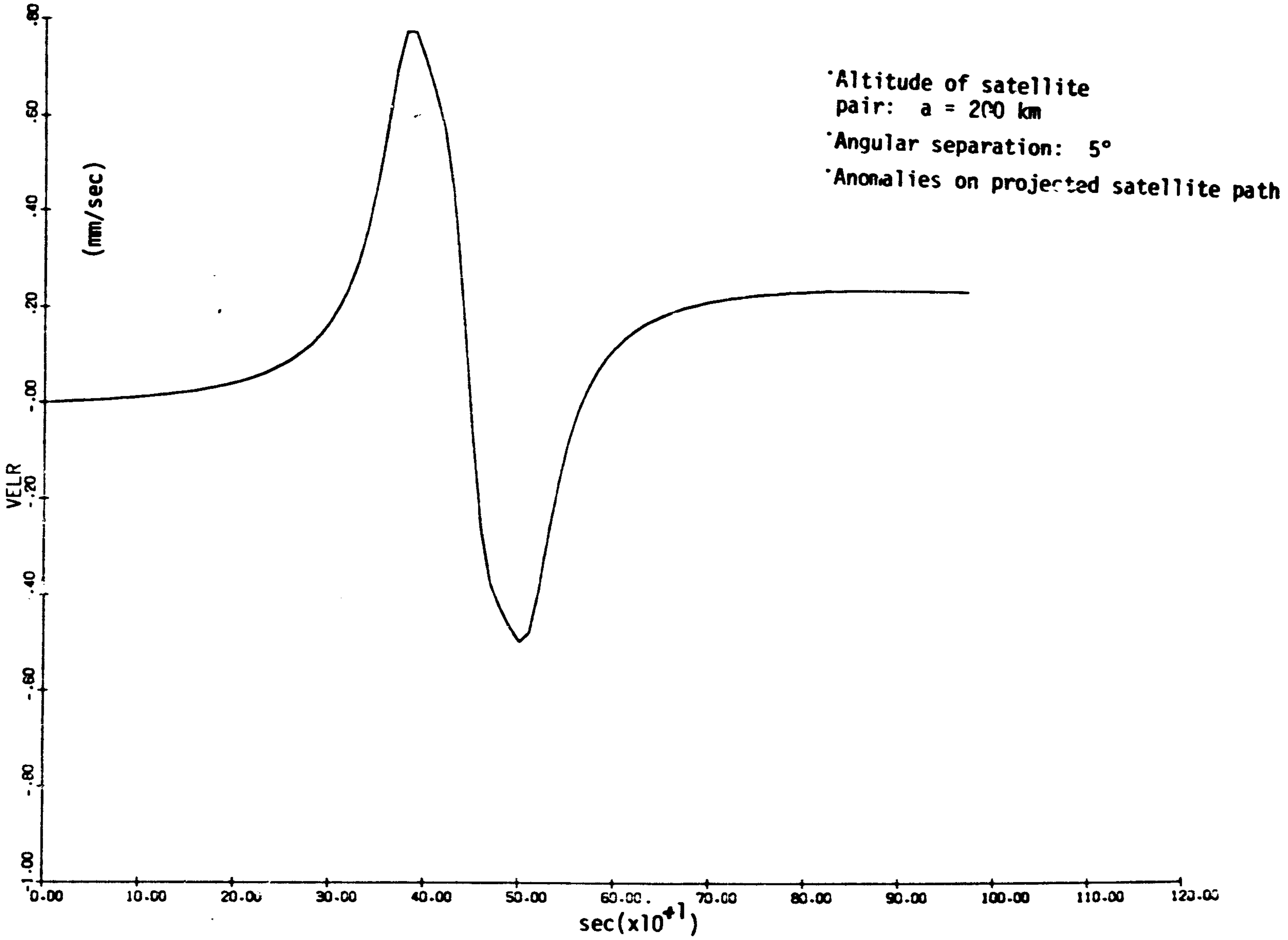

Figure 19(c). Perturbed relative velocity signature of two 20π mgal, 1° x 1°, surface anomalies (3° apart), for standard low-low configuration.

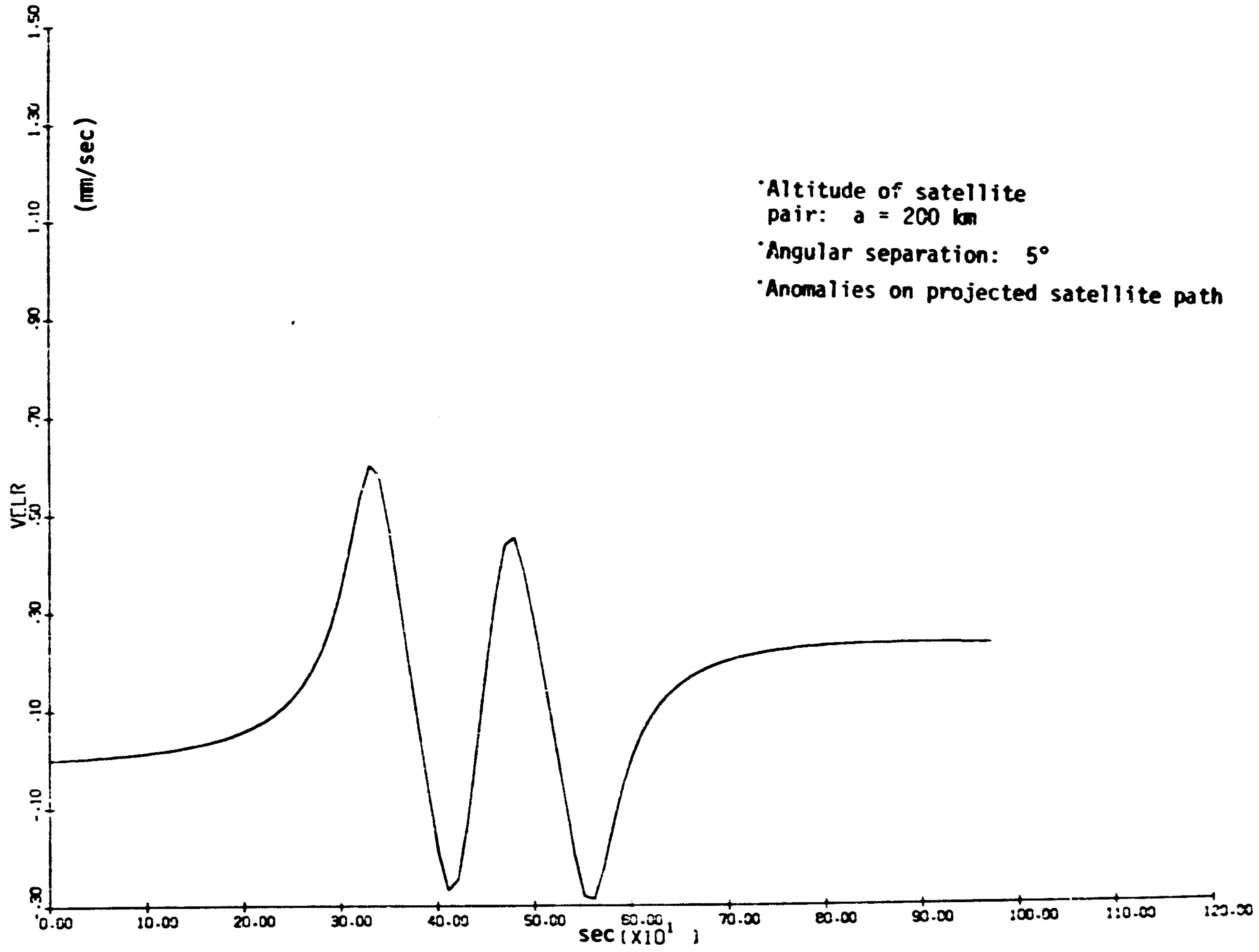

·Altitude of satellite
pair: a = 200 km

·Angular separation: 5°

·Anomalies on projected satellite path

Figure 19(d). Perturbed relative velocity signature of two 20 mgal, 1° x 1°, surface anomalies (10° apart), for standard low-low configuration.

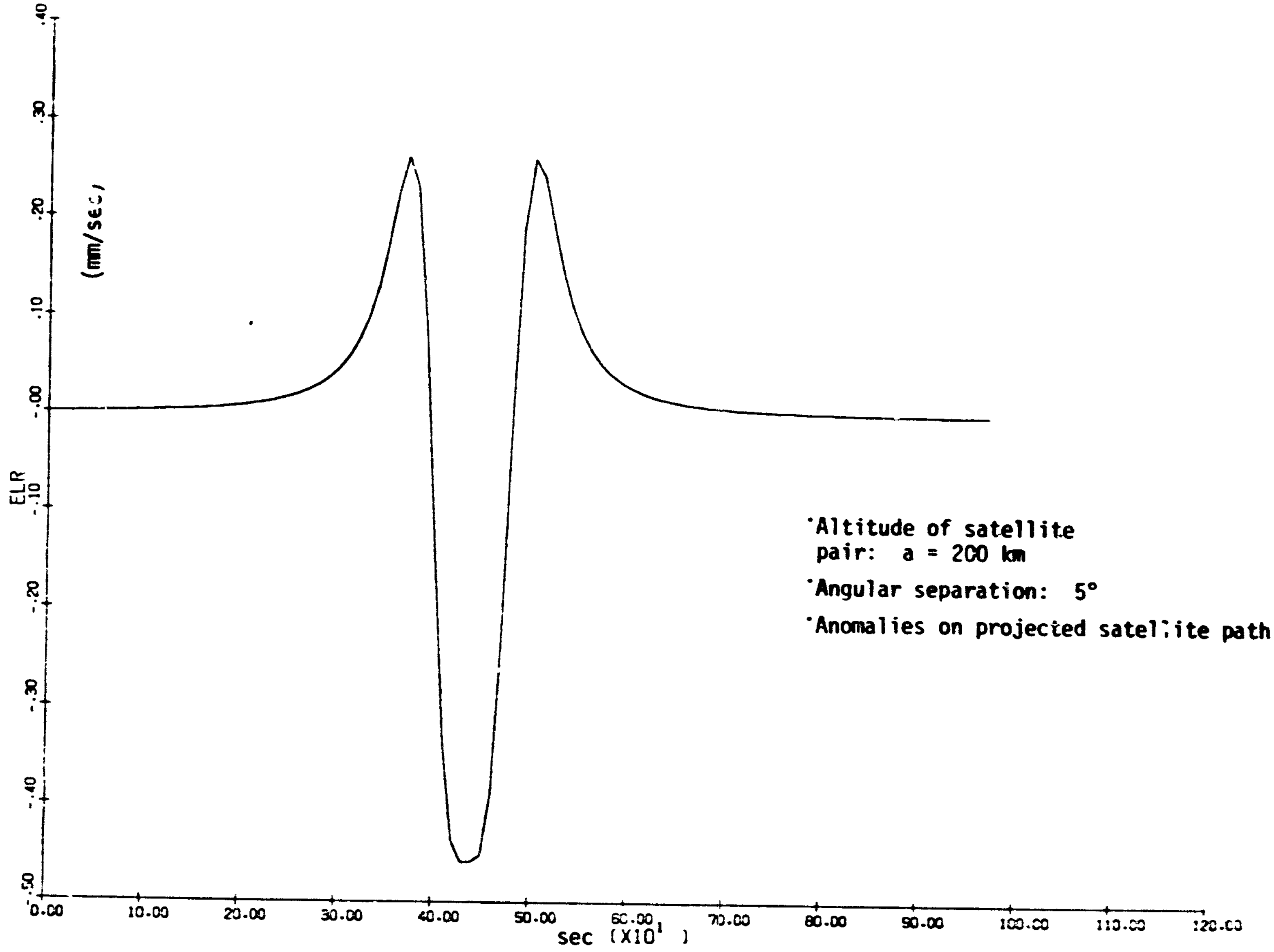

Figure 19(e). Perturbed relative velocity signature of two 20π mgal, 1° x 1°, surface anomalies, of opposite sign and 2° apart, for standard low-low configuration.

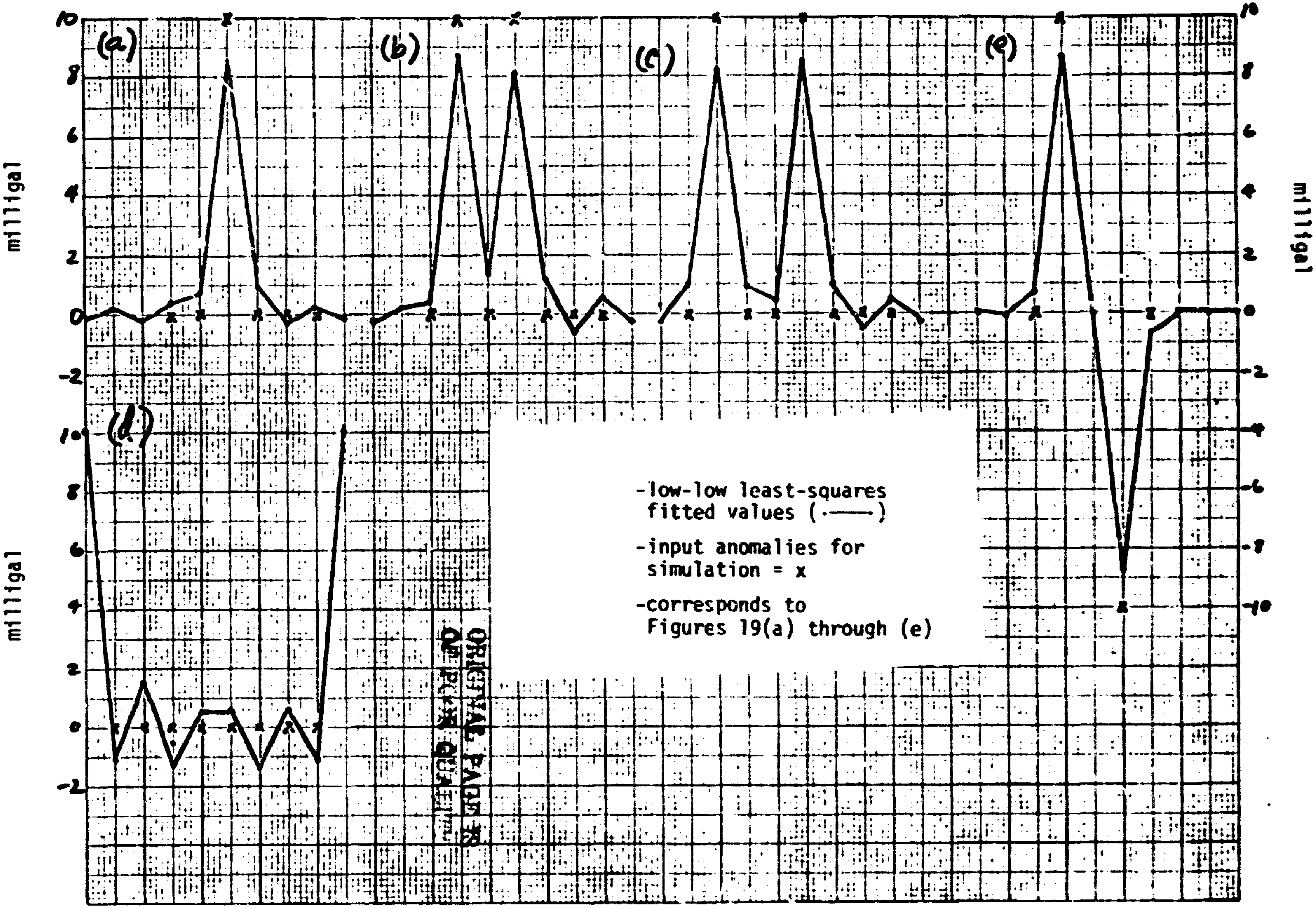

Figure 20(a through e). Least squares fitted anomalies obtained for simulated standard low-low configuration data.

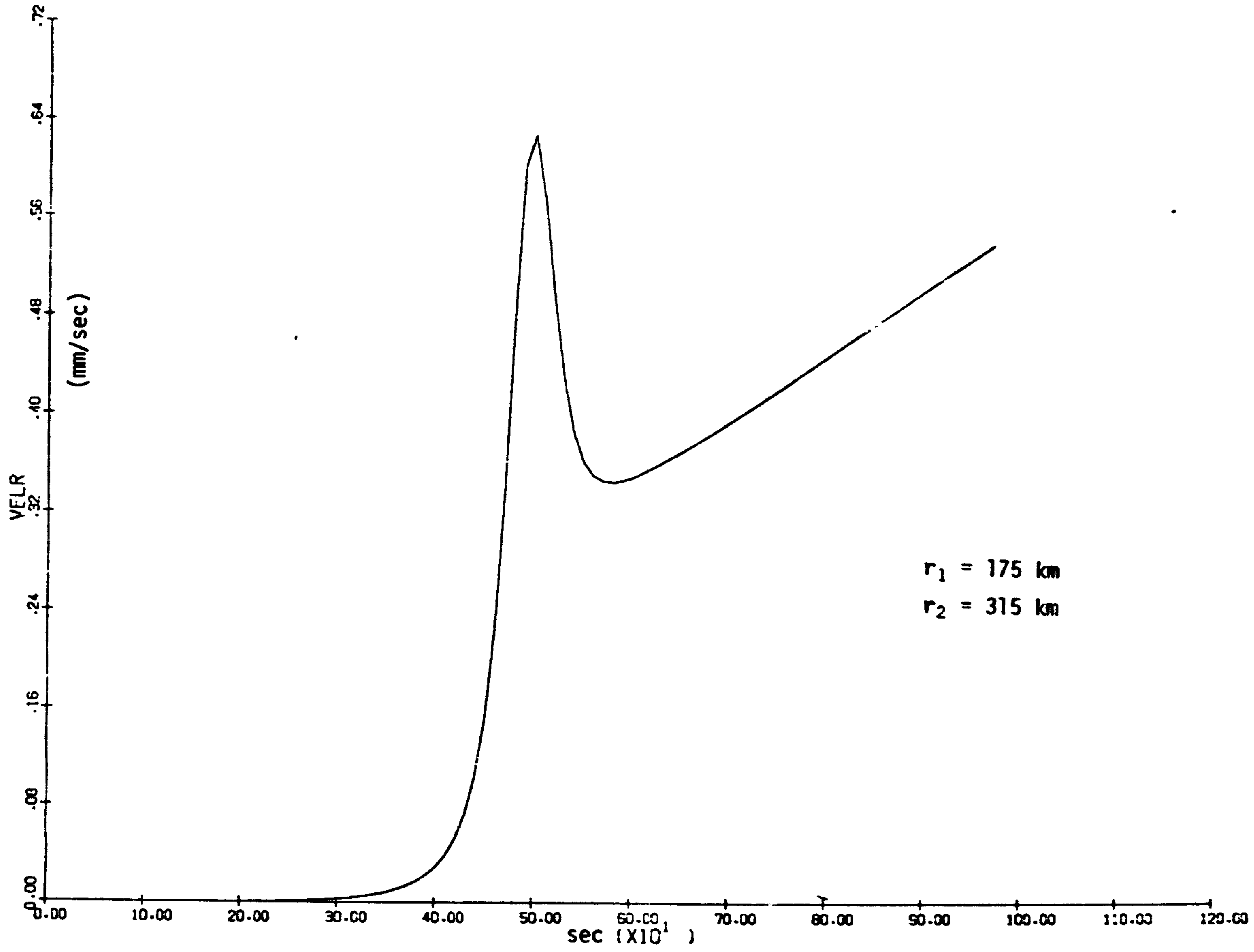

Figure 21(a). Perturbed relative velocity signature of a single, 1° x 1°, 20π mgal surface anomaly, for the Colombo configuration in "high-low" mode.

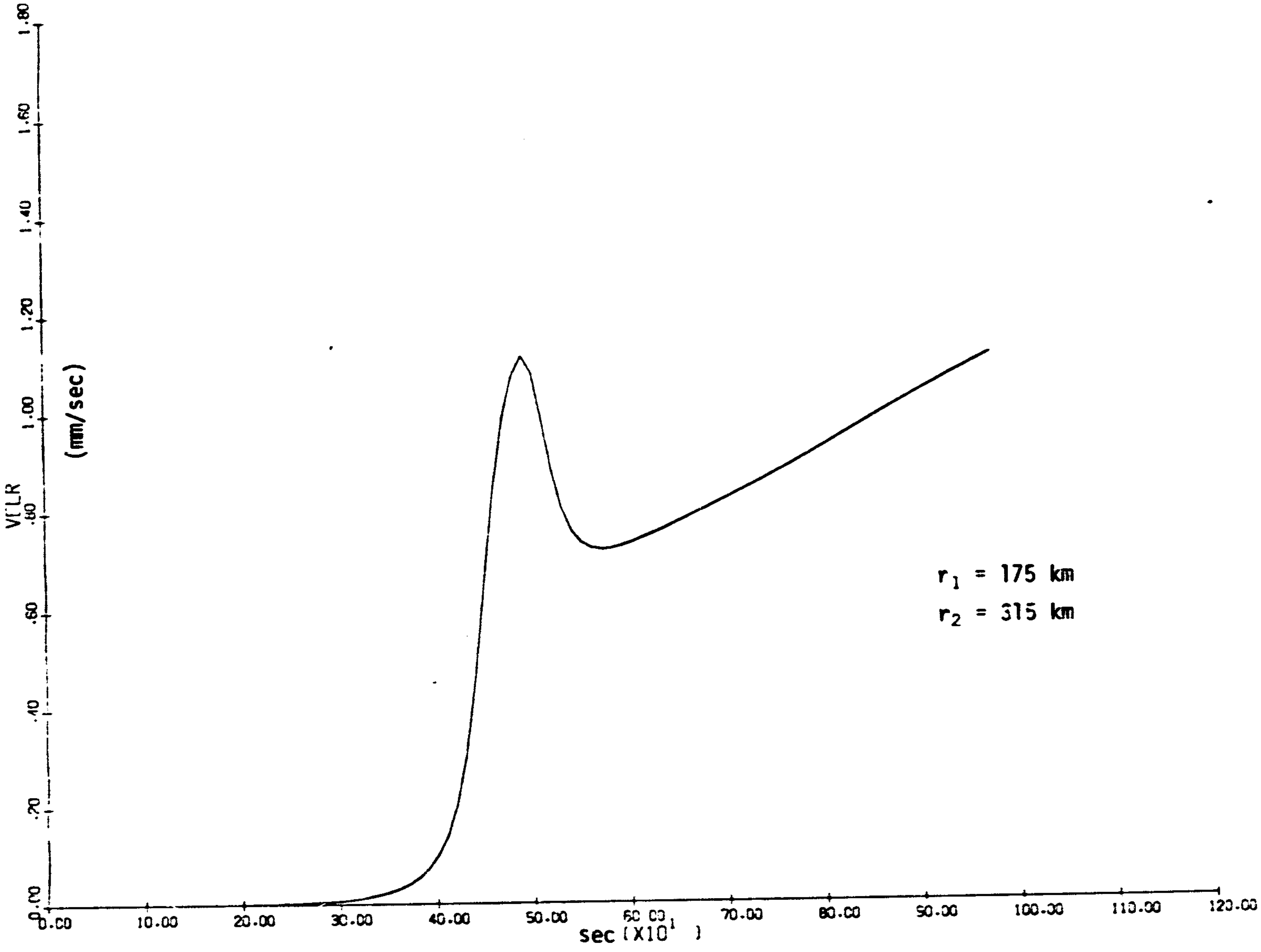

Figure 21(b). Perturbed relative velocity signature of two 20π mgal, 1° x 1° surface anomalies (2° apart), for the Colombo configuration in "high-low" mode.

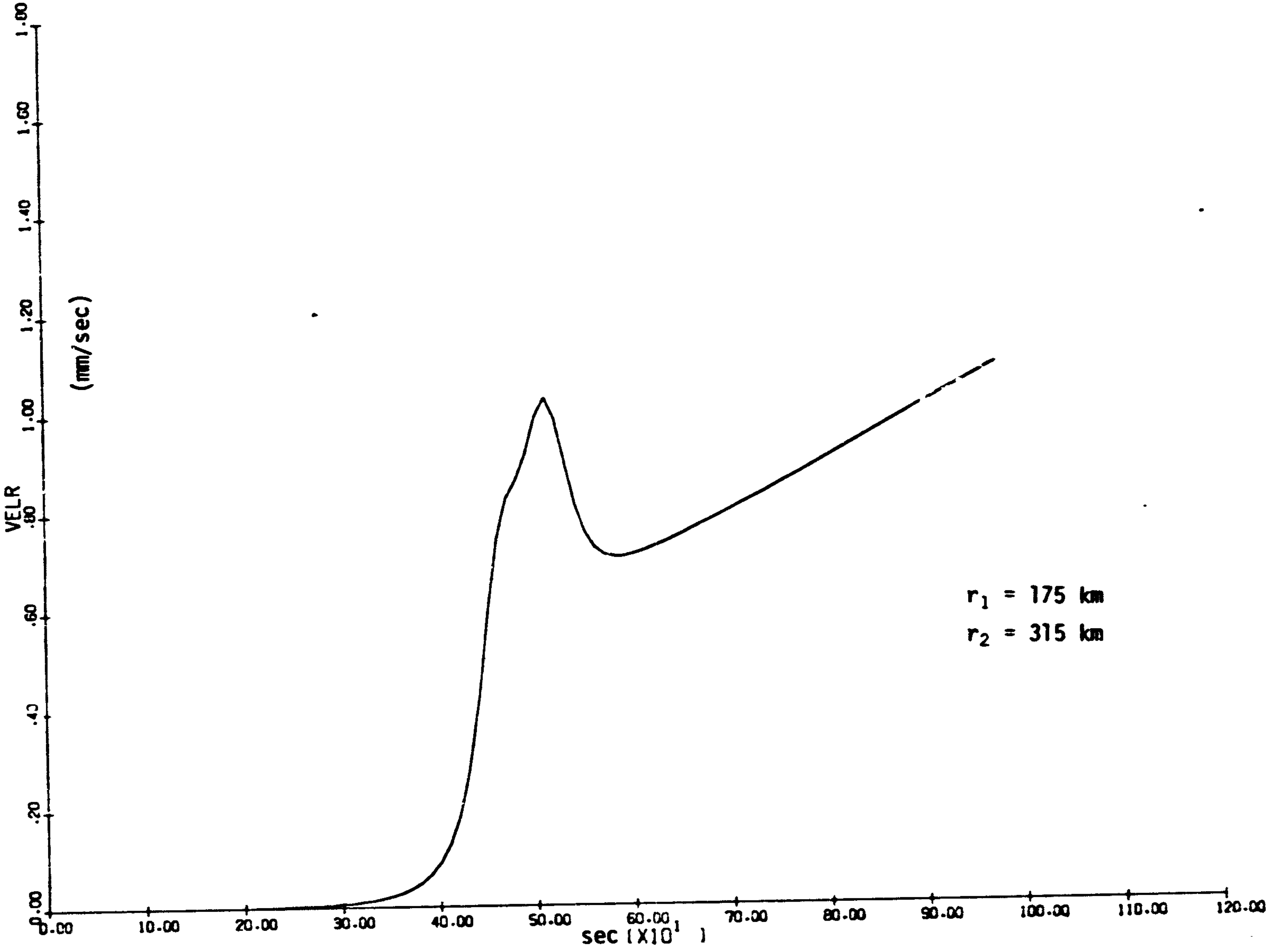

Figure 21(c). Perturbed relative velocity signature of two 20π mgal, 1° x 1°, surface anomalies (3° apart), for the Colombo configuration in "high-low" mode.

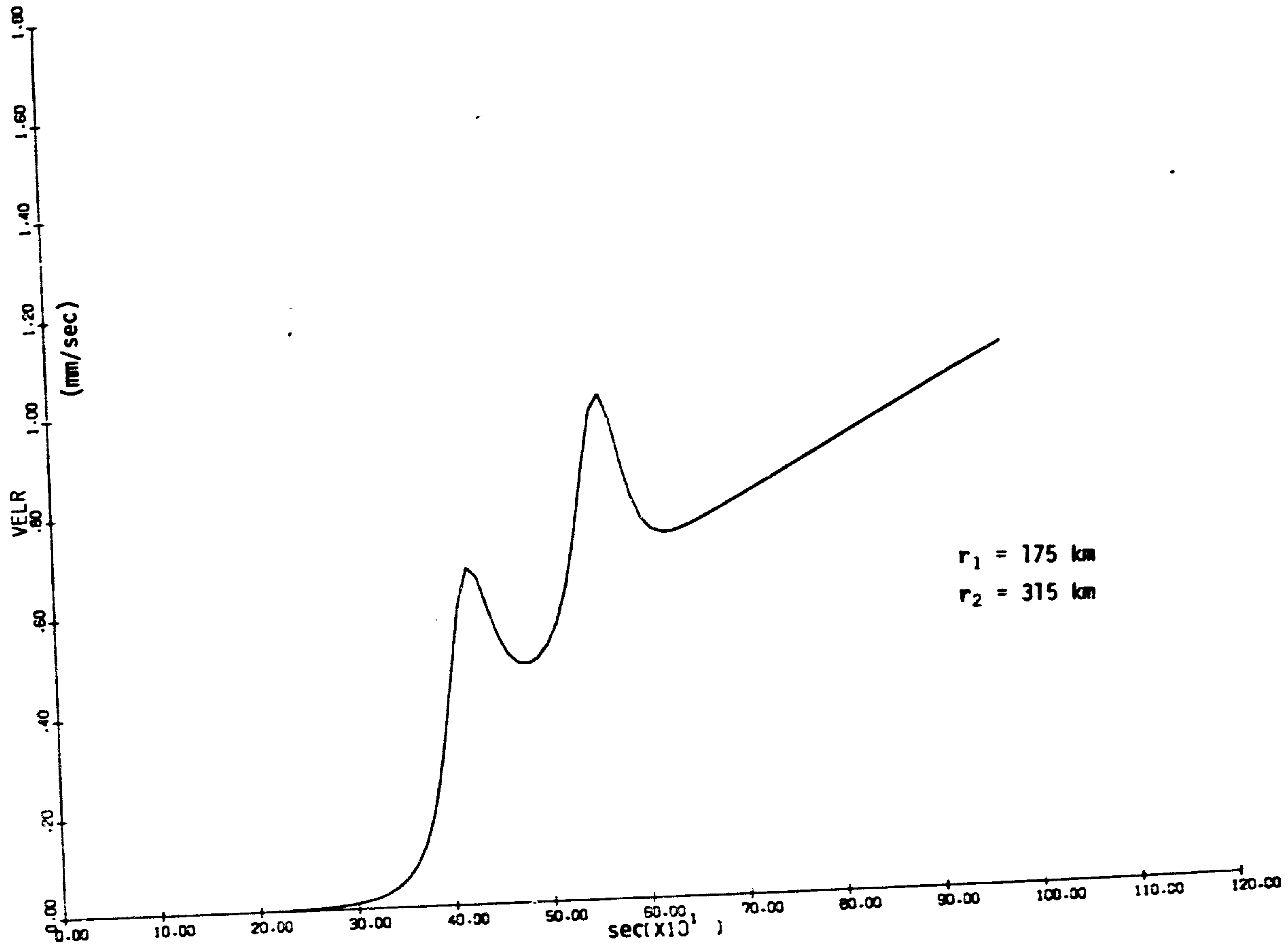

Figure 21(d). Perturbed relative velocity signature of two 20π mgal, 1° x 1°, surface anomalies (10° apart), for the Colombo configuration in "high-low" mode.

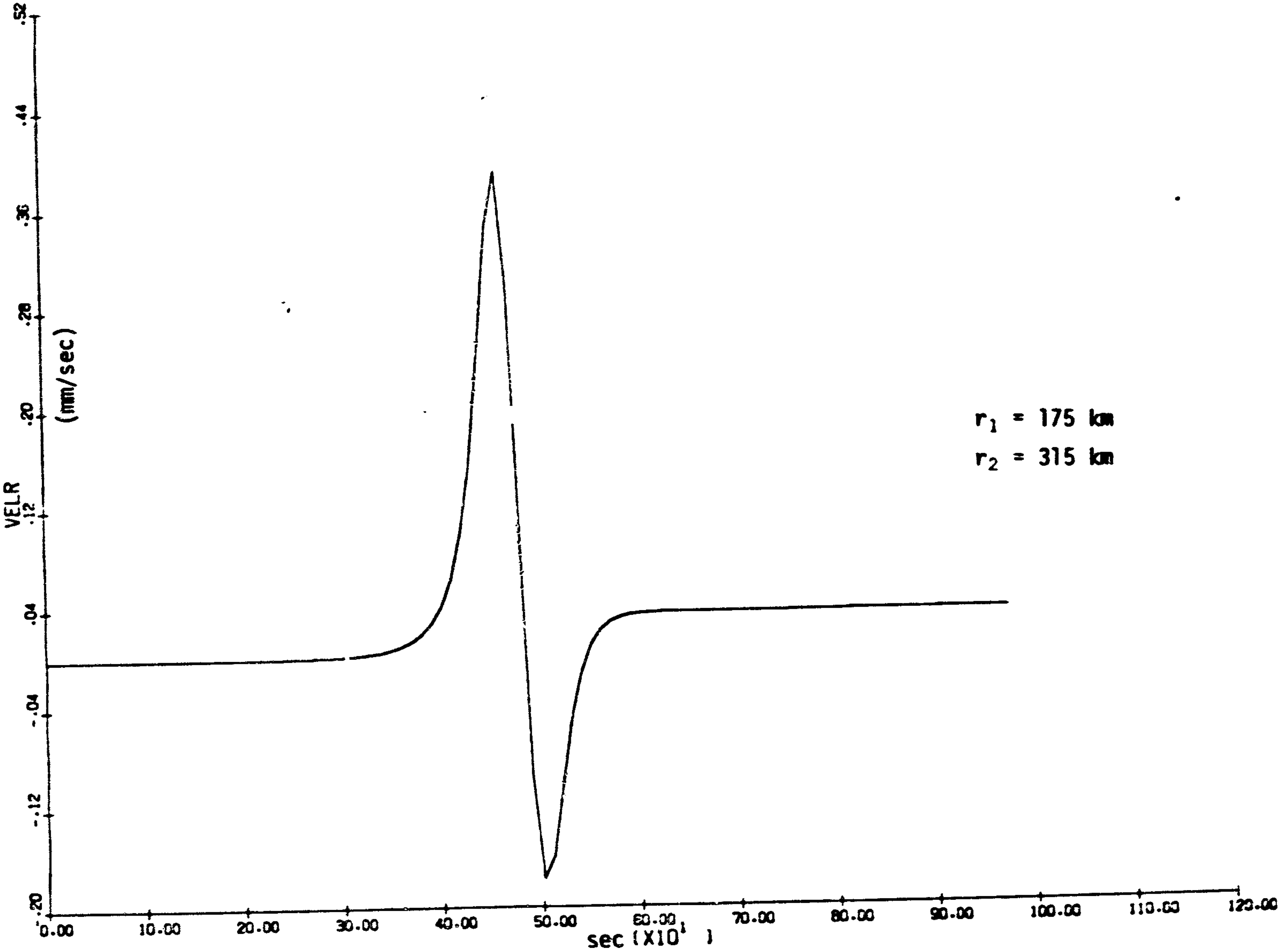

Figure 21(e). Perturbed relative velocity signature of two 20± mgal, 1° x 1°, surface anomalies of opposite sign and 2° apart, for the Colombo configuration in "high-low" mode.

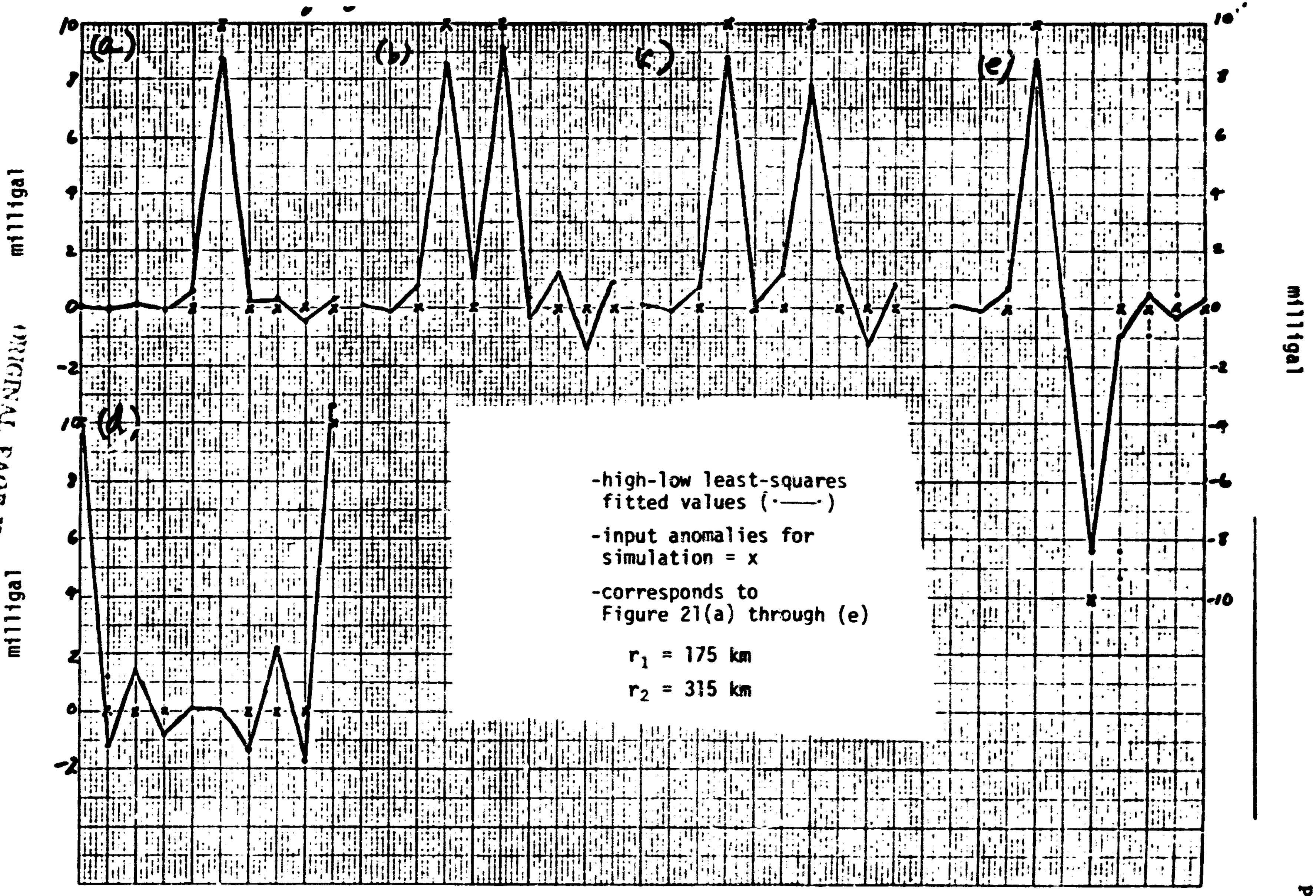

Figure 22(a through e). Least squares fitted anomalies obtained for simulated data pertaining the Colombc configuration in the "high-low" mode.

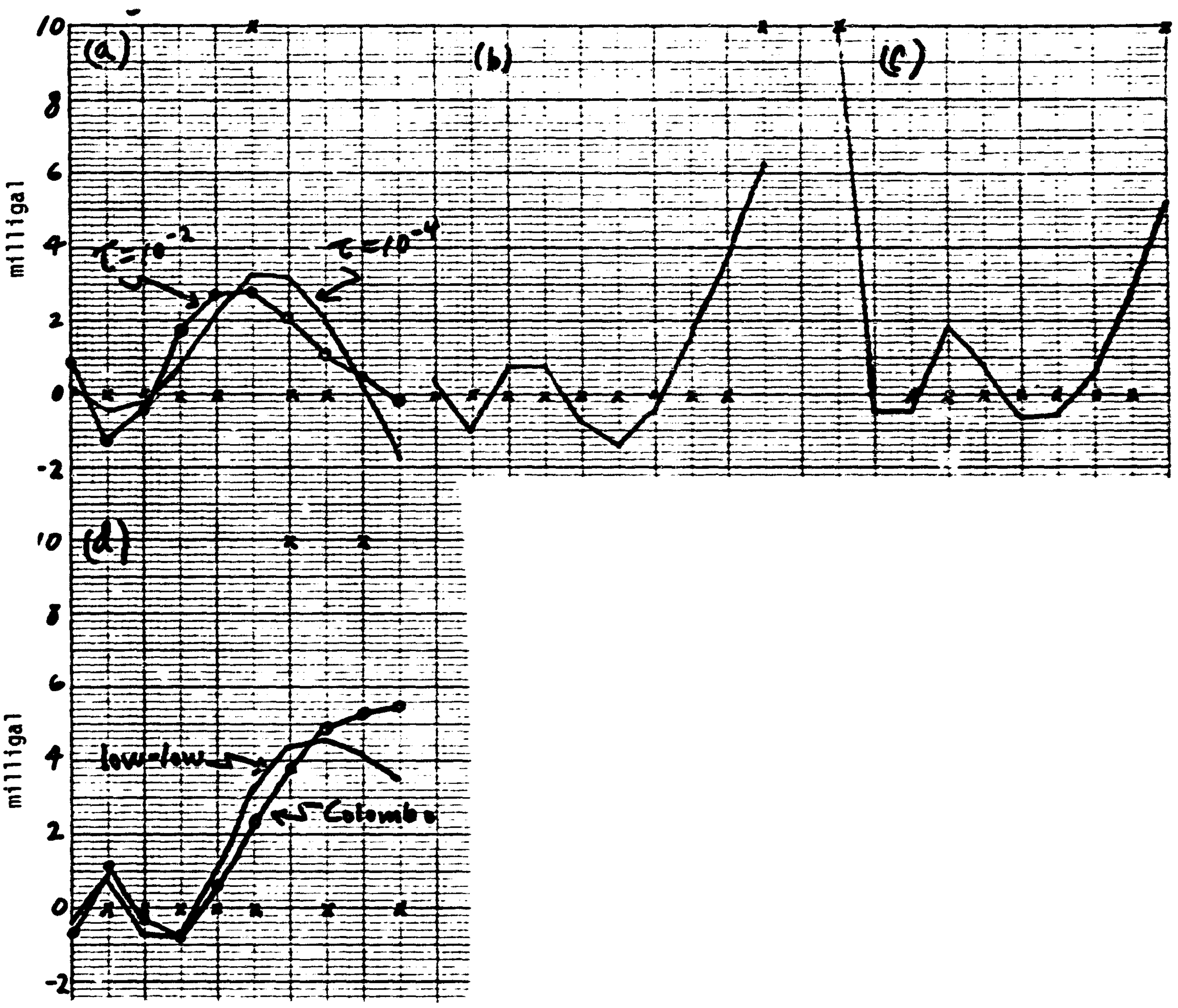

Figure 23. Recovery of anomaly elements aligned perpendicular to the satellite path.

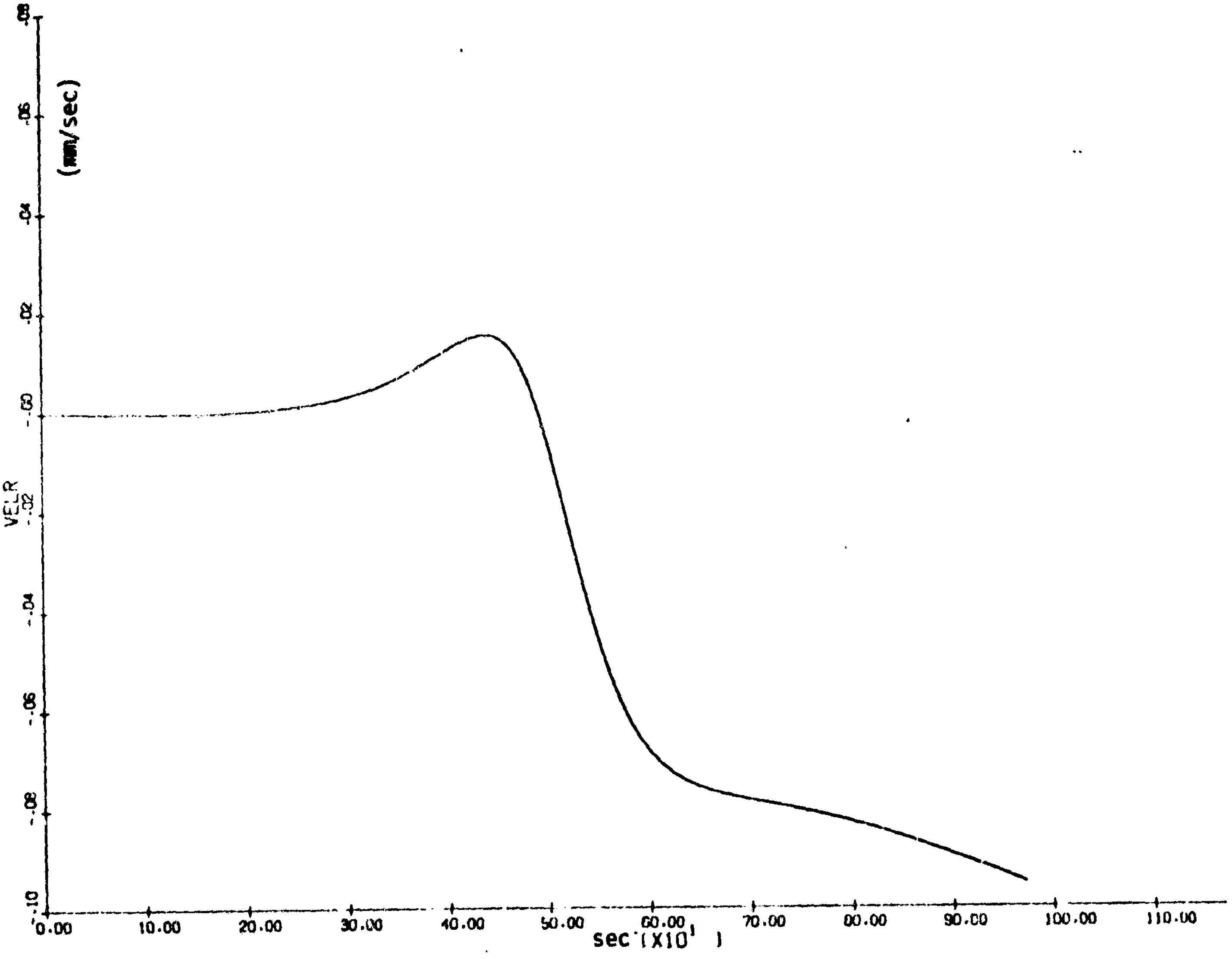

Figure 24. Perturbed relative velocity signature for the case in Figure 23(d) (Colombo configuration, "high-low" mode).

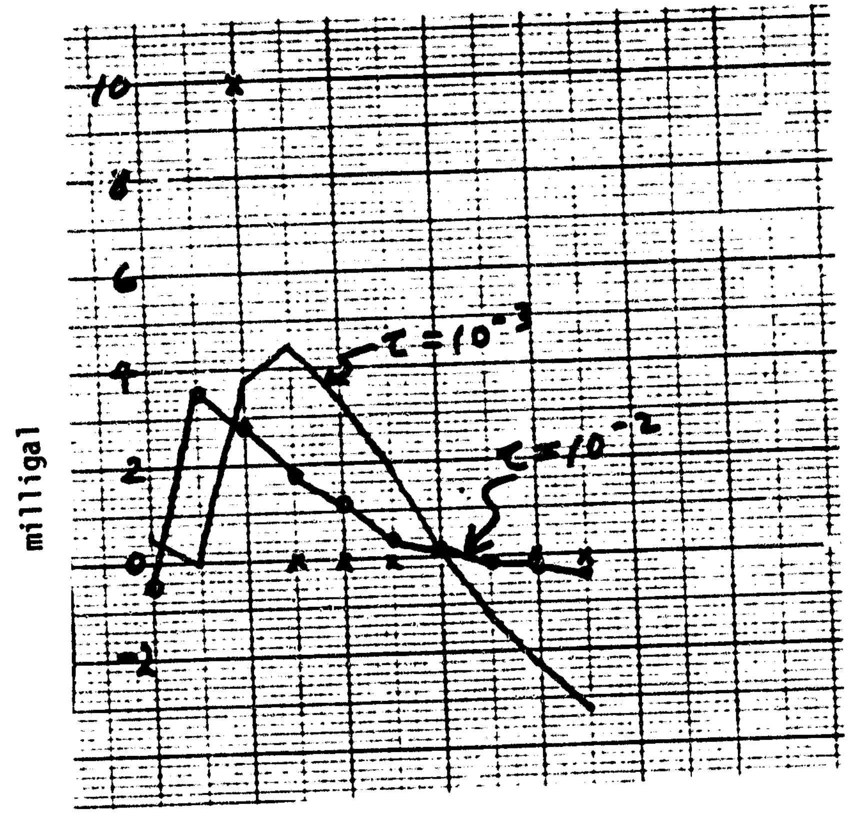

Figure 25. Recovery of a buried anomaly by the Colombo scheme in "high-low" mode.

11. References

(1) Rummel, R. (1975). Downward continuation of gravity information from satellite to satellite tracking or satellite gradiometry in local areas. Ohio State Univ., Dept. Geod. Sci. Rep. No. 221, 50 pp.

(2) Rummel, R., Reigber, C., and Ilk, K.H. (1978). The use of satellite-to-satellite tracking for gravity parameter recovery. In *Proceedings of the Space Oceanography Navigation and Geodynamics Workshop*, European Space Agency, ESA SP-137.

(3) Schwarz, C.R. (1970). Gravity field refinement by satellite-to-satellite doppler tracking. Ohio State Univ., Dept. Geod. Sci. Rep. No. 147, 141 pp.

(4) Wolf, M. (1969). Direct measurements of the earth's gravitational potential using a satellite pair. *Journ. Geophys. Res.*, vol. 74, pp. 5295-5300.

(5) Forsythe, G.E.. Malcomb, M.A., and Moler, C.B. (1977). *Computer Methods for Mathematical Computations*, Prentice-Hall.